Electrochemical Focal Hypoxia for Cell Models

Joseph Jo Yin Wong

Hughes Hall

Department of Chemical Engineering and Biotechnology

University of Cambridge

January 2021

This dissertation is submitted for the degree of Doctor of Philosophy.

This thesis is the result of my own work and includes nothing which is the outcome of work done in collaboration except as declared in the preface and specified in the text. It is not substantially the same as any work that has already been submitted before for any degree or other qualification except as declared in the preface and specified in the text. This dissertation does not exceed the prescribed word limit for the Engineering Degree Committee

For everyone I have met in my life

Electrochemical Focal Hypoxia for Cell Models

Joseph Jo Yin Wong

Abstract

For the last few decades, there has been increasing attention to hypoxia's (low oxygen) contribution to poor prognosis and ineffective treatments. Despite existing physiologically, hypoxia is a pathological accompaniment in a myriad of diseases, including tumour, stroke, dementia and cardiovascular diseases, that causes damage locally and to surrounding tissues. The inflicted damage is particularly significant in the brain which uses 20% of the body's total oxygen supply and has limited energy storage.

Currently common hypoxia models such as low oxygen incubators, hypoxia chambers and chemical hypoxia have two major flaws: no spatial control and long equilibration time. It is not possible to induce hypoxia focally such that these approaches have very limited translatability and resemblance to the physiology and pathophysiology of the local tissue. Thus, our ability to focus on the geography of events emerging from hypoxia has been limited.

This thesis addressed the spatiotemporal limitation of existing hypoxia models and investigated oxygen removal by electrochemical reduction in culture media. The platinum/graphite (Pt/C) electrode had a large surface area and showed promising catalytic properties for the oxygen reduction reaction in the culture media. The oxygen scavenging system effectively generated hypoxia at the base of the electrochemical cell in 7 minutes from normoxia, contrasting with hours needed by conventional methods. Its flexibility in reshaping and positioning were also beneficial to generating patterns of hypoxia gradient. Upon application to human cells, the electrochemical oxygen

scavenging system was proven to induce spatiotemporal response of HIF-1α transcription factor in neural progenitor cells. The system was also applied in a human cerebral microchannel model which was the first known *in vitro* model to demonstrate that 10-minute focal hypoxic stress on the axons caused the induction of apoptosis in human cortical neurons, observed in the distant cell bodies.

Acknowledgements

My PhD study in Cambridge has been extremely eventful and fruitful that it certainly is one of the highlights of my life. There are lots of people I would like to express my sincere gratitude towards.

First and foremost, I would like to express my deepest gratitude to my supervisor, Prof. Lisa Hall. She provided me a safe environment for learning and making mistakes whilst showing incredible amount of support and patience to nurture me. Her depth of knowledge and criticisms were constructive and insightful that inspires me to understand science and the world more profoundly. The skills and knowledge she taught me will certainly remain lifelong that I hope one day I can pass them to the generations to come. Her help and care were like no other that I cannot ask for a better supervisor and mentor for my PhD study.

Second, I would also like to extend my deepest gratitude to my advisor, Dr. Ragnhildur Thóra Káradóttir. She provided insightful knowledge in neuroscience that raised my interests and taught me to observe from an interdisciplinary angle. Our collaboration gave me many unique experiences that are desperate for. I am equally grateful for getting to know Dr. Balazs V Varga who is both my friend and mentor, showing determination at work but carefree at other occasions. Your guidance and patience gave me so much help in making progress. Dr. Deborah Kronenberg-Versteeg was also my friend and inspired me how to be good at science whilst taking good care of family.

Third, I would like to express my love to my family. My father, Mr. Eric Wei Chung Wong, my mother, Mrs. Tracy Yuet Wah Wong and my brother, Mr. Dominic Wai Yin Wong showed bottomless support to my studies and more so when I felt stressed. All of them are role models to my development that guided me through ups and downs. Most importantly, they have demonstrated that perseverance and sincerity are the core values of our family. I hope they will always forgive and tolerate my imperfections as a son or brother. Their love is certainly the greatest gift of my life that I can never ask for more.

Fourth mention has to go to my love, Dr. Shinnie Hei Ching Woo. She is an incredible person who helped me to find love, inspiration and motivation. Her love, patience and support gave me room to improve towards a better person. I hope that we will continue reminding and learning from each other, leading to a fabulous life together.

Fifth mention is dedicated to my closest friends Dr. Andrin Flütsch, Mr. Daniel Wales, Mr. Dushanth Seevaratnam (flat mate as well) and Dr. Walter Kähm. You are all crucial to my life in Cambridge and gave me joy whenever you are around. The activities we participated, places we have been and knowledge we exchanged are all so memorable and inspiring. I would like to thank few other good friends, Dr. Luca Villa, Miss Manja Neumann, Dr. Ziyan Zhao and my flat mates, Mr. Apoorv Jain and Dr. Fernando León-Cazares for being good and supportive companions.

I would also like to thank the Croucher Foundation and the Cambridge Trust for awarding me the Croucher Cambridge International Scholarship in support of my PhD study in Cambridge. This section of my life would not be possible if it were not supported.

Finally, I must thank every person I have met in my life that I might not have the opportunity to mention here. Our encounters, both positive and negative, shaped me into the person I am today. Conversations we held and activities we participated may not be recalled in detail but certainly left their marks in my personality and development.

“Do not pray for an easy life, pray for the strength to endure a difficult one “

- *Bruce Lee*

Table of contents

Abbreviations

CA	Chronoamperometry
CV	Cyclic voltammetry
HIF-1α	Hypoxia inducible factor 1α
NPC	Neural progenitor cells
ODD	Oxygen reduction reaction
Pt/C	Platinum / Graphite
NMCM	Neural progenitor maintenance culture medium
NDCM	Neuron differentiation culture medium
FGF	Fibroblast growth factor
SCM	Scavenging Culture Medium
SRP	Staurosporine
PDMS	Polydimethylsiloxane
PGMEA	Propylene glycol methyl ether acetate
PBS	Phosphate Buffer Saline
BSA	Bovine Serum Albumin
HRP	Horseradish Peroxidase

Chapter 1: Introduction

I. General introduction

Oxygen homeostasis is extremely important for maintaining cell and tissue functionalities in complex organisms. In the human body, ambient oxygen diffuses through the alveoli walls and is taken up by the haemoglobin in the capillaries. An oxygen gradient is developed to distribute oxygen to the entire body for maintaining cellular functions. From the atmospheric oxygen concentration 21% (159mmHg), oxygen concentration at the alveoli is circa 14% (106mmHg) and reduces to 12% (90mmHg) in the arterial blood and 5% (38mmHg) in the venous blood.[1] Mitochondria utilize about 0.3% – 0.7% (2.7 – 5.9 mmHg) oxygen for aerobic metabolism and produce adenosine triphosphate (ATP) to support life.[2] While oxygen takes the important role in energy production, tight regulation of oxygen supply is paramount to protect cells from over-exposure to oxygen. Homeostasis limits the generation of reactive oxidative species, by-products of the electron transport chain, that can cause cell damages and senescence.[3] As a result, some cells require and adapt, to rely on anaerobic metabolism due to the temporal or permanent oxygen deficiency at the local tissue, broadly identified as hypoxia.[4,5]

II. Hypoxia

Hypoxia is defined as the sub-physiological oxygen concentration in the local tissue. Physiological oxygen concentration, normoxia is generally defined as 20mmHg to 53mmHg (3-7%) O_2 in the cellular level in which the demand of oxygen in the mitochondria are met. Hypoxia is defined as oxygen concentration below normoxia but without reaching the absence of oxygen, anoxia. Interestingly, hypoxia can arise physiologically or pathologically. Physiological hypoxia is naturally occurring and is evident in the many tissues, such as embryos during the developmental stage,[6] osteogenesis,[7] renal medulla for sodium reabsorption,[8] stem cell niches [9–11] and skeletal muscle during development.[12] Pathological hypoxia was reported in a wide range of diseases, including stroke,[13] cardiovascular diseases,[14] tumours,[15] Alzheimer’s disease,[16–18] alcoholic liver disease,[19] acute renal injury,[8] and inflammatory bowel disease,[20] commonly caused by hypoxemia (reduced partial pressure of oxygen in blood), ischemia (restriction in blood supply), anaemia (decreased amount of red blood cells or decreased haemoglobin concentration) and increased oxygen demand under fixed oxygen supply. It is important to note that hypoxia plays different roles in the diseases. Hypoxia is central to some diseases like stroke, small vessel disease and traumatic brain injury whereas in alcoholic liver disease, acute renal injury and inflammatory bowel disease, the physiologically existing hypoxia leads to poorer prognosis. Despite being reported, the relationship between Alzheimer’s disease and hypoxia has not yet clearly established. Central to the oxygen sensing mechanism is the transcription factor: hypoxia inducible factor (HIF) that exists in all nucleated cells.

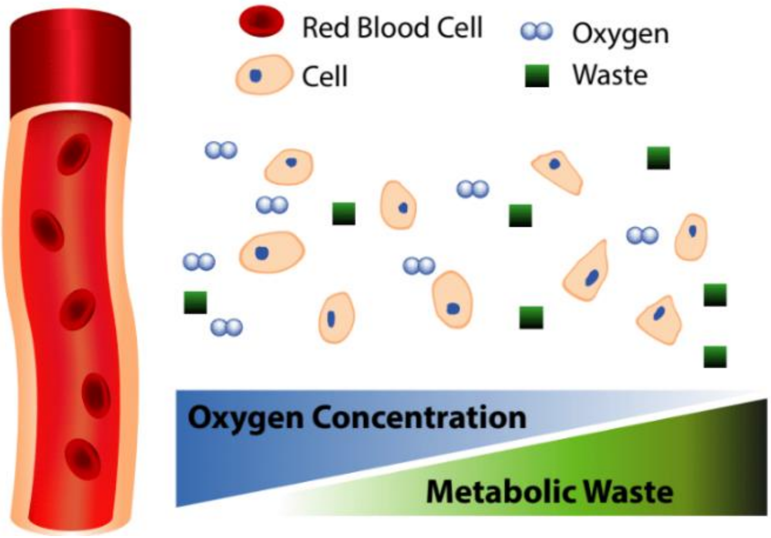

Figure 1.1 Schematic diagram of gradient establishment in proximity to the blood vessels.

II. I. Hypoxia inducible factor 1

HIF is a group of proteins existing as the master regulator of oxygen sensing in human cells, discovered in 1995 by Gregg L. Semenza and Guang Wang. HIF-1 exists as a heterodimer of hypoxia inducible factor-1α (HIF-1α) and hypoxia inducible factor-1β (HIF-1β), also known as aryl hydrocarbon receptor nuclear translocator (ARNT). The importance of this oxygen sensing mechanism can be explained by its regulation of a wide range of cellular mechanisms, including development, physiology, and pathophysiology. HIF is a molecular marker of hypoxia and is an excellent readout of the extent and intensity of tissue hypoxia. It is thus selected as the primary investigated marker in this thesis.

II. I. I. Oxygen sensing mechanism

Figure 1.2 Schematics of the structure of hypoxia inducible factor-1α (HIF-1α). bHLH: Base-helix loop helix; PAS: Per-Arnt-Sim domain; ODD: Oxygen degradation domain; Pro: Proline residue; TAD: Transaction domain.[21,22]

Hypoxia inducible factor-1α (HIF-1α) exists as the key transcription factor in sensing oxygen. It is associated with the feedback system to the cells and is arguably the most important protein in the group of HIFs. HIF-1α contains a basic helix loop helix (bHLH) – Per-Arnt-Sim (PAS) domain at the N-terminal. The HLH and PAS domain are responsible for dimerization whereas the basic domain, in combination with the C-terminal transactivation domain, mediates DNA binding.[23] After the PAS domain, the oxygen degradation domain contain two proline residues (proline 564 and proline 402). Under normoxia, these two prolines are hydroxylated by the family of 4-prolyl hydroxylase (PHD1, PHD2 and PHD3) with oxygen and 2-oxoglutarate as substrates and iron and ascorbate as co-factors.[24] The von Hippel-Lindau (VHL) tumour suppressor protein thus recognizes the hydroxylated HIF-1α and, along with elongins B and C,[25] ubiquitinates the protein for proteasomal degradation. As a result, HIF-1α is under constant turnover in normoxia and are usually degraded before dimerizing with HIF-1β. In hypoxia, PHD has reduced hydroxylation activity due to the diminished availability of oxygen as the co-substrate. VHL thus fails to recognize HIF-1α for ubiquitination and degradation. HIF-1α then dimerizes with HIF-1β to translocate to the cell nucleus as a transcription factor. HIF-1 binds to hypoxia recognition elements (HREs) of the target genes to induce gene transcription and downstream responses. Interestingly, the stabilization of proline 402 occurs at circa 15mmHg (2%) O_2 while that of proline 564 is at circa 4mmHg (0.5%) O_2.[24] This contributes to the HIF-1α level at half-maximum in circa 11mmHg (1.5%) O_2 and at maximum value in 4mmHg (0.5%) O_2, affecting HIF-1 DNA binding activity.[23]

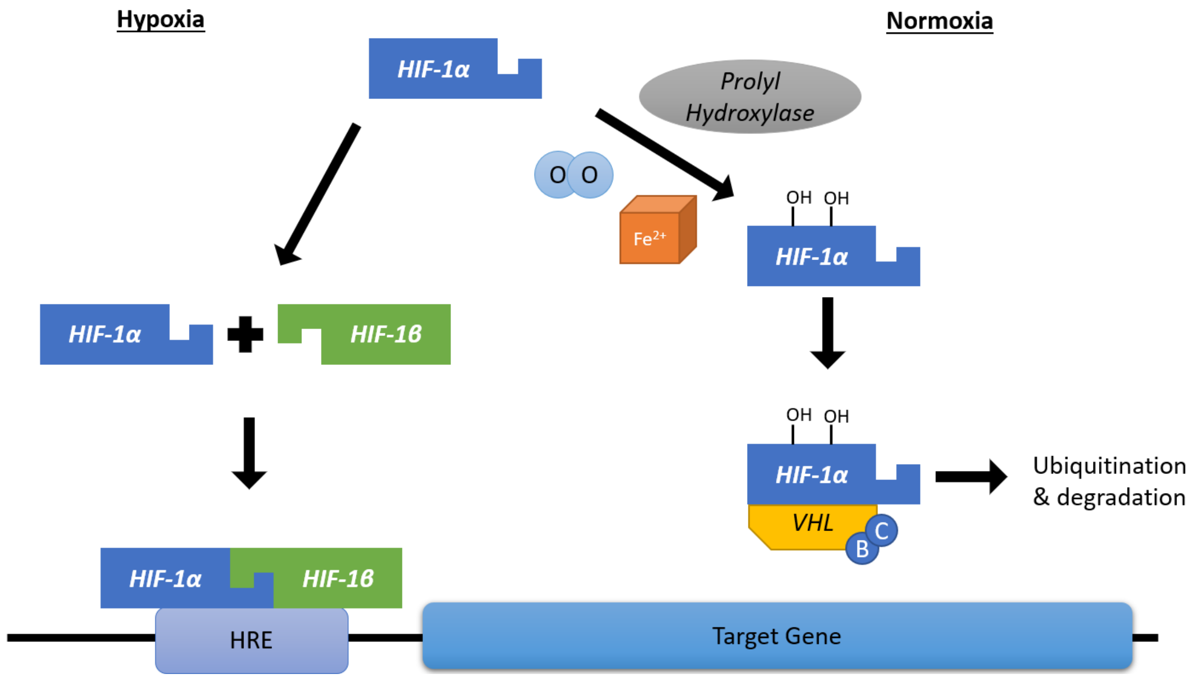

Figure 1.3 Schematics of the oxygen sensing mechanism and functions of hypoxia inducible factor-1α in the cell (Adapted from Harris, 2002)

II. I. II Downstream responses

HIF-1 mediates several biological pathways in response to hypoxia, including protecting the cells from damage by hypoxic stress, improving their survivability,[15,26] modifying the local tissue, and cell death (Table 1.1). One of the key expressions of HIF-1 is enhancing cell proliferation via initiating migration and regeneration by vascularization and erythropoiesis.[27,28] Hypoxic cells upregulate production of certain growth factors such as transforming growth factor β3 and vascular endothelial growth factor. These growth factors are sent and bind to the receptors of other cells such as the endothelial cells. Over time, new blood vessels are formed at the local tissue for increasing oxygen supply to the cells and thus alleviate the hypoxic stress. In the meantime, hypoxic cells also express growth inhibitory signals to other cell types, causing cell cycle arrest and suppression of apoptosis. These pathways protect the local tissue from increasing the demand of oxygen. Another important downstream response was the mediation of glucose metabolism. The preferred metabolic pathway swaps from the oxygen-required tricarboxylic acid (TCA) cycle to the oxygen-independent glycolysis despite significantly reducing the conversion from 38 ATP per glucose to only 2 ATP per glucose.[29] HIF-1 was also shown to be involved in regulating all the enzymes in the glycolytic pathway such as the glucose transporters, which increase the cellular glucose uptake.[29] Despite its role in anti-apoptosis, HIF-1 is also involved in pro-apoptosis pathways. It has been shown to upregulate the expression of pro-apoptotic protein NIP3,[30] as well as promoting p53-dependent apoptosis.[31] To improve the prediction of cell fate under hypoxia, it is beneficial to categorize the cause and duration of hypoxia.

Functions	***Gene products involved***
Angiogenesis	Plasminogen activator inhibitor 1 Transforming growth factor β3 Vascular endothelial growth factor (VEGF) VEGF receptor FLT-1
Apoptosis	BCL2 interacting protein 3 (NIP3)
Collagen metabolism	Prolyl-4-hydroxylase α(I)
Erythropoiesis	Erythropoietin
Glucose metabolism	Aldolase A, C Glucose Transporter 1, 3 Glyceraldehyde-3-P-dehydrogenase Hexokinase 1, 2 Lactate dehydrogenase A Phosphofructokinase L Phosphoglycerate kinase 1 Pyruvate kinase M Triosephophate isomerase
Iron metabolism	Ceruloplasmin Transferrin Transferrin receptor
Nucleotide metabolism	Adenylate kinase 3
pH regulation	Carbonic anhydrase 9
Proliferation and survival	Adrenomedullin Insulin-like growth factor (IGF) 2 IGF-binding protein 1, 2, 3 p21 Transforming growth factor β3
Regulation of HIF-1 activity	P35srj
Vascular tone	α_{1B}-adrenergic receptor Adrenomedullin Endothelin-1 Heme oxygenase-1 Nitric oxide synthase 2

Table 1.1 Pathways regulated by HIF-1 (adapted from Semenza, 2001)

II. II. Classification of hypoxia

Hypoxia is generally classified as chronic hypoxia and acute hypoxia. Chronic hypoxia is broadly defined as the gradual and persistent low oxygen environment which generally inflicts minimal harm to the tissue and renders local protective mechanisms. They include metabolic adaptation, local tissue remodelling via angiogenesis and erythropoiesis and autophagy. One typical example of chronic hypoxia is hypobaric hypoxia which may trigger high altitude sickness.[32] The reduced atmospheric pressure equates to reduced available oxygen for inhalation and thus triggers erythropoiesis and angiogenesis. This series of biological response is not lethal and is often exploited by the athletes competing in aerobic sports. High-altitude training before competitions helps them improve their performances at the sea level. Chronic hypoxia can also be naturally occurring in the body and has been reported in a myriad of mechanisms. It was reported and suggested to be involved in, but not limited to, preserving stemness of stem cell and progenitor cells,[33,34] maintaining efficient sodium reabsorption in the renal tubular[8] and signalling orientation in embryo maturation.[35,36]

Acute hypoxia refers to temporary and local shortage of oxygen which usually incurs more severe damage to the local tissue. The area of effect is generally more localized due to ischaemia and hypoxemia, commonly caused by aggregates, capillary ruptures and fibrin clots.[37] Transient and focal they might be, secondary damages occur at the surrounding tissue if not controlled in time. It has even been reported that reperfusion in an ischemic brain, a sudden return of blood flow to the hypoxic tissue, can cause more damage to the neurons than in ischemia.[38,39]

Yet it must be noted that these conventional and general classifications should not lead to stereotyping the nature of hypoxia nor the molecular and cellular responses. As mentioned in the previous section, the complexity and convoluting downstream response of HIF-1 could lead to multiple outcomes, depending on the health, age, and environment of the subject.[37]

II. III. Focal hypoxia and diseases

Focal hypoxia is always associated with a wide range of manifestations occurring in multiple diseases. Depending on the local tissue, hypoxia damages can be long-lasting even if reperfusion occurs within minutes. The human brain is one of the most susceptible organs to hypoxic stress. Hypoxia is known to be implicated in a few common central nervous system diseases such as stroke[13], Alzheimer's disease[16], hypertension[40] and traumatic brain injury.[41] Its susceptibility is accounted for by its lack of proper energy reserve and high energy consumption. Despite amounting to about 2% of the total body mass, the human brain consumes 20% of the total oxygen supply.[42,43] It can sustain its ATP consumption for only about 1 minute without blood flow so that sustained glucose and oxygen supply are therefore highly important.[44] It was reported in literature that minutes of hypoxia can cause severe neuronal damage.[42,45,46] Importantly, the complex, yet biased vasculature in the brain also causes some regions to be more vulnerable than the others.[47] Kirst et al. mapped the vasculature of a mouse brain and clearly showed that the white matter (where axons and myelin are located) has significantly less capillaries than the grey matter (where neuron cell bodies are located). In case of an infarct, white matter, being more distant to the blood supply, will likely be more stressed than the grey matter.

Focal hypoxia can also affect the effectiveness of therapies and prognosis of disease. Hypoxia has been reported in various types of tumours such as lung, prostate, and head and neck.[48] Due to the poor vasculature and uncontrolled cell growth, regions within the tumour exceed the diffusion limits of oxygen (>200μm) from the nearest capillary and create hypoxic and acidic microenvironments.[49] While radiotherapy has been utilized to combat tumours since 1896, its effectiveness was discovered to be greatly hindered by the hypoxic core of the tumour microenvironment.[50,51] Lack of oxygen radicals from molecular oxygen severely increased the radioresistance of the hypoxic microenvironments by 2.5- to 3- times.[52,53] Hypoxia activated prodrugs, such as tirapazamine[54,55] and its improved version SN30000,[56] have been investigated for their toxicity to cancerous cells, with the goal to create a chemoradiotherapy. It is therefore important to recognise the importance of focal hypoxia to cell mechanisms, disease pathophysiology and pharmacokinetics.

III. Modelling hypoxia

Modelling diseases requires a combination of interventions for recreating the local environment. Not only the delivery of metabolites like glucose and oxygen are disrupted in the pathological tissue, the removal of waste products such as carbon dioxide and lactate should also be addressed. The use of models allows strategic investigations of individual components and factors causing the cascade of manifestations in a disease. Essential to understand the role of hypoxia in diseases, it is important to create models for studying the pathophysiology and stress-response pathways of the local and surrounding tissue. Key to the hypoxia model development is to minimize and simplify the variables to maximize the translatability to the manifestations of the diseases. It may thus inspire and discover potential therapeutic pathways for interventions.

III. I. Animal models

Human models are extremely complicated to obtain ethically and even if so, it can never be guaranteed that experiments conducted do not inflict permanent damage. To model diseases, rat, mouse, pig, and many other animals have been used as animal models for studies. Animal models have long been a fundamental tool for investigating hypoxic-related diseases. They are an inherently complex model that offer a wide range of information including oxygen saturation,[57] arterial CO_2 concentration,[40] NO levels,[58] behavioural changes, and pharmacokinetics.[59] They are used extensively in studying pulmonary hypertension, hypoxia/reperfusion damages, cerebral hypoxic insults, and altitude sickness.[4] Commonly used methods can be classified into the use of gas chambers and surgical interventions.

Gas chambers administer hypoxia to subjects through hypoxic tents,[60] environmental chambers, and gas masks.[61] They are sub-classified into two major types based on the methodologies in hypoxia induction. Hypobaric chambers induce hypoxia by decreasing the atmospheric pressure below 1atm (760mmHg) whereas normobaric hypoxia chambers decrease the partial pressure of oxygen below 159mmHg, (20.9% of 760mmHg) by replacing with nitrogen.[32,60,61] These chambers are suitable for studying acute or chronic bulk hypoxia.

Surgical interventions offer higher flexibility to study ischaemia by restricting blood flow globally and locally. Oxygen transported via blood vessels to the brain can be reduced by methods such as carotid artery ligation, electrocoagulation, and injection of the vasoconstrictor endothelin-1.[62,63] These methods cause ischaemia and thus decrease in the oxygen supply. Hypoxic stress can be induced to the tissue or organ and injuries can be analysed in real time by MRI or post-operation by paraformaldehyde fixation. Reperfusion can also be studied by utilizing surgical procedures like the removal of occluding devices or bridging intact blood vessels to by-pass occlusions.[63]

Widely used though these animal models might be, there are a few underlying pitfalls that must be addressed. One of the major limitations is the difference in species. Fundamental differences are easily observed in cellular functions and expressions within an organ model,[64] structure of the organs,[65] and total masses of the organisms. Experimental results may thus expect varying translatability to human diseases.[66] Besides, many of these models generate global hypoxia that can be difficult to reflect the pathophysiology of focal hypoxia occurring in, for example, the cerebral white matter. This also limits the investigation of secondary damages, such as glutamate release and microglia activation, which have been documented in diseased patients. Other limitations include the differences in pharmacology and toxicology, variations within animal strains and high cost.

III.II. *In vitro* models

In vitro models offer a promising alternative to the animal models. The establishment of controls and assumptions and standardizations allow thorough investigations at the cellular, biochemical and molecular level that are more convoluted to accomplish in animal models.

III. II. I. Chemical hypoxia models

One of the most common methods used in *in vitro* hypoxia models is achieved by introducing chemicals into the culture medium. This method is the most accessible way for studying hypoxia without needing additional apparatus to modulate the ambient oxygen concentration level. The upregulation of HIF-1α can be studied by using chemicals such as cobalt chloride, dimethyloxaloglycine (DMOG) and deferoxamine (DFO).[67] These chemicals interfere with different stages of the HIF-1α degradation process. DMOG was reported as a PHD competitive inhibitor and was suggested to act analogously to the PHD co-substrate 2-oxoglutarate. DFO blocks PHD activity by chelating the co-factor Fe^{2+}.[68] This results in a lack of Fe^{2+} available for hydroxylation for VHL recognition, leading to HIF-1α accumulation. Co^{2+}, on the other hand, acts as the substitute of Fe^{2+} and inhibits the PHD activity.[67] Stabilized HIF-1α under these chemicals, is thus allowed to dimerize, translocate to the cell nucleus, and bind to HRE for increasing the transcription activity.[69] HIF downstream responses can be investigated.

Despite the convenience of chemicals, their applications are limited due to the fundamental differences in the mechanism and ignoring the ambient oxygen concentration. Artificially increasing HIF-1α transcription activity results in untranslatable experimental results to actual pathophysiology occurred under hypoxic stress. They can adversely interfere with other pathways and result in false deductions of hypoxia-ischaemia.[70] Application of chemicals is usually non-localized, so that hypoxic gradients cannot be established for studying more in-depth cellular and molecular investigations.

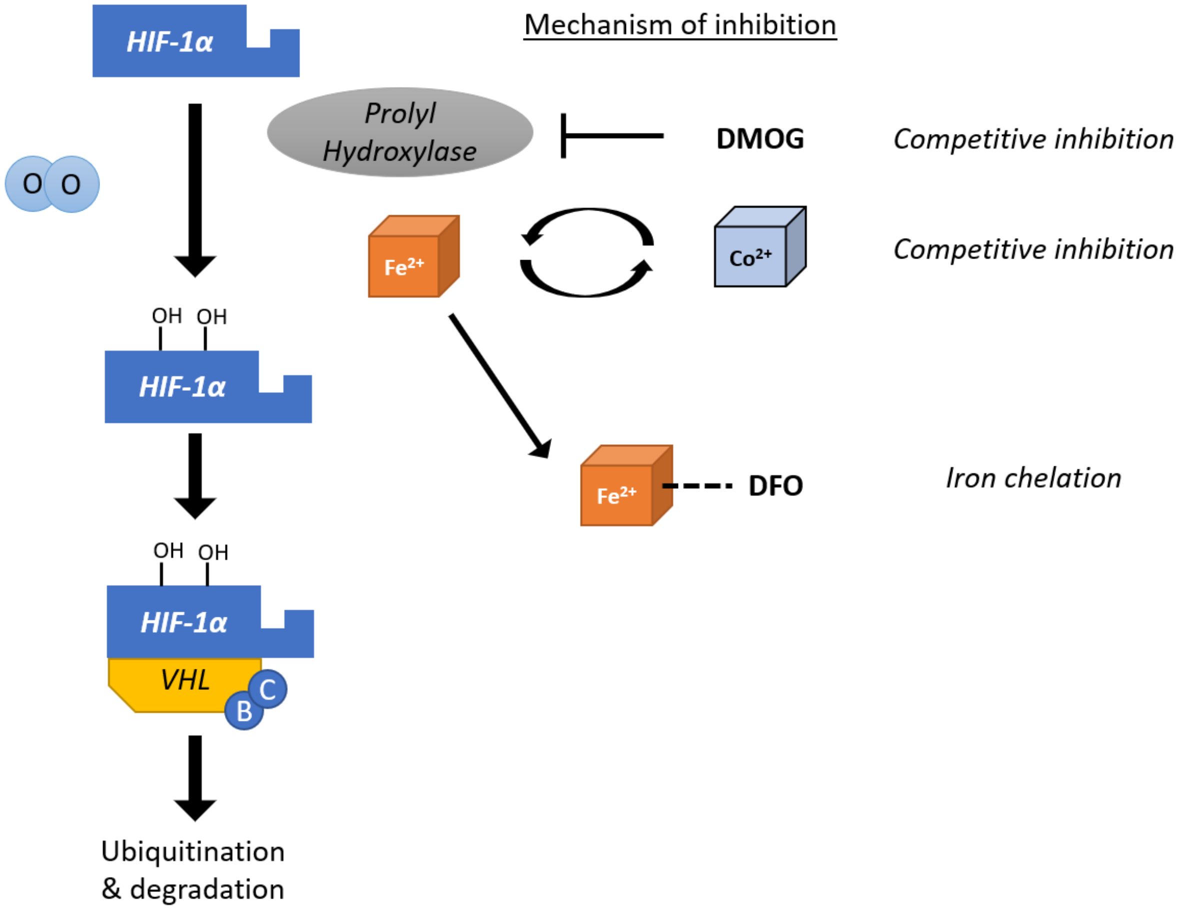

Figure 1.4 Schematic presentation of the inhibition mechanism by DMOG, cobalt ion and DFO to HIF-1α degradation.

III. II. II. Enzymatic oxygen scavengers

Enzymatic oxygen scavenging methods are commonly used for generating hypoxia in cell models but more so in food preservation and super-resolution microscopy techniques.[71,72] The working principle of enzymatic hypoxia in cell cultures is by combining the catalytic pathways of glucose oxidase (GluOx) and catalase. Fast kinetics of GluOx was exploited in the presence of glucose in the culture medium, consuming oxygen by the reduction reaction with glucose to produce gluconolactone and hydrogen peroxide, the latter was then removed by catalase.[72,73] Yet, the turnover of dissolved oxygen against oxygen diffusion from ambient is in question, meaning that it works best in closed containers with sufficient time provided but not so much in open area within a short period of time.[74] Besides, gluconolactone produced can significantly increase the acidity of the medium that increases the necessity of buffering for extended oxygen scavenging duration.[71]

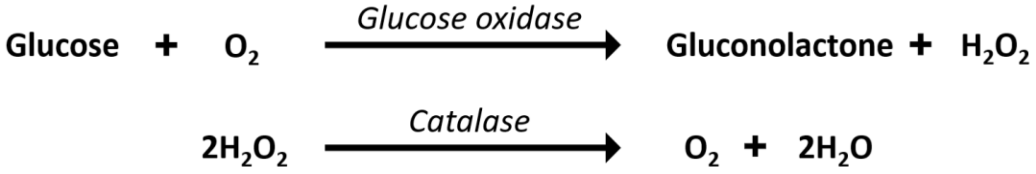

Figure 1.5 Oxygen scavenging reaction catalysed by glucose oxidase and catalase.

III. II. III. Diffusion hypoxia models

Another commonly used method for creating hypoxia is the diffusion approach. Premixed gas and gas cylinders can be used to change the ambient oxygen concentration inside low oxygen incubators, hypoxic chambers, and workstations. Its ease of set-up and better translatability to chemical hypoxia increased its employment in hypoxia research. Yet, these methods are limited by their single hypoxic level, slow oxygen diffusion rate and absence of hypoxic gradient.[75] Other approaches attempted to overcome these limitations by exploiting the slow oxygen diffusion with plastic inserts[76] and increasing the oxygen consumption with high cell densities.[73,77,78] However, the applications of these approaches are limited, due to the high variation of oxygen consumption rate amongst different cell types, creating difficulties in applying robust hypoxia. Its lack of oxygen concentration variation within the culture also decreases its value in hypoxia studies.

III.II. IV. Microfabrication in Cell Cultures *in vitro*

Microfabrication is an emerging field that possesses the versatility to overcome some of the limitations of existing hypoxia cell models. One major advantage of microfabrication is to improve the degree of control in oxygen delivery to the cells, creating a tightly controlled gradient platform. Most of the microfluidic designs integrate with similar principles as above, to alter oxygen concentration levels with better spatiotemporal control, focal and intermittent hypoxia.[79] Delivery of equilibrated culture medium and oxygen scavengers are common approaches in generating hypoxia.[80,81] Compartmentalization in microfluidic systems are also popular solutions in generating a hypoxia gradient. By exploiting the fast oxygen diffusion coefficient of oxygen in PDMS, parallel channels and multi-layered devices are beneficial in perfusing gas and separating the toxic oxygen scavenging chemicals from the cell culture.[82–85] Some applications even include a hydration chamber to reduce the solution evaporation due to constant gas flow.[86]

To create these complex oxygen modulating devices, laser engraving, additive printing and photolithography are common fabrication techniques, with each of them having their advantages over another. Laser engraving and additive printing are best for 3-dimensional device fabrication but are constrained by their dimension limits whereas photolithography offers the best accuracy and fine resolution for pattern development. The former two methods have resolutions at 10μm while photolithography has better than 100nm resolution.[87,88]

One major limitation of the current microfluidics research is that many of the reported systems did not pay enough attention to how *in vitro* cell culture practices were commonly performed, as well as the interests of biologists. The narrow channel systems offer little to no room for cell loading and studying cellular and molecular functions. They also require bulky off-chip equipment such as gas tanks, syringe pumps, tubing and actuators.[89] Source of contamination also increases due to the interfaces with this extra equipment involved. These limitations thus unfortunately decreased the attractiveness of the technique, prompting more effort and communication between the engineers and biologists.

IV. Electrochemical scavengers

Electrochemistry offers an unexplored alternative approach to the study of cellular hypoxia, in removing dissolved oxygen efficiently and continuously. Previously, removal of electrochemical interferents electrochemically has been reported in the literature. Hahn et al. created the nitrous oxide and halothane anaesthetic gas sensor prototype by introducing a metalized membrane electrode to filter oxygen, which has the same reduction potential as halothane on silver surfaces.[90] Similarly, Bacon et al. created a sandwich electrode system for ascorbate in a glucose sensor.[91] An outer scavenging membrane electrode was installed to remove ascorbic acid which interferes with the detection of hydrogen peroxide, generated by the glucose oxidase located at the inner electrode. A prototype for indirect electrochemical removal of dissolved oxygen in a flow through system was also demonstrated by Marei et al. for advancing the detection of negatively reduced metals in water quality control.[92] Oxygen was removed by a silver electrode after passively diffusing across a silicone membrane. Although the applicability of the prototype is in doubt due to the material selection, electrochemistry has proven its use in scavenging dissolved electrochemically active species.

Removal of dissolved oxygen in the culture medium could potentially be an extended application of electrochemical scavenging. It may be possible to create localized hypoxia by controlling the O_2 diffusion layer within the cell culture. This potentially gives hope and inspiration in furthering our understanding of oxygen related biological processes and disease pathophysiology.

V. Rationale and aim of research

Investigation and understanding of acute focal hypoxia have been lacking in the literature despite their importance in the physiological system and the pathophysiology of diseases. This is at least in part, due to the absence of a system able to create a satisfactory model for acute focal hypoxia and representative oxygen gradients. It is of paramount importance to develop a robust methodology capable of generating focal hypoxia with an oxygen gradient for translating the technical feasibility to biological application. Animal *in vivo* models offer great potential but have fundamental differences with human beings. *In vitro* cell models offer an essential starting point with high flexibility and relevance for unravelling the cellular, molecular, and biochemical interactions.

The overall aim of the thesis was to develop a hypoxia control system to create an *in vitro* focal hypoxia cell model, for investigating cell-molecule and cell-cell interactions under focal hypoxic insults. The particular final aim of the project was to develop a human cerebral microinfarct model where axons were under hypoxic insult whereas the cell bodies were under normoxia. It was proposed that this method would provide the basis and framework for other acute hypoxia research.

The approach taken in this thesis was to investigate the feasibility in scavenging dissolved oxygen in the cell culture electrochemically and thus developing a controlled oxygen gradient within the single cell culture. In my previous research, a few electrode materials were tested previously and the best electrode material for oxygen scavenging, based on kinetics, application flexibility and robustness, was selected for further investigation in the physiological conditions required for cell culture.[93] The starting point of the research reported in this thesis leads on from this selection and is focussed on a Pt/C sintered electrode preparation (Chapter 2). An electrochemical cell was designed for optimizing the generation of oxygen gradient, evaluated by the resultant oxygen concentration at the base of the cell.

The effectiveness of the approach was first applied to the human neural progenitor cell model as a proof of concept (Chapter 3). Human neural progenitor cells were selected for their resilience to hypoxic insult, to demonstrate the temporal effectiveness in generating a hypoxic environment for cell culture. Hypoxic gradient response was used to evaluate the effectiveness in creating focal hypoxia in the cell culture. HIF-1α upregulation will be used as the readout of achieving hypoxia, whereas DMOG can be used in this thesis as positive controls.

Further preliminary investigation of the effect of focal hypoxia on human cortical neurons by simulating the cerebral structure was undertaken (Chapter 4). A compartmentalized microchannel device was designed and developed for separating neuron cell bodies and axons. The hypoxia system was integrated into the culture device to establish hypoxia at the axons and cellular responses were investigated.

Chapter 2: Oxygen scavenging with electrochemistry

I. Introduction

In this chapter, the use of electrochemistry for creating focal low oxygen in the solution was investigated. Attempts to achieve spatiotemporal control of hypoxia is commonly overlooked in animal hypoxia models and *in vitro* cell models despite the significance of acute focal hypoxia proven by CT, MRI, or post-mortem neuropathology. Long equilibration time, toxicity and/or untranslatable cellular mechanisms caused by chemicals are known disadvantages of conventional hypoxia models. The oxygen reduction reaction, one of the most extensively studied reactions in electrochemistry, has the potential of overcoming these drawbacks.

The oxygen reduction reaction is widely used in fuel cell technology, and oxygen sensors, in environmental and medical applications.[94–97] This reaction has two major pathways in aqueous solution: the direct 4-electron reduction pathway to produce H_2O (eq. 2.1) and the indirect 2-electron reduction pathway to produce H_2O_2 (eq. 2.2) that can further be reduced to H_2O (eq. 2.3).[98] It is highly complicated that the mechanism pathway primarily depends on the nature of the electrode material, electrolyte and ambient conditions.

The direct 4-electron pathway at more acidic pH:

$$\mathrm{O_2 + 4H^+ + 4}e^- \rightarrow \mathrm{2H_2O} \tag{2.1}$$

$$\mathrm{O_2 + 2H^+ + 2}e^- \rightarrow \mathrm{2H_2O_2} \tag{2.2}$$

$$\mathrm{H_2O_2 + 2H^+ + 2}e^- \rightarrow \mathrm{2H_2O} \tag{2.3}$$

In alkaline pH

$$\mathrm{O_2 + 4H_2O + 4}e^- \rightarrow \mathrm{4OH^-} \tag{2.4}$$

And the ‘peroxide’ pathway:

$$\mathrm{O_2 + H_2O + 2}e^- \rightarrow \mathrm{2HO_2^- + OH^-} \tag{2.5}$$

$$\mathrm{HO_2^- + H_2O + 2}e^- \rightarrow \mathrm{3OH^-} \tag{2.6}$$

Platinum has been considered as one of the best catalysts for oxygen reduction so that the mechanism has been extensively studied.[99–103] O_2 reduction primarily undergoes the 4-electron reduction mechanism.[104] Its superb oxygen reduction catalysing capacity is explained by the balance of adsorption energy and desorption energy on the substrate, intermediate and product, evident in the volcano plot (fig. 2.1).[97] While many of its oxygen reduction reaction properties were investigated in extreme pH and high temperature to elevate the current density generated by the electrode, application to cell cultures are restricted to the physiological pH 7.35-7.45 and 37°C. Biocompatibility of the electrolyte also restricts the choice of background electrolyte from using hypochlorite ions (ClO^-) or other ions that would be toxic to biological cells, thereby sacrificing the oxygen scavenging efficiency commonly observed and desired in fuel cells.[105] The thermodynamic potential of the oxygen reduction reaction on platinum is 1.23 V (vs NHE).[98] This highly anodic potential causes surface material oxidation and complications in oxidizing metabolites and protein.[106]

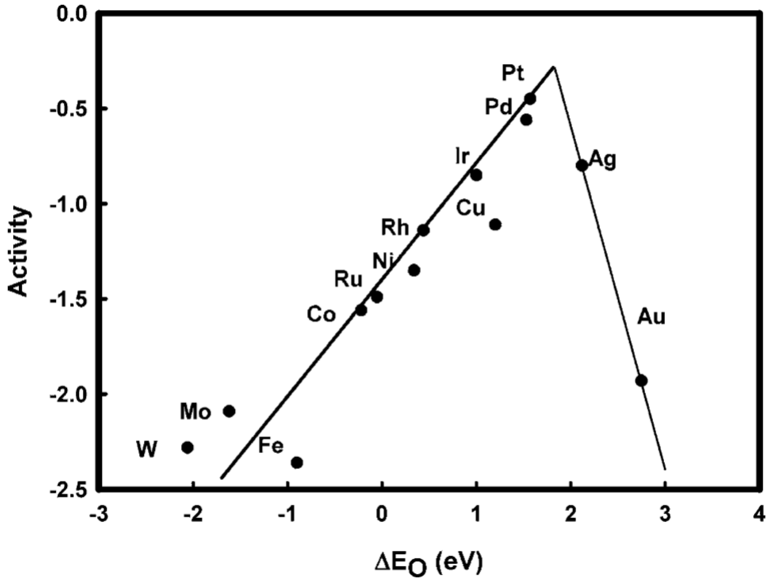

Figure 2.1 Volcano plot presenting trend in oxygen reduction activity plotted against the function of oxygen binding energy. Increasing oxygen binding energy (right of X-axis) infers less spontaneous reactions. Increasing activity (upwards of Y-axis) implies stronger overall oxygen reduction reaction activity on the surface of the material. Plot reprinted from Nørskov et al., 2004.

Gold is also another kind of material widely used for the oxygen reduction reaction, particularly in the synthesis of hydrogen peroxide and in oxygen measurements.[107] One major advantage of the gold electrode is that the hydrogen evolution reaction occurs at a more cathodic potential that does not interfere with the oxygen reduction reaction under a wide range of pH.[108] The oxygen reduction reaction at physiological pH is suggested to occur via a mixture of the 2-electron reduction pathway and 4-electron reduction pathway producing hydrogen peroxide and water (fig. 2.2).[104] These pathways are not independent by the fact that the 4-electron reduction pathway proceeds through the hydrogen peroxide intermediate.[109]

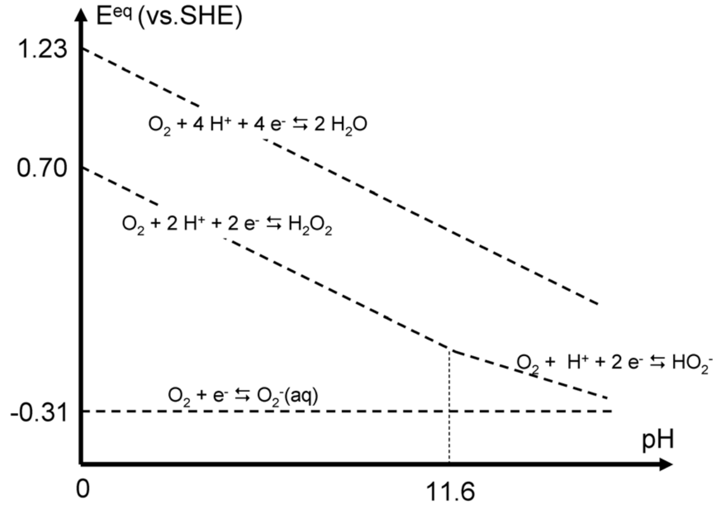

Figure. 2.2 Schematic Pourbaix diagram of oxygen reduction reaction pathways on gold. Reprinted from Rodriguez. P. and Koper M. T. M. (2014).

To pick a material for oxygen scavenging in the culturing conditions, the material properties for the oxygen reduction reaction in biocompatible electrolyte should be compared. It is necessary to consider the material's electrochemical window, physiological stability, efficiency in oxygen reduction, flexibility in reshaping, and cost.

Previous preliminary study investigated the properties of a gold disk electrode, an electrodeposited gold nanoparticle on ITO electrode (AuNP/ITO) and a 5% platinum / graphite (Pt/C) electrode.[93] Expectedly, all materials selected showed catalytic activity towards the oxygen reduction reaction in the electrochemical window, evident from varied oxygen content in the 0.1M KCl electrolyte (fig. 2.3). CVs with a gold disk working electrode showed a broad peak at –0.4V vs Ag/AgCl, whereas CVs with an AuNP/ITO electrode showed two oxygen reduction peaks at –0.5V and –0.8V vs Ag/AgCl. The CV with Pt/C showed a current increase due to the increase in O_2 concentration.

Since all materials were capable of scavenging oxygen, the current densities and the kinetics of each material were compared. The current densities were calculated from the geometric surface area for comparing oxygen removal per unit area and presented in the given potential range in figure 2.4. The gold disk electrode had a lower overpotential than AuNP/ITO. Yet, its current densities matched from –0.8V. Pt/C had the highest current density at all potentials in the window. It was also seen that Pt/C had high background current, which is associated with the high capacitance of this electrode.

Selection of materials depends on the final application. For a scavenging material, high scavenging ability is the most important factor of consideration. Current density, quantifying the turnover of electrons and thus oxygen scavenged, is the dominant factor for consideration than the other electrochemical properties. Based on the results presented, Pt/C showed superiority in oxygen scavenging to the other two materials investigated. For a sensing electrode in this thesis, the primary interest is the local oxygen concentration experienced by the human cells (approx. diameter of 10–100 μm). An electrode with matching small diameter is preferred. The material should also be stable for an extended period (for hours) in the electrolyte or culture medium. Gold wires are thus preferred for sensing in this thesis.

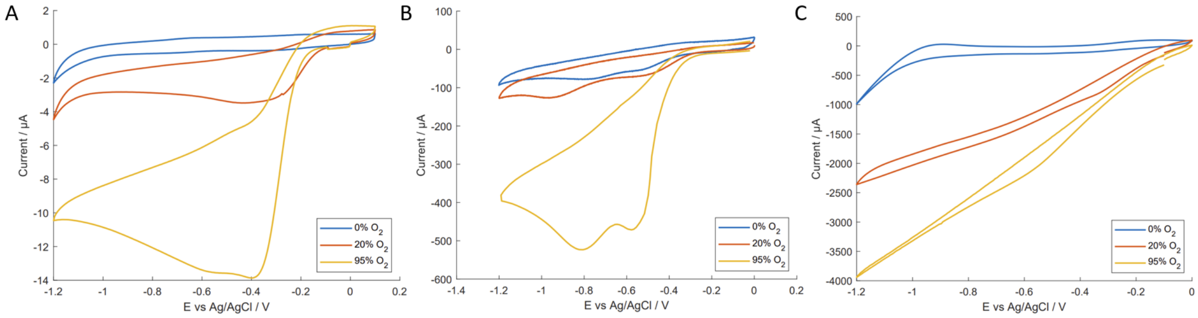

Figure 2.3 Cyclic voltammetry of different material in air and degassed 0.1M KCl. A: Gold disk electrode (scan rate: 50mV/s), B: AuNP/ITO electrode (scan rate: 100mV/s); and C: Pt/C electrode (scan rate: 20mV/s). CV of AuNP/ITO electrode in degassed electrolyte had gas leakage, leading to the increase in Faradaic current by the oxygen reduction reaction. Note that the Y-axes of the A, B and C are on different scales.

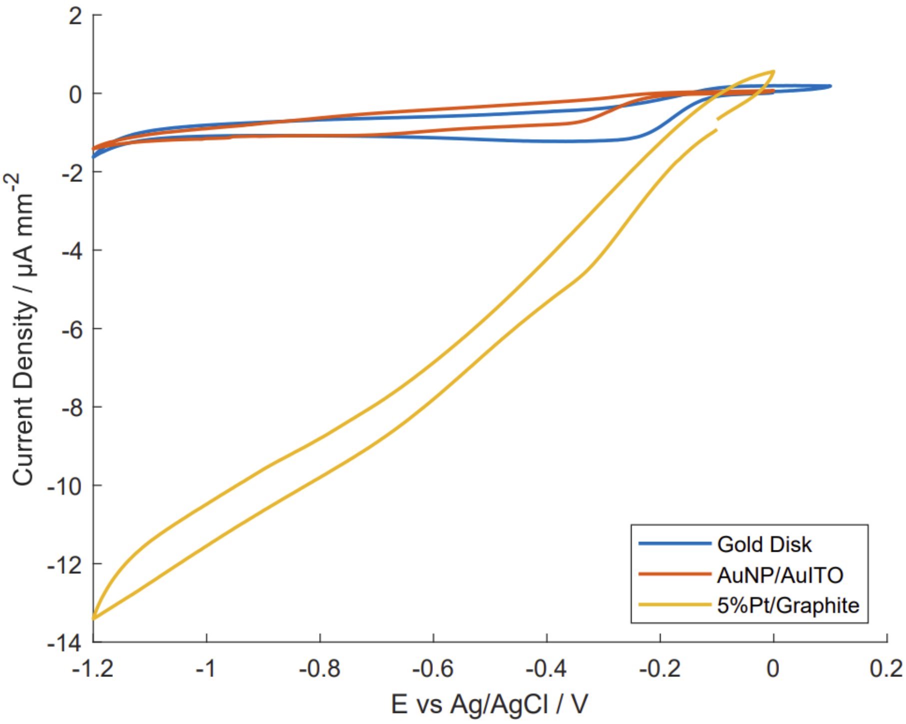

Figure 2.4 Cyclic voltammetry of gold disk, AuNP/AuITO and Pt/C in 0.1M KCl at 50mV/s. Current density was calculated with respect to the geometric surface area.

To further investigate the kinetics of the oxygen reduction reaction on different materials, the previous study also investigated with pseudo-Tafel plots (figure 2.5) and the results are summarised in table 2.1. [93] In both cases of gold electrodes, one Tafel slope was observed before reaching the diffusion-controlled potential. Gold disk and AuNP/ITO had similar Tafel slopes of 84mV/Dec and 106mV/Dec, respectively, and demonstrated the same exchange current density at –6.1. The second Tafel slope would be consistent with the mixed materials on this electrode, showing a steep 2454mV/Dec. This may be related to the reduction of Sn in the ITO, which was also observed in other work from the lab.[110] Pt/C showed a Tafel slope at 306mV/Dec with exchange current densities at –4.17. The absence of the second Tafel slope commonly observed on platinum-containing materials could be related to overlapping with that of hydrogen evolution reaction due to the high scan speed.[98] This two Tafel slope phenomenon has been attributed to the surface change from a Pt/PtO surface at high potentials to the reduced Pt surface at lower potentials, changing the rate determining step from the first electron transfer to the pseudo two-electron transfer.[98,99]

All of the Tafel slopes reported in the previous study deviated from the literature values.[98] This suggested that they might be influenced by recording at 20mV/s scan rate, which is known to produce pseudo-higher slopes. A slower scan rate is recommended for better analysis of the catalytic kinetics. Still, the experimental results suggested that Pt/C had a higher current density and superior catalytic activity for the oxygen reduction reaction compared to gold disk and AuNP/ITO electrode. Pt/C was therefore selected as the main candidate of investigation in this thesis.

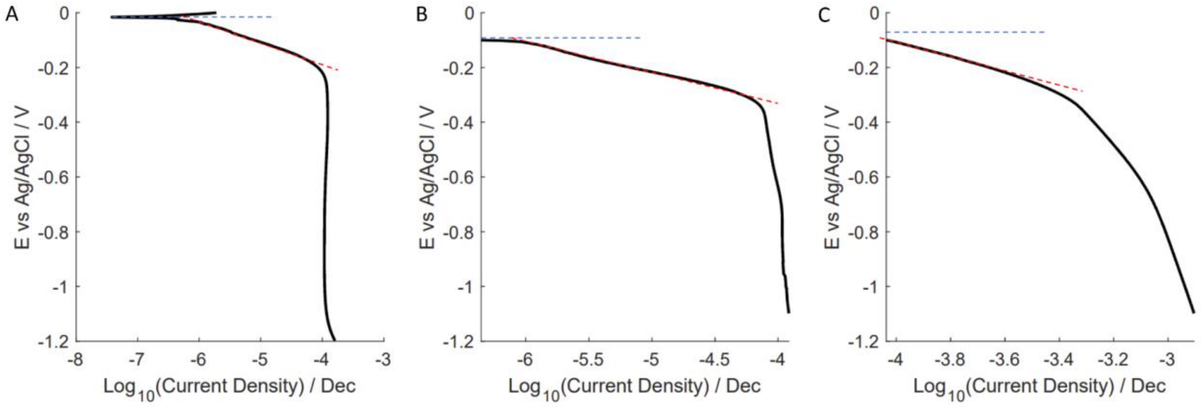

Figure 2.5 Tafel plot of gold disk (A), AuNP/ITO (B) and Pt/C (C) electrode in 0.1M (20mV/s). The dotted lines were fitted lines for equilibrium potentials (blue) and oxygen reduction Tafel slopes (red). Current

densities were calculated from the geometric surface area. The exchange current density denotes the equilibrium of the reaction (no net electrolysis) at the potential. Overpotential away from the equilibrium shifts the energy barrier height that positively correlates to the speed of electrochemical reaction.

Electrode	**Tafel slope(s) (mV/Dec)**	**Exchange current density ($\log(i_0)$)**
Gold Disk	84	–6.12
AuNP/ITO	106	–6.07
5% Platinum / graphite	306	–4.17

Table 2.1 Pseudo-Tafel slopes and exchange current densities of different electrodes in 0.1M KCl, calculated from cyclic voltammogram at 20mV/s.

In this chapter, Pt/C was further investigated for its properties and applicability for oxygen scavenging in culture medium. The Pt/C electrode has been demonstrated in the literature for catalysing the oxygen reduction reaction but most of these studies were conducted in high temperature and either strong acidic or alkaline conditions. Herein, the oxygen reduction reaction and other properties of Pt/C in physiological settings were further characterized and investigated. A scavenging device (electrochemical cell) was built for housing the electrode system and for cell culturing. Investigation of its spatiotemporal modulation of oxygen concentration was thus conducted.

II. Materials and methods

II. I. Materials

The chemicals purchased from Sigma-Aldrich are listed as follow: phosphate buffer saline (PBS), potassium phosphate dibasic, potassium phosphate monobasic, potassium chloride, ferrocyanide and 30% (v/v) hydrogen peroxide solution.

II. II. Equipment and instrumentation

The equipment used for electrochemical studies are the µStat 400 Bipotentiostat/Galvanostat from DropSens and the multichannel potentiostat MultiEmStat3 (4 channels) from PalmSens, Formlabs 3D printer was used for printing parts for the electrode array. FEI Nova NanoSEM scanning electron microscope (SEM) was used to analyse the material topography and atom distribution.

II. III. General electrochemistry techniques

II. III. I. Cyclic voltammetry

Cyclic voltammetry (CV) was used to detect the redox reaction occurring at the working electrode. Potential is swept from the beginning potential to the first potential (V_1), then reversed to the second potential (V_2) and ends at the starting potential to complete a cycle. The sweep speed, also known as the scan rate, was constant throughout the sweeping process. The resultant current was measured by the potentiostat and plotted against the potential with respect to the reference electrode potential. This technique is particularly useful for understanding the redox reaction, chemical reaction and adsorption/desorption occurring on the working electrode in the electrochemical system.

The reversibility of the redox reaction can be visualized by CV by measuring the potential of the oxidation peak E_{ox} to reduction peak E_{red} separation. The peak currents I_{ox} / I_{red} were measured by obtaining the difference between the projected baseline current towards the respective E_{ox} and E_{red}. Analyzing chronologically with repeated scans can also shed information into the underlying chemical / physical reactions that cannot be observed in the first scan. For a fully reversible reaction ($E_{ox} - E_{red} = 59/n\ mV$ at 25°C), the Randles-Sevcik equation can be used as follows:

$$\mathrm{i_p} = 0.4463\mathrm{nFAC}\left(\frac{\mathrm{nFvD}}{\mathrm{RT}}\right)^{\frac{1}{2}} \tag{2.7}$$

As for an irreversible/quasi-reversible redox reaction ($E_{ox} - E_{red} > 59/n\ mV$ at 25°C), the Randles-Sevcik irreversible equation is:

$$\mathrm{i_p} = 0.4961\mathrm{nFAC}\left(\frac{\alpha\mathrm{nFvD}}{\mathrm{RT}}\right)^{\frac{1}{2}} \tag{2.8}$$

In which,
$\mathrm{i_p}$: Peak current (A)
n: Number of electrons in the redox reaction
F: Faraday's constant (C $\mathrm{mol^{-1}}$)
A: Electrode area ($\mathrm{cm^2}$)
C: Concentration (mol $\mathrm{cm^{-3}}$)
R: Gas constant (J $\mathrm{mol^{-1}}$ $\mathrm{K^{-1}}$)
T: Temperature (K)
D: Diffusion coefficient ($\mathrm{cm^2}$ $\mathrm{s^{-1}}$)
α: transfer coefficient of the redox reaction
v: Scan rate (V $\mathrm{s^{-1}}$)

II. III. II. Chronoamperometry

Chronoamperometry (CA) is a measurement of current over time in which a fixed potential step was applied to the working electrode. In this thesis, polarization potential was set at the diffusion-controlled potential learned from CV, so that the kinetics of the working electrode at the set overpotential was not a limiting factor to the redox reaction. The diffusion current can be expressed as the Cottrell equation:

$$\mathrm{i_p} = \mathrm{nFAC}\left(\frac{\mathrm{D}}{\pi\mathrm{t}}\right)^{\frac{1}{2}} \tag{2.9}$$

II. III. III. Chronocoulometry and Anson plot

Chronocoulometry (CC) is a similar analytical method as CA but expresses the cumulated charge passing the working electrode over time. It is particularly useful over CA for long-term analysis due to the increasing differences in measurements over time and the analysis of the adsorbed species on the electrode material. The Anson equation describes the charge passing through the electrode based on diffusion:

$$Q_{diff} = 2nFACD^{\frac{1}{2}}\pi^{-\frac{1}{2}}t^{\frac{1}{2}} \tag{2.10}$$

The Anson plot is a plot of charge against square root of time. Interpretation of the graph allows possible separation of catalysis of the electrochemical species from the sum of double layer charging (Q_{dl}) and the adsorbed molecules (Q_{ads}), which can be resolved from the projected intercept of the plot. The total charge recorded from the potentiostat can be expressed by:

$$Q_{total} = Q_{diff} + Q_{ads} + Q_{dl} \tag{2.11}$$

The difference between measured intercepts from both the presence and absence of the adsorbed species can be used to calculate Q_{ads}, assuming Q_{dl} is constant in both cases. Surface concentration of adsorbed species (Γ_0) is calculated from Q_{ads} based on the following equation:

$$Q_{ads} = nFA\Gamma_0 \tag{2.12}$$

II. III. IV. Tafel plot

The Tafel plot is used to represent the electrochemical kinetics of the material, displaying the relationship between overpotential and logarithmic current density. The Tafel slope, the projected straight line, was utilized to describe the rate of electrochemical reaction to the overpotential. The equilibrium potential of the system can then be determined by the intersection of the Tafel slope and horizontal line projected from the converging potential.

$$\eta = A \times \log_{10}\left(\frac{i}{i_0}\right) \tag{2.13}$$

$$\alpha = \frac{RT}{nFA} \tag{2.14}$$

In which,

η: overpotential (V)

A: Tafel slope (V Dec^{-1})

i: current density (A m^{-2})

i_0: exchange current density (A m^{-2})

α: electron transfer coefficient

II. III. V. Electrochemical reversibility

Electrochemical reversibility (Λ) discusses the relationship of charge transfer and mass transfer. The faster the charge transfer relative to the mass transfer, the more reversible the reaction is. According to Bard and Faulkner, the reversibility of the reactions is defined by the ranges of reversible ($\Lambda \geq 15$), quasi-reversible ($15 \geq \Lambda \geq 10^{-2(1+\alpha)}$), and irreversible ($\Lambda \leq 10^{-2(1+\alpha)}$). It is defined by the ratio of standard rate constant (k^0) to mass transfer, which is dependent on the scan rate ($(DFv/RT)^{1/2}$.)

$$\Lambda = \frac{k^0}{\left(\frac{DFv}{RT}\right)^{\frac{1}{2}}} \tag{2.15}$$

$$i_0 = Fk^0 \tag{2.16}$$

II. IV. Electrodes

II. IV. I. Platinum / graphite (Pt/C) electrode

The Pt/C electrode used in the study was provided by Alphasesnse, The Sensor Technology Company, Great Notley, Essex, from which the electrode was designed and fabricated. Platinum was dispersed into ground-graphite with surfactant and mixed with PTFE and then heated to remove water and surfactant and then sintered in an aluminium cup near the melting point of PTFE. It was then pressed through the aluminium cup into a Gore membrane (Ø: 16mm) at ambient temperature. The aluminium cup was then discarded, leaving the Gore-supported Pt/C electrode. The finished product was then modified to suit the electrochemical cell. An opening was pinched through the electrode for a copper wire to pass through. Minimal amount of silver epoxy was used to bind both parts together for electrical conductivity and allowed to dry overnight. Normal epoxy was used to cover the silver epoxy exposed and allowed drying overnight before using (fig. 2.6). The electrodes were always cleaned with 70% ethanol and distilled water before experiments. The diameter of the electrode, including the non-catalytic region, was 16 mm while the catalytic area was 14mm. A small rectangular indentation of about 2mm^2 was cut for placing the reference electrode in close proximity to the working electrode surface. The Pt/C electrode was stored in room temperature under ambient air overnight before studying adsorbed oxygen.

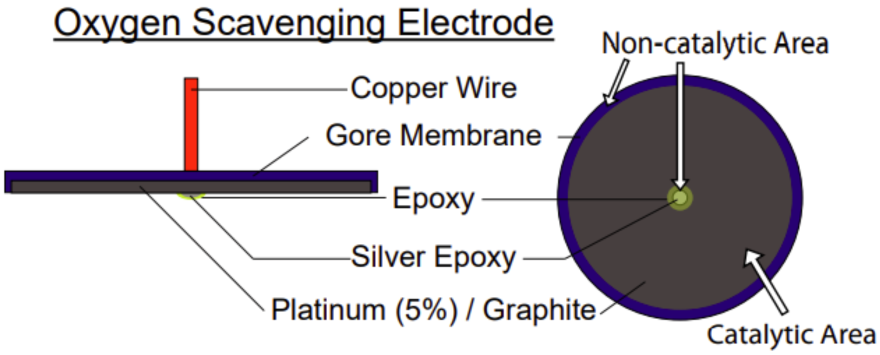

Figure 2.6 Schematic diagram of the platinum / graphite electrode

The centre and the rim of the Pt/C electrode were also analysed separately. A biopsy punch (8mm diameter) was used to punch out the centre of the electrode. Both parts were first connected to a copper wire, same as the procedure above. Nail varnish (two-layer coating) was used to cover parts of the electrode surface in contact to the electrolyte.

II. IV. II. Clark electrode array

A Clark electrode and a Clark electrode array were used to measure oxygen concentration changes at the base of the electrochemical cell under the oxygen scavenging process. The Clark electrode, designed and fabricated by previous lab members, was a 99.99+% purity gold wire of 125µm diameter encased in the amber epoxy resin of 6mm diameter. The multielectrode system was designed in this thesis for robustly investigate the oxygen concentration gradient established by the oxygen scavenging system. Gold wires of 125μm diameter at 99.99+% purity (Goodfellow) were chosen for its oxygen reduction reaction properties, low background capacitance, consistent performance of gold over time and fine diameter for more dominant radial diffusion over planar diffusion whilst balancing the ease of handling by its moderate rigidity. The Clark electrodes were positioned 0.5mm apart across the 17mm base for a good spatial mapping of the oxygen gradient. The Clark array was formed by four 3D printed blocks. Together they encased the gold electrodes which were soldered on a custom-made printed circuit board (PCB). 3D printed blocks were printed with UV-curing clear resin in a Formlabs 3D printer. Gold wires were first coiled around a 3D printed block with ridges to retrain the wire movement (fig. 2.7). The second piece of 3D printed block was bound to the gold-coiled block with the resin. The assembly was placed in a UV box for 3 hours at 60°C to allow crosslinking between the two pieces. A scalpel was used to cut the wires apart, creating a short end for sensing and a long end for soldering to the PCB (fig. 2.8). The double-sided PCB was designed with 16 contact points on each side, making a total of 32 connections (fig. 2.9, fig. 2.10, fig. 2.11). Gold wires on the assembly were alternately soldered onto each side of the PCB (fig. 2.11). The PCB was attached to the overlaying resin by a 3mm bolt and nut. The gold wire parts were filled with UV-curing resin and placed in the UV box for a total of 8 hours at 60°C in which the assembly was flipped every 2 hours. The final product was slotted into a 36-pin PCB edge connector (Fig. 2.12). Silver epoxy was added to each PCB-pin connection to enhance conductivity. Support was received in fabricating the printed circuit board by the Department of Engineering and the 3D printed models by the Department of Chemical Engineering and Biotechnology. The assembly of the electrode array, the soldering and other work were my own effort.

Prior to experiments, the Clark electrode and the electrode array were polished and cleaned. They were first rinsed in deionised water and then polished sequentially in 1.0μm and 0.3μm alumina slurry on a polishing pad for 5 minutes each. After each abrasive, any adsorbed particle was removed by placing the array under running deionized water and then pressured nitrogen gas, followed by a 30-second polish on a clean damp polishing pad. To fix the Clark electrode at the base, a 6mm hole was created at a PDMS base, which was subsequently adhered to the PDMS wells (see section II. V. IV.). For the Clark electrode array, PTFE thread sealing was used to circle the cylindrical part of the electrode array three times. The array was then pushed towards into the hollow PDMS cell culturing well (see section II. V. V.) of 17mm diameter (method similar to that described later but with a cylindrical mould) and became the base of the assembly, fixed to the desk with Blu Tack.

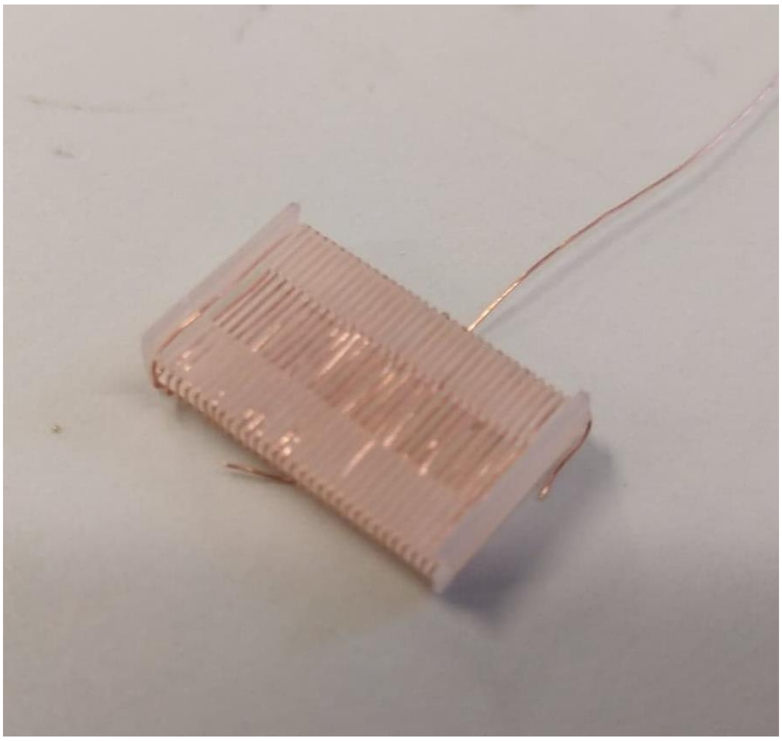

Figure 2.7 Gold wire (125μm) coiled around the central piece of 3D block. Ridges to fix gold wire position is 500μm apart.

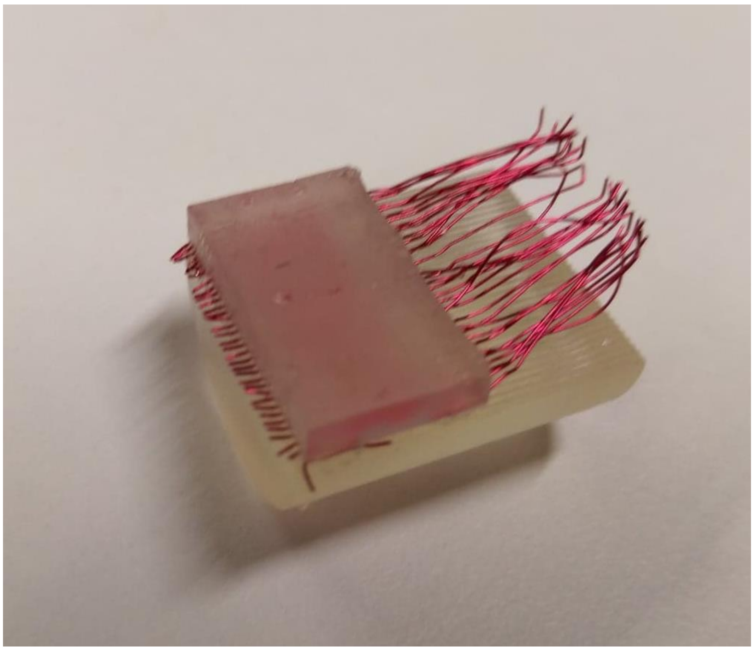

Figure 2.8 Assembled sensor illustrated with copper wires.

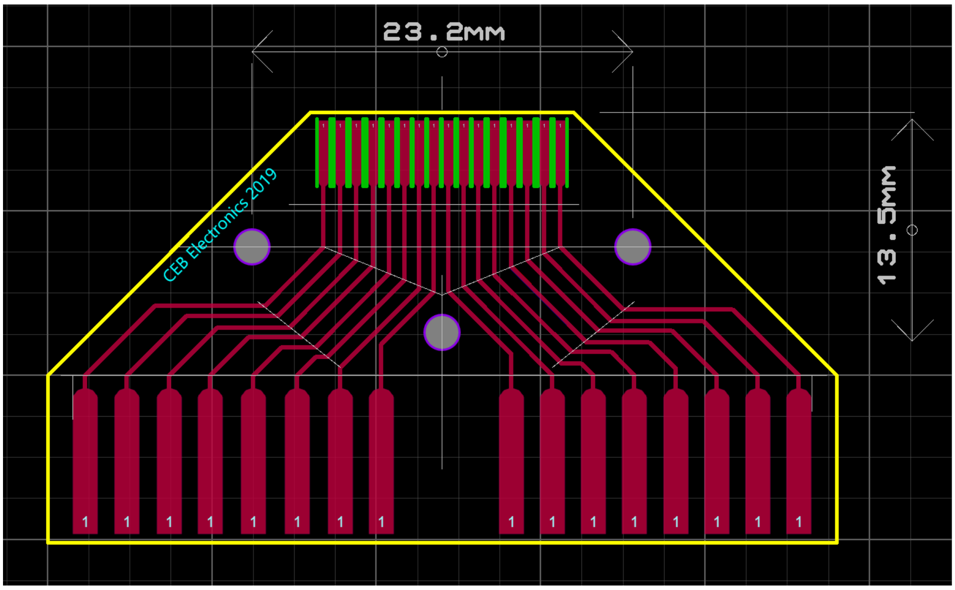

Figure 2.9 Schematic diagram of the PCB design. Design was the same for both the top side and the bottom side.

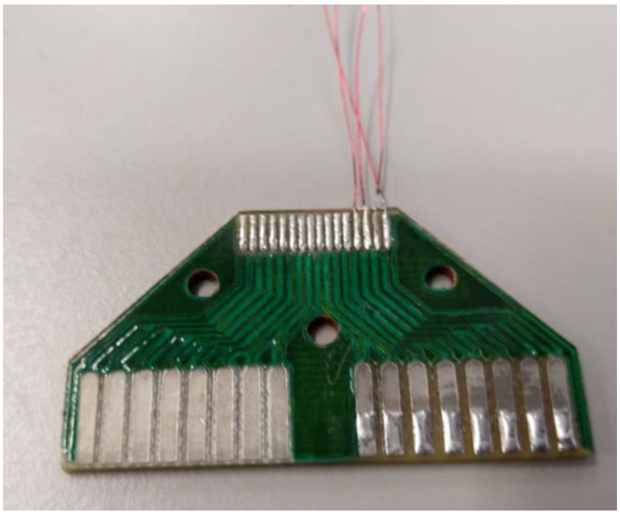

Figure 2.10 Final product of the PCB with copper wires soldered for testing

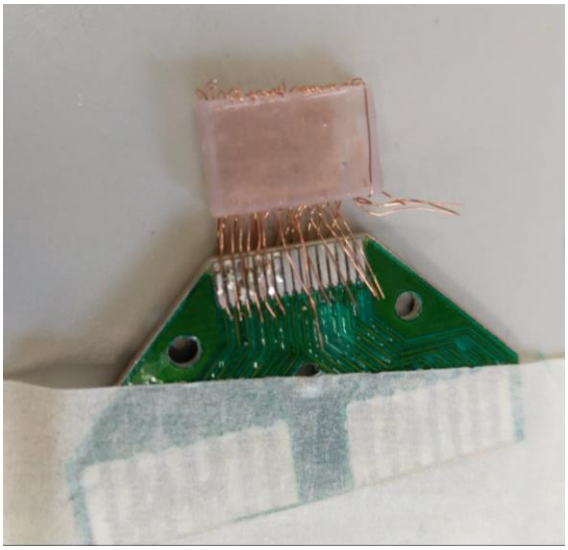

Figure 2.11 Soldered wires on the PCB.

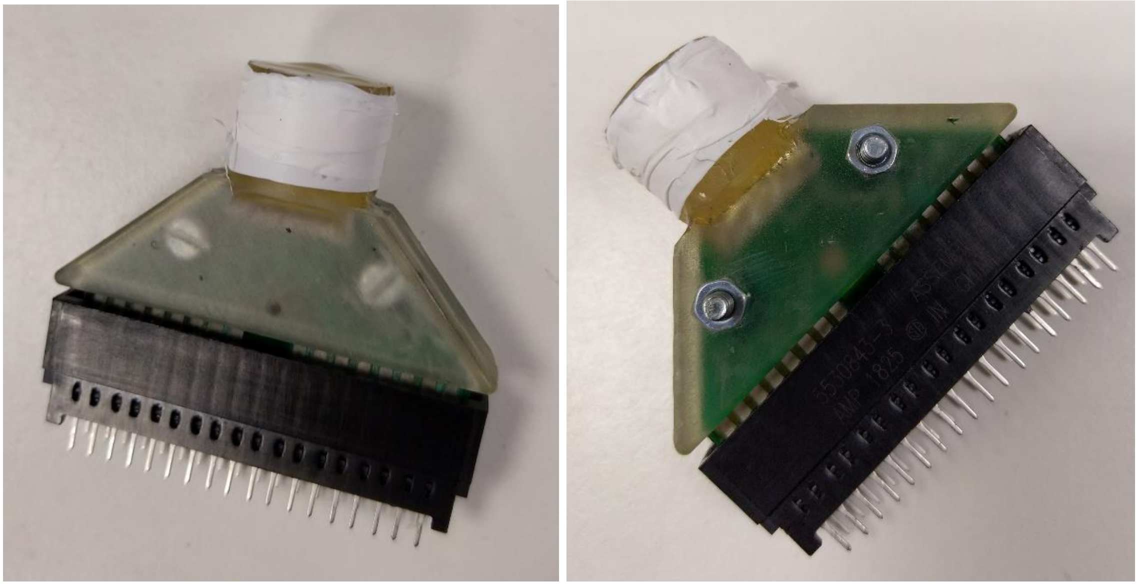

Figure 2.12 Clark array finished product attached to a 36-pin edge connector. Left: front; right: back. Teflon tape covering the insert to prevent liquid leakage.

II. IV. III. Other electrodes

The silver / silver chloride (Ag/AgCl) was obtained from Harvard Apparatus Ltd. The electrode was pressed against a copper wire and covered with epoxy. Prior to experiments, it was rinsed with water and dried with nitrogen gas. The platinum coil counter electrode of 5 mm diameter was obtained from GoodFellow Cambridge Ltd. It was cleaned from impurities by heating under the Bunsen flame.

II. V. Oxygen reduction reaction in electrochemical cell

II. V. I. Characterization of Clark electrode for oxygen measurement

Clark electrodes were characterized in 40mM phosphate buffer pH 7.4 with 100mM potassium chloride (PBKCl) unless stated otherwise. CV measurements were conducted in air and degassed electrolyte, which was conditioned by bubbling N_2 gas for 30 minutes and keeping an overhead N_2 gas flow. Clark electrodes were subsequently polarised at –0.5V (vs Ag/AgCl) for oxygen measurements under 0% O_2, 5% O_2, 10% O_2, 20.9% O_2 and 30% O_2 in the hypoxia chamber shown above. Gas was equilibrated for 3 hours before recording the respective current measurements. A calibration curve was plotted for relating current to the oxygen concentration level. A calibration curve for the Clark electrode polarized at –0.7V (vs Ag/AgCl) was also generated for measurements in PBS.

II. V. II. Characterization of Pt/C electrode

Pt/C electrode was characterized in PBKCl and culture medium N2B27(–) (composition please refer to chapter 3 section II. III.). PBKCl was equilibrated as reported above in either air or nitrogen at room temperature whereas N2B27(–) was equilibrated 4 hours in an incubator with 5% CO_2 / Air or 5% CO_2 / 0% O_2 / N_2 at 37°C. CV measurements were conducted in all conditions of electrolytes and the oxygen reduction reaction peak was identified. The centre and rim of the Pt/C electrode were characterized with CV (n = 3). The current densities were calculated and compared by dividing the respective geometric surface areas.

To determine the polarization potential in N2B27(–), Pt/C was polarized at –0.6V, –0.7V and –0.8V for 5 minutes in air and nitrogen. Pt/C was polarized at –0.7V in the subsequent oxygen scavenging experiments. An adsorption study was conducted by placing the Pt/C electrode in air overnight before conducting the stepwise –0.7V CC measurements. Second measurements with fresh electrolyte were conducted back-to-back and the Anson plot was used to distinguish the amount adsorbed on the electrode through comparison of charges (Q_{ads}).

II. V. III. Electrochemical cell set-up

A PDMS cell culturing well (Ø: 17mm) was designed to accommodate the electrode system. The wells were created by fixing plastic cylinders with double-sided tape on a 55mm petri dish. PDMS was used to fill up the space till about 1.5mm height. After polymerization, the plastic cylinders were removed, and the cylindrical wells were created on the petri dishes. For electrodes to pass through into the wells, three holes were created in the lid by either drilling or melting. The working electrode (Pt/C), reference electrode (Ag/AgCl) and counter electrode (Pt coil) were fixed by Blu Tack and placed in the well as illustrated in the schematics below (fig. 2.13). All electrodes were connected to the bipotentiostat controlled by a computer. To measure low oxygen, the assembly was placed inside a hypoxia chamber created from an air-tight food container with two openings (fig. 2.14). A top opening was for wire connections whereas a side opening near the base was for gas inlet under constant flow.

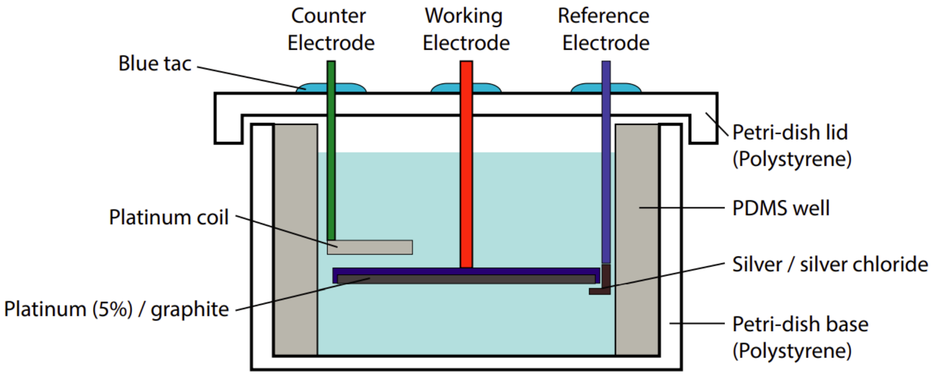

Figure 2.13 Schematic diagram of the electrochemical cell set up.

Figure 2.14 Hypoxia chamber for gas equilibration.

II. V. IV. Oxygen equilibration in incubator

Efficiency of oxygen equilibration in the incubator was investigated. Electrodes were prepared as previously described in characterization experiments. To simulate culture medium without gas pre-treatments, PBS was equilibrated in ambient for 8 hours before using as electrolyte. Oxygen concentration was measured with the Clark electrode in the PDMS container inserted inside a PS container and placed in the 5% O2 incubator (fig. 2.15). The Clark electrode was polarized at –0.7V for 5 hours. Three separate measurements were performed and time required to reach circa 5% O2 was averaged.

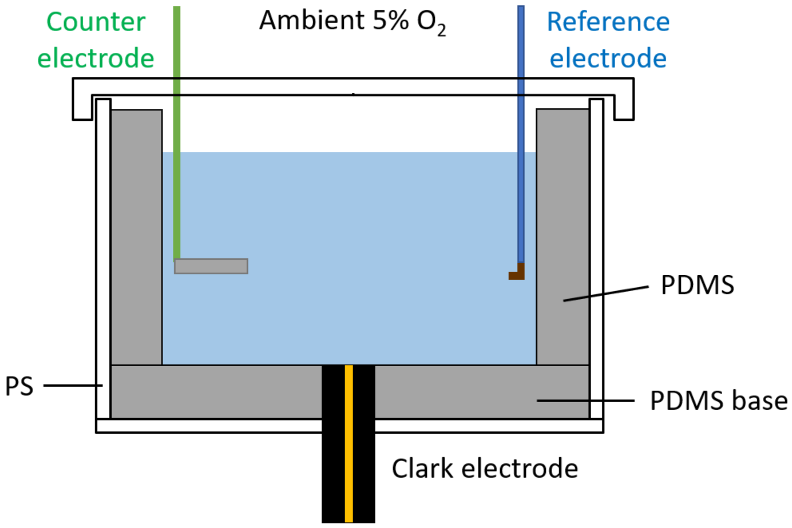

Figure 2.15 Schematic diagram of the set up used for investigating PBS oxygen equilibration from 20% O_2 to 5% O_2 ambient in incubator. Clark electrode was polarized at –0.7V.

II. V. V. Oxygen gradient characterization

1.7 mL of electrolyte was added to the electrochemical cell, resulting in the electrolyte depth of 8mm. The Clark electrode fixed at the base was used to measure the residual O_2 concentration. It was polarized at –0.5 V for 3 minutes to stabilize the current and obtain a background oxygen measurement, prior to the connection and polarization (–0.7 V) of the Pt/C electrode at the oxygen reduction (scavenging) potential. Measurements were conducted in 5% O_2 concentration obtained with a 5% O_2/N_2 balance premixed gas cylinder. The scavenging efficiency was then studied by varying the position of the Pt/C electrode within the PDMS cell at 1mm, 2mm and 3mm distance from the bottom of the well (fig 2.16). The current from individual electrodes in the Clark electrode array was recorded, placed at 0, 2 and 6mm radial distances from the centre of the culture well. This allows investigation of the uniformity of oxygen concentration across the base under the oxygen scavenger at different distances above the base.

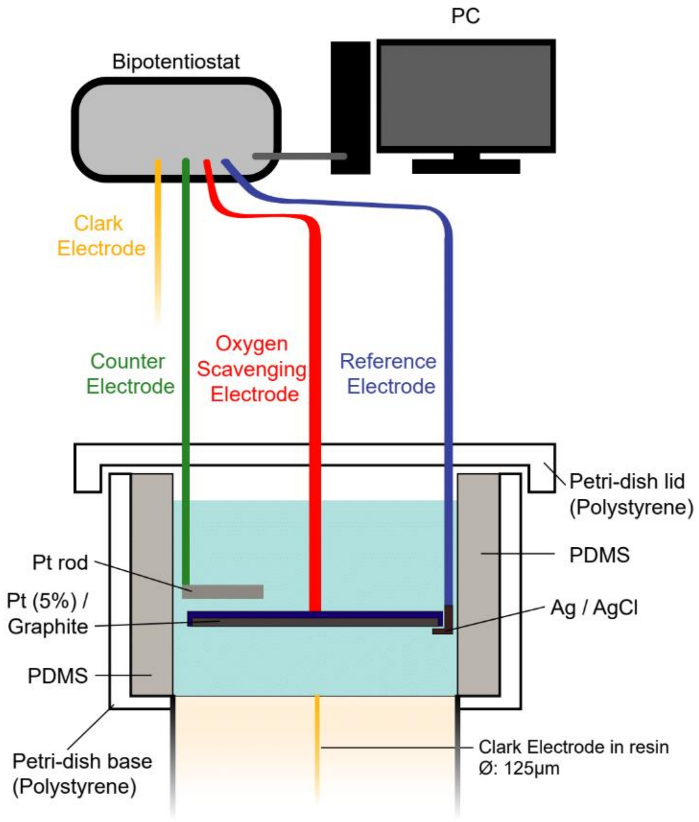

Figure 2.16 Schematic diagram of the assembly of the electrochemical set up with Clark electrode (array) as the oxygen sensor. The electrodes are connected to a bipotentiostat for current measurements.

The oxygen gradient was also investigated in the electrochemical cell with the Pt/C electrode cut into halves and connected to the wire as previously described. The electrode was positioned at 2 or 3mm in height from the base, at one side of the electrochemical cell. A clean and freshly polished Clark electrode array was used to measure the steady state oxygen concentration with the bipotentiostat. The Clark electrode at the centre of the array (electrode number 7/8/9/10) was selected first and polarized at –0.5V for current measurement. After 2 minutes of current stabilization, the Pt/C scavenging electrode was polarized at –0.7V. After 30 minutes of oxygen scavenging, Clark electrodes from the array were selected randomly and current was measured for 2 minutes each, until all 16 positions were measured. The recorded current, normalized against the first 120 seconds as 20.9% ambient O2, were plotted against their respective positions.

II. VI. BET surface area analysis

The BET surface area analysis was conducted for studying the surface area and surface properties of the material of interest. The Quantachrom NOVA Station A instrument was used for data acquisition 53 mg of 0.01359cc of Pt/C was used for the analysis. The material was subjected to outgassing for 3 hours at 300°C. The nitrogen adsorption and desorption isotherm on Pt/C was conducted at 77.35K. Parameters of the adsorbate used for the calculation are listed below. Quantity of absorbed gas was plotted against the relative pressure. The BET equation and molecular cross section area were used to calculate the specific surface area of Pt/C ($\mathrm{A_{spec.}}$), fitted from $0.04 < \frac{P}{P_0} < 0.3$. The BJH method and de-Boer t-method were used to calculate pore radius and micro pore volume measurement. Data points below $\frac{P}{P_0} < 0.35$ were ignored.

$$\frac{1}{W\left(\left(\frac{P_0}{P}\right)-1\right)} = \frac{1}{W_mC} + \frac{C-1}{W_mC}\left(\frac{P}{P_0}\right) \tag{2.17}$$

$$\mathrm{Slope} = \frac{C-1}{W_mC} \tag{2.18}$$

$$\mathrm{Intercept} = \frac{1}{W_mC} \tag{2.19}$$

$$A_{BET} = \frac{W_m N A_{N_2(CS)}}{M_{N_2}} \tag{2.20}$$

Where:

W: weight of gas adsorbed per gram of material

$\frac{P}{P_0}$: relative pressure

W_m: weight of gas adsorbed in monolayer per gram of material

C: BET constant (7.124)

$A_{BET.}$: specific surface area or BET surface area ($m^2\ g^{-1}$)

N: Avogadro's number (6.022e23)

$A_{N_2(CS)}$: adsorption cross section of the adsorbing species (16.2 $Å^2$)

M_{N_2}: the molecular weight of the adsorbate gas (28.013 g mol^{-1})

II. VI. Scanning electron microscopy

Scanning electron microscopy (SEM) was used to investigate the surface topography and the composition differences of the Pt/C material. The modes used for analysis were secondary electron detection with settings at 5kV, 5.0 spot size, and 4.7mm working distance with through-the-lens detector (TLD); whereas the backscattered electron detection settings were 5kV, 5.0 spot size and 5.0mm working distance with circular backscatter detector (CBS). SEM micrographs were kindly taken by Dr. Fernando Daniel León-Cázares.

III. Results and discussions

III. I. Characterization of 5% Pt/C electrode

III. I. I. Topography of Pt/C

The topography of the Pt/C electrode was investigated with the SEM (fig. 2.17). There were clear visual differences between the centre and the surrounding area of the electrode (fig. 2.17A). This difference relates to the manufacturing process of the electrode. The centre had black colour in the SEM, whereas the surrounding had a dull silver surface. This is consistent with the sintering process, whereby the PTFE – Pt/C solution in an aluminium cup, is heated to near the melting point of PTFE; during the evaporation and sintering, material migrates from the centre and collects more towards the outside of the cup, also collecting slightly up the walls of the cup. It is then pressed onto Gore, producing an electrode with a thickness gradient from the outside to the centre (thinnest in the centre). SEM micrographs taken at the centre where the electrode is thinnest, showed a heterogenous layer with no obvious surface pores (fig. 2.17B). There were also long parallel lines on the surface. These patterns are commonly seen on mechanically cut metallic surfaces and probably arise from the aluminium cup. When the material was pressed on the Gore membrane, the pattern may be carried over. Cracks were also observed on the surface with a wide dispersion of high intensity regions (fig. 2.17C). The brighter regions are expected to be PTFE, which was used as the binding material, whereas the darker region would be graphite. This is supported by the publication by Kunz and Gruver (1975), in which they showed the electron photomicrograph of a microtomed platinum supported on Vulcan.[111] The surrounding area where, during the evaporation and sintering process pushed material from the centre of the cup, showed a very different surface structure (fig. 2.17D,E,F), rougher than that of the central region (fig. 2.17D). Flakes of graphite were stacked in layers, analogous to SEM micrographs of ground graphite in the literature.[112–114] The higher magnification micrograph showed that pores smaller than 1μm in size were formed between the graphite flakes (fig. 2.17D inset). It was more evident in the backscattered electron images that the pores exist in the region (fig. 2.17E). It was also obvious that there were significantly less bright PTFE regions on the surface compared to the centre. This is consistent with the evaporation as the sintering begins, which leaves a higher deposition of PTFE in the centre. In the higher magnification backscattered electron image (fig.2.17F), a thin layer of high atomic weight particles was observed covering the graphite surfaces. According to a technical report by Prof. Michael Hitchman (2012), platinum aggregates dispersed on the material surface are expected, consistent with the observations of high atomic weight particles. It was evident that Pt/C had a heterogenous rough surface with small pores, which could be beneficial for electrochemical reaction. More thorough investigation of the surface area and pore sizes were conducted with BET surface area analysis (see section III.I.III.).

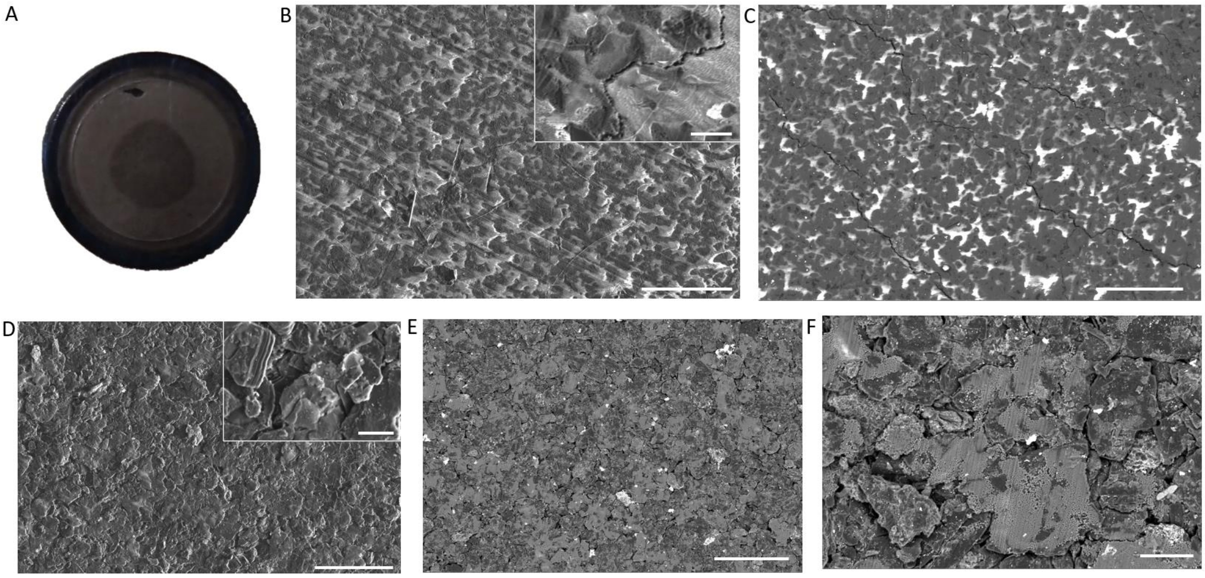

Figure 2.17 A: Camera image of the Pt/C material. Centre of the material has a duller surface than its surrounding. Dark blue rim is the gore membrane. B,C: Representative SEM micrographs of the centre of Pt/C material. B: Secondary electron micrograph at 500x magnification (scale bar: 50µm) and inset was at 5000x magnification (scale bar: 5µm). C: Backscatter electron micrograph of the centre of the material (scale bar: 50µm). D,E,F: Representative SEM micrographs of the dull silver colour region around the centre of Pt/C electrode. D: Secondary electron micrograph at 500x magnification (scale bar: 50µm) and inset was at 5000x magnification (scale bar: 5µm). E,F: Backscatter electron micrograph of the region around the centre. E: Zoomed out micrograph (scale bar: 50µm). F: Zoomed in micrograph (scale bar: 5µm).

III. I. II. Oxygen reduction reaction

The oxygen reduction reaction on the Pt/C was investigated with linear sweep voltammetry in phosphate buffered KCL electrolyte (PBKCl) and culture medium N2B27(–) (fig. 2.18). At 1mV/s scan rate, the oxygen reduction reactions were observed in both electrolytes in air and in nitrogen. In PBKCl, two reduction peaks were observed at –0.15V and –0.3V (vs Ag/AgCl), whereas only one reduction peak was observed at –0.35V in N2B27(–). No peaks were observed in the nitrogen equilibrated electrolyte, proving their relevance to oxygen reduction reaction.

On top of the oxygen reduction reaction, the hydrogen evolution reaction was observed in both electrolytes in all conditions. Hydrogen evolution ($2H^+ + 2e^- = H_2$) on platinum is one of the fastest electrocatalytic processes.[115] The Pt/C electrode used showed hydrogen evolution from –0.75V (vs Ag/AgCl), seen from the linear sweep voltammetries in figure 2.18. The potential was more negative (cathodic) than the planar polycrystalline Pt electrode and nanostructured platinum electrode measured in similar conditions. P. Daubinger *et al.* measured the potential range on Pt in PBS (pH 7.4) and hydrogen evolutions of both electrodes begin by circa 0V and circa –0.3V (vs R.H.E.)[116]. By calculating E^0 of Ag/AgCl with respect to R.H.E. in 0.1M KCl at 25°C (Eq. 2.21)[117], hydrogen evolution on Pt/C shifted by –0.5V compared with the planar polycrystalline Pt. The shift of potential can be attributed to the high graphite percentage and the dispersal of low content platinum nanoparticles, reducing the active sites of Pt-H formation and hydrogen evolution. The production process for the Pt/C electrode does not seek to control the exposed planes of the Pt. However, it is reported that such Pt nanoparticles mainly exhibits a face-centred cubic phase (although five centred symmetry is also predicted) with a mixture of exposed planes.[118,119] As different planes have different hydrogen evolution reaction performances, the mixture of planes is expected to have different kinetics to the polycrystalline Pt.[120] The influence of pH, although important to these reactions, is expected to be minimal as both media were buffered. With this electrode formulation, the available potential window maximized the range for diffusion-controlled oxygen reduction reaction without reaching the potential for hydrolysis of water / hydrogen evolution.

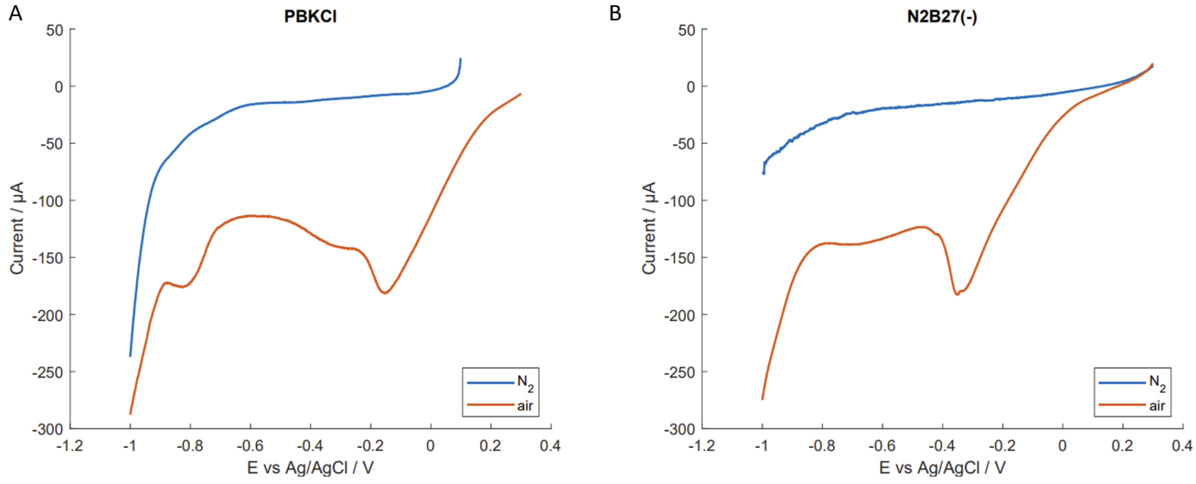

Figure 2.18 Linear sweep voltammetry of Pt/C electrode in PBKCl (A) or N2B27(–) (B) in air and in nitrogen at 1mV/s. Scans were from 0.3V to –1.0V (vs Ag/AgCl), apart from the LSV in degassed PBKCl started from 0.1V.

$$E_{AgCl/0.1MKCl}(RHE) = 0.23755 - 5.3783 \times 10^{-4} \times T(°\mathrm{C}) \\ -2.3728 \times 10^{-6} \times \left(T(°\mathrm{C})\right)^{2} + 2.2671 \times 10^{-4} \times T(K) \quad (2.21)$$

The oxygen reduction peak was investigated by cyclic voltammetry as shown in fig 2.19A and fig 2.20A. The scan rates were varied from 1mV/s to 30mV/s. It was evident that the diffusion peak potential becomes more cathodic in both electrolytes when scan rates were increased. In PBKCl, the diffusion limiting oxygen reduction peak was observed at –0.2V (vs Ag/AgCl) at 1mV/s and shifted to –0.7V at 30mV/s, similarly occurred in N2B27(–) from –0.3V to –0.7V, respectively. This was a significant feature of the slow irreversible kinetics of the oxygen reduction reaction undergoing an inner sphere electron transfer.[121] The absence of oxidation peak in the anodic scan and the shift of peak potential are indicative of the irreversibility of the oxygen reduction reaction.

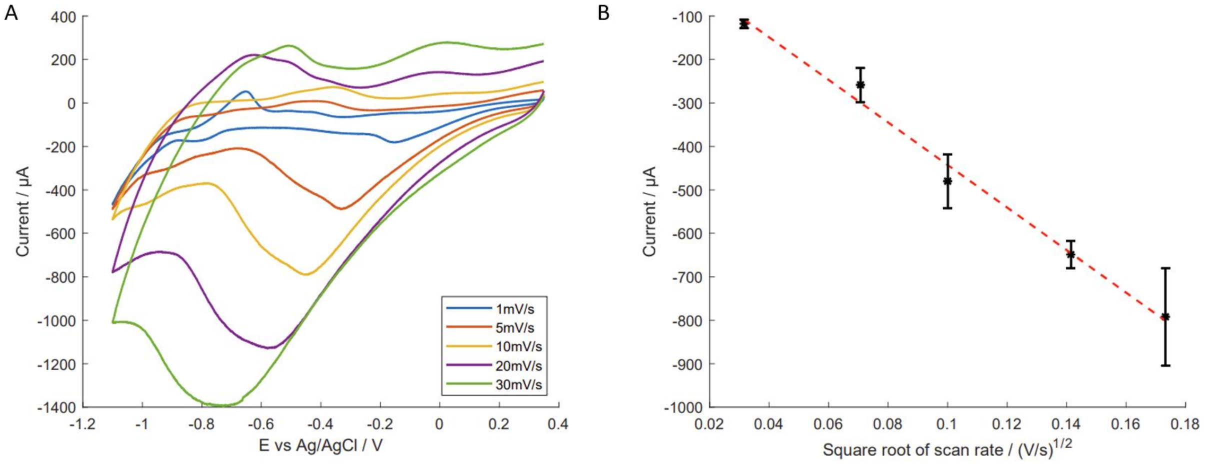

Figure 2.19 (A) Cyclic voltammetry of Pt/C electrode in air PBKCl under various scan rates (1 mV/s to 30 mV/s). (B) Plot of Pt/C electrode oxygen reduction peak current against square root of scan rate. Projected linear curve (red dotted line) is displayed on the image. The equation is $y = -5.71\times10^3x + 40.9$ ($R^2 = 0.9893$).

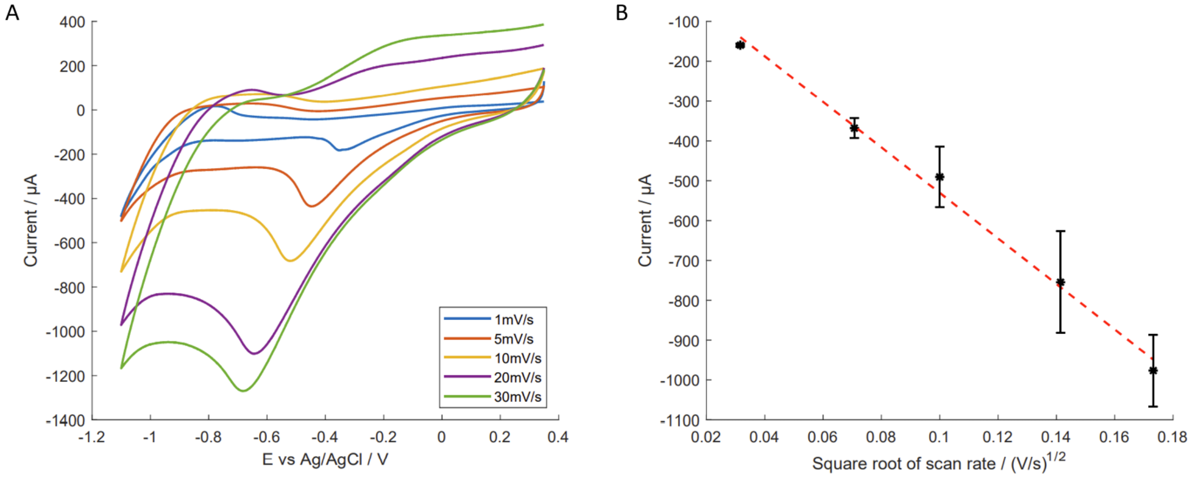

Figure 2.20 (A) Cyclic voltammetry of Pt/C electrode in air N2B27(–) under various scan rates (1 mV/s to 30 mV/s). (B) Plot of Pt/C electrode oxygen reduction peak current against square root of scan rate. Projected linear curve (red dotted line) is displayed on the image. The equation is $y = -4.89\times10^3x + 46.9$ ($R^2 = 0.9929$).

Faradaic current at the peak potentials were measured and plotted against the square root of scan rate (fig. 2.19B and fig 2.20B). A linear relationship was observed in the measured range (1mV/s to 30mV/s). This confirmed that oxygen reduction reaction in both electrolytes was diffusion controlled and determined by the Randles-Sevcik equation for an irreversible reaction. The electrochemical active surface area was calculated from the slope of the fitted curve. Taking the solvated molecular oxygen concentration in the electrolyte as 263µM, calculated from the Henry-Setschenow equation and for n = 4, $D_{O2} = 2.01\times10^{-5}$ $cm^2 s^{-1}$ and α = 0.11 (calculated and explained from the Tafel plot discussed below (fig. 2.21)), the calculated electrochemical active surface area was 5.97cm^2 and 5.19cm^2 for PBKCl and N2B27(–) respectively, more than three-fold of the geometric area (1.53cm^2).[102,122] This could be explained by the heterogeneous dispersal of platinum particles on the graphite and the irregular topography of the material observed in the SEM micrographs.

The kinetics of the oxygen reduction reaction in both electrolytes were investigated with the Tafel slope and the respective exchange current densities. Two fitted slopes could be fitted on the Tafel plots for each electrolyte (fig. 2.21). The projected Tafel slopes of PBKCl were 276 mV/Dec (yellow dotted line) and 514mV/Dec (purple dotted line) whereas in N2B27(–), the Tafel slopes were at 220mV/Dec (cyan dotted line) and 528mV/Dec (red dotted line). The two slopes, appearing to suggest a transition from one mechanism with slow kinetics to another, have been reported previously, attributed to the transition between different oxygen reduction processes leading to the formation of water or hydrogen peroxide.

The values were different from the commonly reported slopes at 60 mV/Dec and 120 mV/Dec of Pt/C catalysts in literature.[123,124] This difference was attributed to the decrease in Pt content in the material available for catalysing oxygen reduction reaction. Predominantly occurring with the inner-sphere electron transfer, direct adsorption of solvated O_2 was crucial for the oxygen reduction reaction. Low Pt content is expected to significantly minimize the formation of adsorbed Pt-O and Pt-O_2 and thus retard the catalytic conversion kinetics to H_2O.[121] The presence of two slopes suggested a change in rate determining step as suggested in literature: at low potentials, the dissociate mechanism leads to:

$$Pt + \frac{1}{2}O_2 \rightarrow PtO$$

$$PtO + H^+ + e^- \rightarrow Pt - OH$$

$$Pt - OH + H^+ + e^- \rightarrow H_2O + Pt$$

O_2 is adsorbed on platinum breaking the O-O bond (Pt-O); it is reduced and H_2O is produced. For this mechanism, the platinum surface is reduced platinum whereas at high potentials, the oxygen is adsorbed as molecular oxygen (Pt_2O_2) and a mixture of Pt and PtO exists. This mechanism can lead to H_2O_2. It has been reported that Pt/PtO changes the rate determining step from the first electron transfer to a pseudo-two electron transfer, respectively. This is evident from the low potential Tafel slope which was about two-fold the high potential Tafel slope. By using equation 2.14 and assuming the rate determining steps were first electron transfer and two electron transfer at low potential and high potential respectively, the transfer coefficient (α) was calculated to be 0.1 (Table 2.2). The equilibrium potentials were 0.32V and 0.18V (vs Ag/AgCl) in PBKCl and N2B27(–), respectively. The exchange current densities were very similar in both cases, calculated to be –5.90 and –5.34 in PBKCl, and –6.11 and –5.40 in N2B27(–). It was interesting that dihydrogen phosphate ($H_2PO_4^-$) ions were reported in literature, particularly in high temperature fuel cell applications, to affect the oxygen reduction reaction through competitive binding at the platinum reaction sites.[125,126] However, there is no evidence of this from the Tafel plots when comparing the phosphate buffered PBKCl against the carbonate buffered N2B27(–). The presence of protein and amino acids in the culture medium however, may have an equally strong effect in reducing the current density due to surface fouling.[127,128] By equation 2.12 and 2.13, the electrochemical reversibility parameter (Λ) was calculated as -5.25×10^{-2} and -3.29×10^{-2} in PBKCl and N2B27(–) respectively, fitting the criteria of an electrochemical quasi-reversible reaction ($15 \geq \Lambda \geq 10^{-2(1+\alpha)}$).

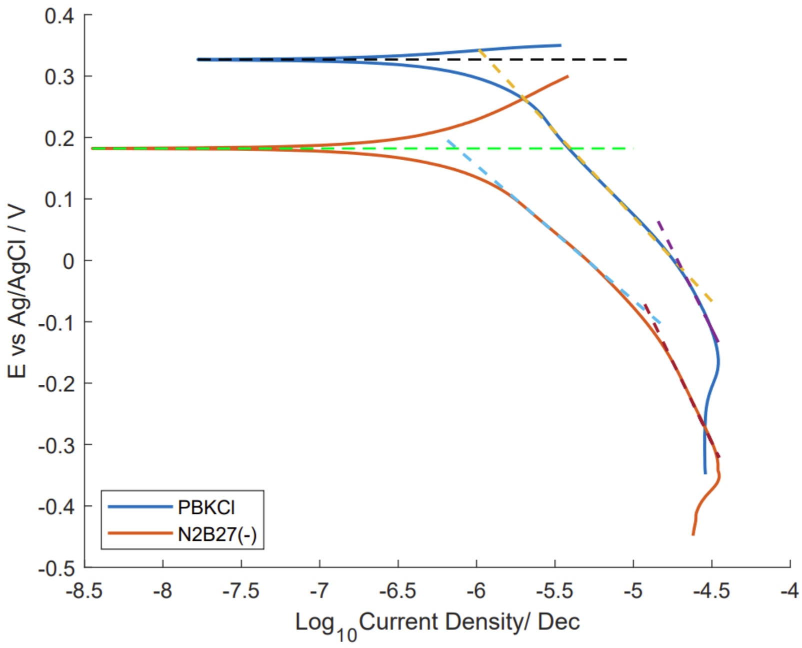

Figure 2.21 Tafel plot of Pt/C in PBKCl (blue) and N2B27(–) (orange) (scan rate: 1mV/s). In PBKCl, equilibrium potential was 0.32V vs Ag/AgCl and the Tafel slopes are 276 mV/Dec (yellow dotted line) and 514 mV/Dec (purple dotted line) whereas in N2B27(–), equilibrium potential was 0.18V vs Ag/AgCl and the Tafel slopes are 220 mV/Dec (cyan dotted line) and 528 mV/Dec (red dotted line). The equilibrium potentials were 0.32V (black dotted line) and 0.18V (green dotted line), and the respective exchange current densities were –1.18e–6 A/cm^2 and –0.74e–6 A/cm2 in PBKCl and N2B27(–).

Electrolyte	**Tafel slope (mV/Dec)**	**n*α**	**α**	**Exchange current density** $(\log_{10}(i_0))$
PBKCl	277 ± 14	0.21	0.11*	–5.90
	601 ± 51	0.10	$0.12^{\#}$	–5.34
N2B27(–)	232 ± 10	0.25	0.13*	–6.11
	492 ± 37	0.12	$0.12^{\#}$	–5.40

Table 2.2 Tafel slopes and the calculated transfer coefficient of the oxygen reduction reaction on Pt/C in different electrolytes. *: First electron transfer as rate determining step; $^{\#}$: pseudo-two electron transfer as rate determining step.

Chronoamperometry was conducted to determine the step potential of Pt/C for oxygen scavenging. To create maximum oxygen scavenging efficiency, the polarizing potential should be stepped to diffusion-controlled regime. According to the CV reported earlier, the peaks of oxygen reduction reaction in N2B27(–) were observed at –0.4V and –0.7V in 1mV/s and 30mV/s respectively. Step potentials of –0.6V, –0.7V and –0.8V were investigated to study diffusion-controlled oxygen reduction reaction in both air and degassed electrolyte (fig. 2.22). It was observed that in air all potentials showed very similar steady state current. However, current measured in nitrogen showed slight variations between different step potentials. While –0.6V and –0.7V had similar steady state current at –3μA and –7μA respectively, polarizing at –0.8V caused –20μA background current. This was evident by the CV in figure 2.20A that hydrogen evolution reaction become kinetically favourable at this potential. It was thus determined that the electrode was polarized at –0.7V (vs Ag/AgCl) for all subsequent oxygen scavenging experiments. The slight increase in current recorded in the first 50 seconds of polarizing at –0.6V was possibly due to wetting of the electrode and residual oxygen adsorbed on the surface of the Pt/C electrode, even though the electrode was pre-treated for 5 minutes at –0.7V.

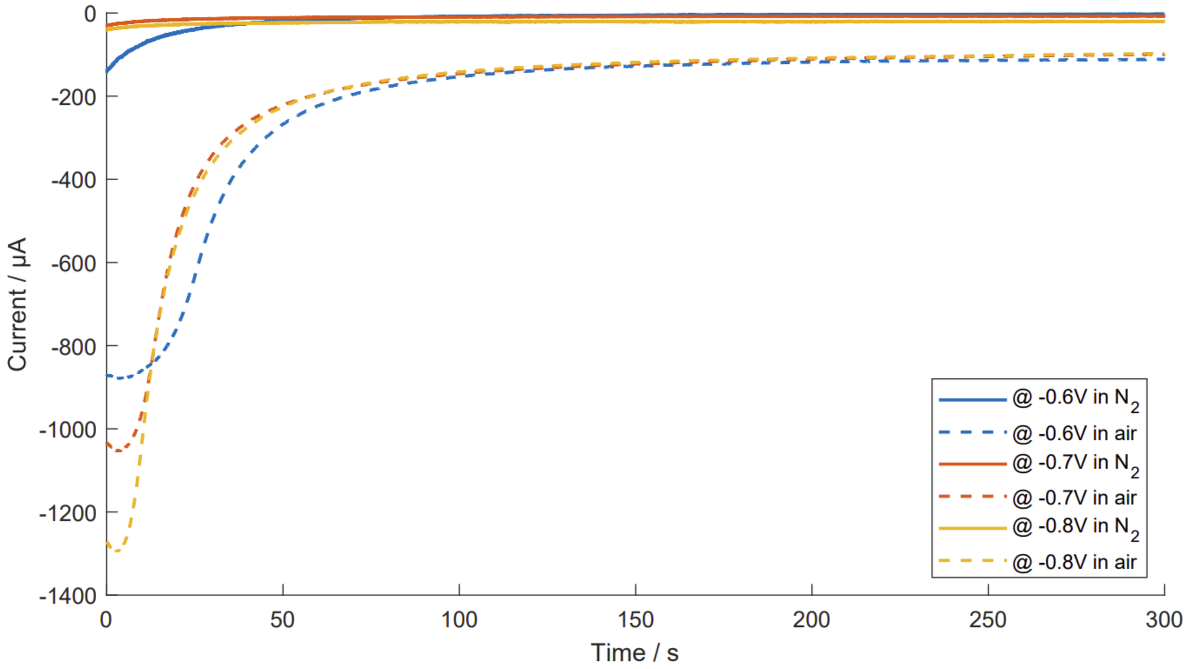

Figure 2.22 Chronoamperometry of Pt/C at different step potential in air (dotted line) and in degassed (solid line) N2B27(–). Blue: polarization at –0.6V; Orange: polarization at –0.7V; Yellow: polarization at –0.8V. A slight increase in current of polarization at –0.6V might be due to residual oxygen adsorbed on the surface of the Pt/C electrode or gas trapped in the material and Gore.

III. I. III. Surface Analysis

III. I. III. I. Pt/C regional analysis

Since it was observed in the SEM micrographs that the centre and the ring of the electrode had different topography, it is of interest to investigate their electrochemical behaviour. Similar to the observations reported earlier, CVs of both regions expectedly showed catalytic activity to the oxygen reduction reaction and increased peak potential when the scan rate was increased (figure 2.23A and figure 2.24A). Faradaic current density (from geometric surface area) was plotted against the square root of scan rate (figure 2.23B and figure 2.24B), with slopes –65.9 and –102.0 for the centre and the ring, respectively. The difference in slopes suggested that the geometric current density at the ring is higher than that of the at the centre of the electrode, which is consistent with the earlier discussion concerning the variation in electrode thickness and high PTFE content in the centre, as observed in the SEM micrographs (fig. 2.17).

Tafel plots of both regions showed some differences amidst the similarities (Figure 2.25). Both regions had the same equilibrium potentials at 0.32V. Although the Tafel slopes calculated showed some variation between electrodes, the two Tafel slopes observed for each part of the same electrode were nearly the same, calculated for example for the electrode examined as ~190mV/Dec and ~620mV/Dec at high and low potential respectively. While the change of rate determining step at lower potential was suggested as discussed previously, the Tafel slopes should not be directly compared with different electrodes due to differences in calculating surface areas. As indicated above, the differences between the two regions within the same electrode, lay in the geometric exchange current densities. On both parts of the electrode, the exchange current densities of the rim were larger than that of the centre (Table 2.3) but were similar at high and low potentials (circa 0.32A/mm^2). The small graphite granules at the ring drastically increased the surface area for electrochemical reactions. Yet, this topological difference should not cause any significant complications to the planar diffusion commonly observed on macroelectrodes, and thus the electrochemical system. Since oxygen diffuses in from the proximity of the ring and the base of the electrochemical cell is not oxygen permeable, a significantly higher oxygen concentration at the centre should not be expected.

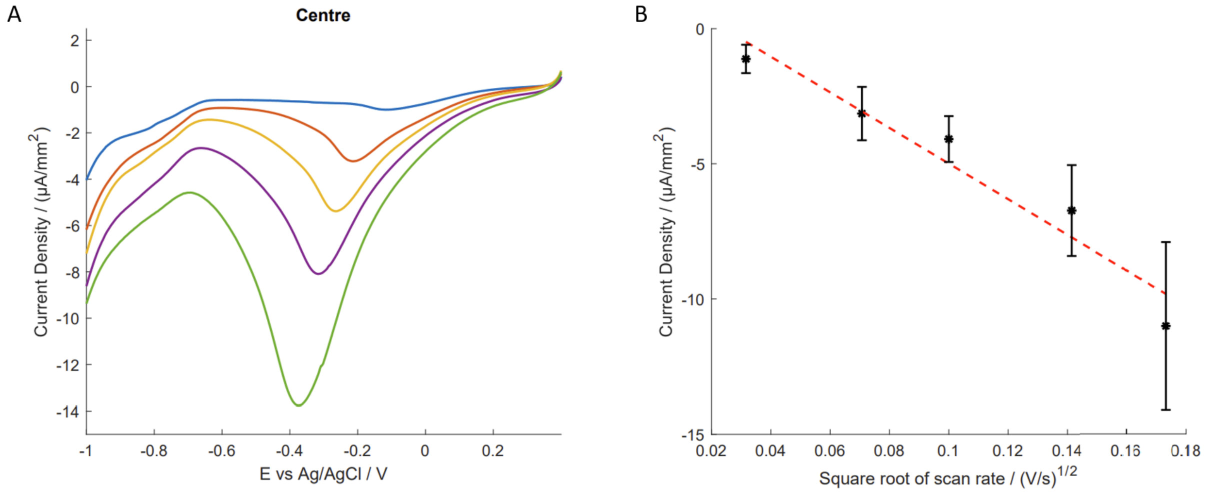

Figure 2.23 (A) Cyclic voltammetry of centre of Pt/C electrode in air PBKCl under various scan rates (1 mV/s to 30 mV/s). Current density was calculated by dividing against geometric surface area. (B) Plot of the oxygen reduction peak current density against the square root of scan rate. Three electrodes were used for the analysis. Projected linear curve (red dotted line) is displayed on the image. The equation is $y = -65.9x + 1.6$.

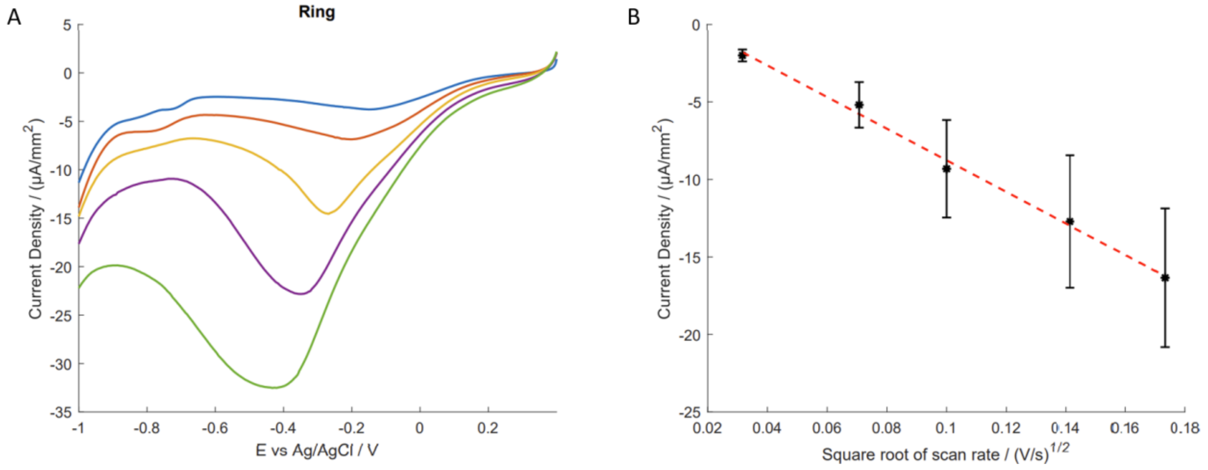

Figure 2.24 (A) Cyclic voltammetry of ring of Pt/C electrode in air PBKCl under various scan rates (1 mV/s to 30 mV/s). Current density was calculated by dividing against geometric surface area. (B) Plot of the oxygen reduction peak current density against the square root of scan rate. Three electrodes were used for the analysis. Projected linear curve (red dotted line) is displayed on the image. The equation is $y = -102.0x + 1.4$.

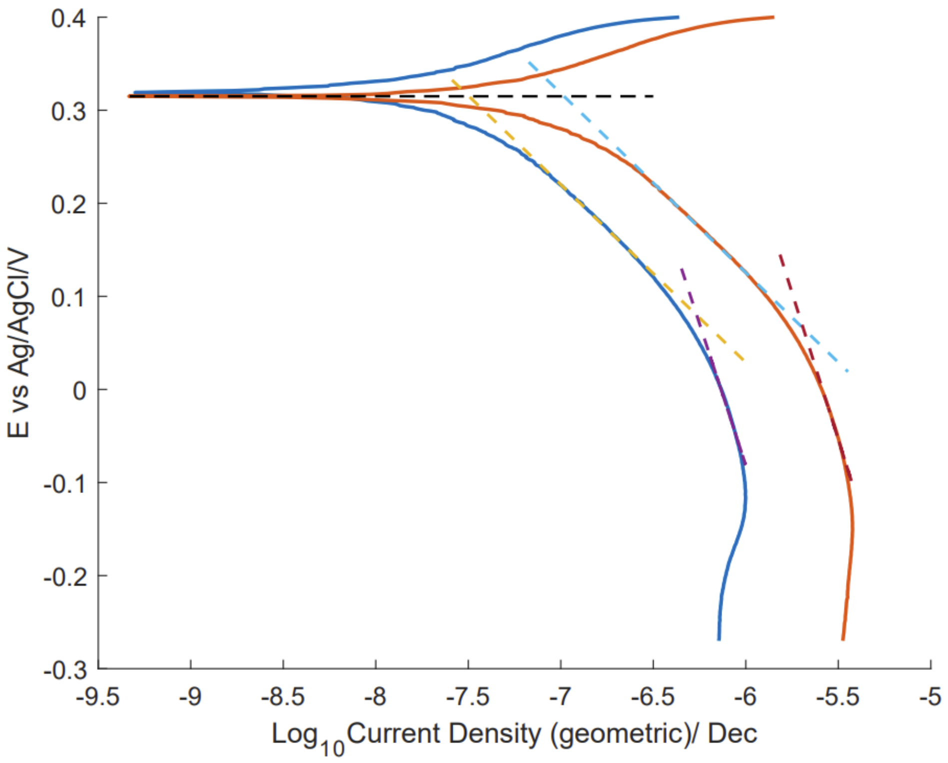

Figure 2.25 Tafel plot of the centre (blue) and the ring (orange) of Pt/C in PBKCl (scan rate: 1mV/s). The equilibrium potentials were 0.32V (black dotted line) for both regions. The Tafel slopes of the centre are 191 mV/Dec (yellow dotted line) and 608 mV/Dec (purple dotted line) whereas those at the ring are 193 mV/Dec (cyan dotted line) and 630 mV/Dec (red dotted line).

Region	**Tafel Slope (mV/Dec)**	**Exchange current density ($\log_{10}(i_0)$) (Geometric)**
Centre	191	–7.49
	608	–6.65
Ring	193	–6.98
	630	–6.09

Table 2.3 Tafel slopes and the exchange current density (geometric) of the oxygen reduction reaction on different regions of Pt/C in PBKCl. Note that the current density reported here were calculated from geometric surface area and should not be directly compared with the numbers reported earlier. Three electrodes were used for each region.

III. I. III. II. BET Surface Area

To investigate the increase of surface area and other surface properties that can affect diffusion, gas adsorption and electrochemical behaviour, Pt/C was further investigated by the Brunauer-Emmett-Teller (BET) surface area analysis. The nitrogen adsorption and desorption isotherm were plotted in figure 2.26. The plot suggested that a type II adsorption isotherm occurred on the Pt/C. As the partial pressure increases, a change in gradient was first observed at partial pressure 0.05 which was related to the completion of monolayer coverage and transition to multilayer adsorption. The sharp increase in slope observed at relative pressure 0.9 suggested capillary condensation. Unsupported platinum has been reported to have 5.2-11.5 m^2/g.[129] This 5% Pt/C electrode had a BET surface area of 52.9 ± 14.0 m^2/g (mean ± S.E.M.) (n=2). The surface area was significantly larger than both mesoporous Pt and nanostructure Pt film at about 37 m^2/g.[129,130] The pore radius and pore volume were 15.48 ± 0.06 Å and 0.079 ± 0.008 cm^3/g respectively. These data suggested that the Pt/C electrode has a large non-porous surface with micropores allowing an advantageous increase in reactive sites for oxygen reduction reaction, without reducing the available potential window for oxygen reduction and introducing the problem of the hydrolysis of water. This observation echoed the large electrochemical active surface area calculated, compared with its geometric surface area.

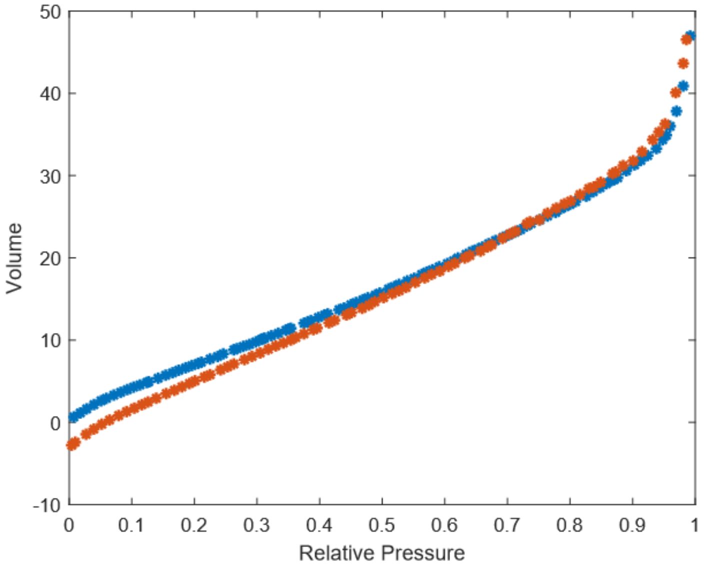

Figure 2.26 BET curve of 5% platinum / carbon. Adsorption curve (blue); desorption curve (red).

III. I. IV. Oxygen adsorption on carbon supported electrodes

Oxygen adsorption is a typical feature observed in graphite containing materials.[131] Pt/C electrodes demonstrated the same property, as expected for their high graphite content and exposure to air for extensive periods. Observed from figure 2.27A and figure 2.28A, chronoamperometries showed major decrease in current due to reduction of oxygen adsorbed on Pt/C after the first 200 sec of stepwise polarization at –0.7V vs Ag/AgCl. Measured currents reached steady-state current after 200s regardless of the oxygen adsorption. These electrodes showed high background O_2 capacity irrespective of the solution they were placed in. From the Anson plot measured in nitrogen (fig. 2.27B), the charge differences between the oxygen adsorbed and oxygen depleted electrode were projected and showed an intercept at 15.80 ± 2.77mC. By equation 2.12, O_2 adsorbed on the Pt/C surface amounted to 40.93 ± 7.18nmol. When the same measurement was conducted in air, the intercept of the charge differences was 30.98 ± 1.47mC. This increase in charge measured in air is related to gas trapped in the pores and Gore membrane in the electrode, which will be further analysed below. In contrast, oxygen depleted Pt/C electrodes had intercepts at 0.10mC and 0.01mC in air and nitrogen respectively. These values, assumed to be dependent on double layer charging, are at least 3 orders of magnitude lower than the charge generated from adsorbed oxygen, suggesting the high oxygen capacity of Pt/C.

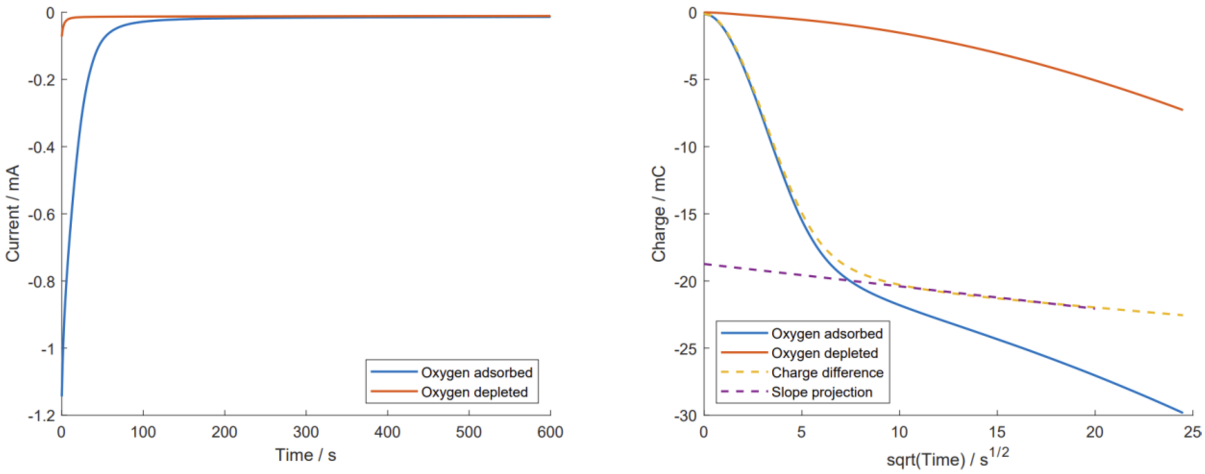

Figure 2.27 Chronoamperomogram (A) and Anson plot (B) of Pt/C at –0.7V vs Ag/AgCl in degassed PBKCl. Blue: oxygen adsorbed Pt/C electrode; Orange: oxygen depleted Pt/C electrode; Yellow: difference between oxygen adsorbed and oxygen depleted curves. Purple: slope projection.

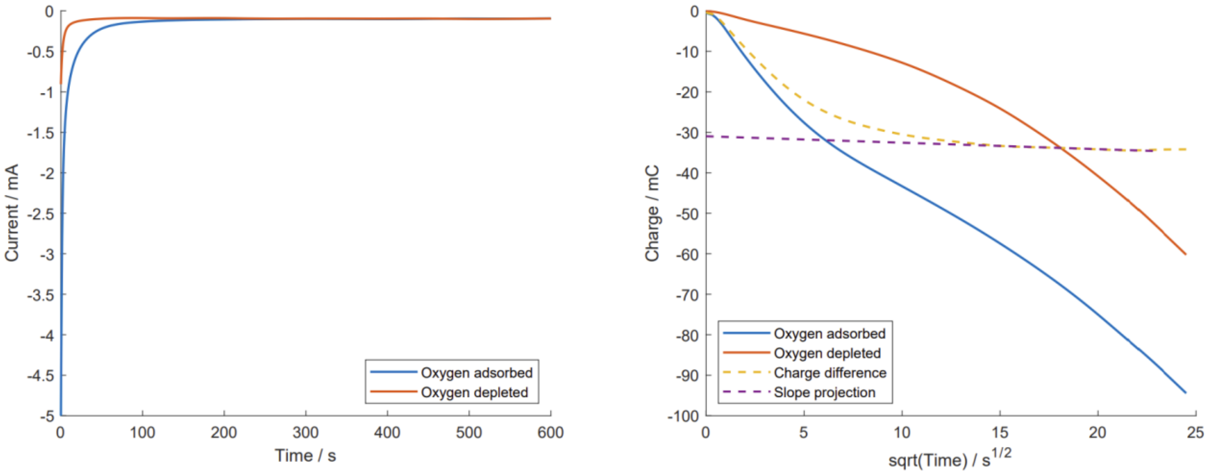

Figure 2.28 Chronoamperomogram (A) and Anson plot (B) of Pt/C at –0.7V vs Ag/AgCl in air PBKCl. Blue: oxygen adsorbed Pt/C electrode; Orange: oxygen depleted Pt/C electrode; Yellow: difference between oxygen adsorbed and oxygen depleted curves; Purple: slope projection.

PBKCl	**Charge adsorbed (mC)**	**O_2 adsorbed (nmol)**	**O2 trapped (nmol)**
Air	30.98 ± 1.47	-	39.35 ± 11.0*
Degassed	15.80 ± 2.77	40.93 ± 7.18	-

Table 2.4 Table of the charge adsorbed and the calculated oxygen adsorbed on the Pt/C electrode. Three electrodes were used for analysis in each condition. *: Assuming the oxygen adsorbed in the value measured in degassed PBKCl.

Interestingly, it is also observed that the measured charge depends on the ambient condition and the oxygen adsorption state of the electrode (fig. 2.29). Negative charge from Faradaic current passing through the oxygen depleted electrodes expectedly rose steadily after subtracting the background capacitance charging (measured in degassed electrolyte) at a rate of –82.9mC/s. On the oxygen adsorbed electrodes, a significant rise in negative charge at a rate of –84.6mC/s was recorded in the first 100 seconds before reaching the steady state.

15.19 ± 4.25mC decrease in Faradaic charge was measured in air compared with that measured in degassed electrolyte during the first 100 seconds (n = 3). When the electrode was submerged into the electrolyte, gas was trapped in the pores of the material and in the hydrophobic Gore membrane. This created a fast-diffusing source of oxygen for the oxygen reduction reaction at the three-phase boundary (material-gas-electrolyte) until depleted, illustrated by the schematic diagram in figure 2.30. This phenomenon could exist in air but not in degassed conditions where oxygen in the void diffused out before the experiments were conducted. Such observation was also absent in the charge depleted electrode in air as charge measurements (oxygen scavenging) were conducted immediately after the measurement of the oxygen adsorbed electrode.

As a result, assuming that all charges were accounted for by oxygen undergoing 4-electron reduction reaction, a total of 39.35nmol of oxygen were trapped in the electrode. While the compressibility factor of gas in air at 300K and 1bar is 0.9999, it could be assumed that the gas behaved as an ideal gas.[132] By the ideal gas law, the total amount of gas (39.35nmol) in the electrode occupied 0.97mm^3, which calculated the total volume of void in the material and the Gore membrane.

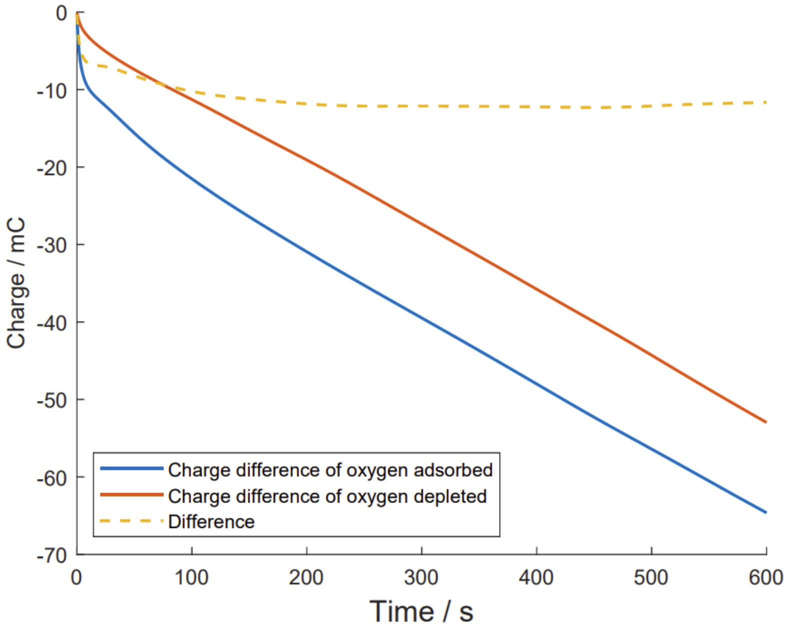

Figure. 2.29 Charge differences under different ambient conditions with oxygen adsorbed (blue) and oxygen depleted electrode (red). The difference between the two curves showed gas trapped in the electrode (yellow dotted line). Steady state equation of oxygen adsorbed is $y = -82.9x - 2.75\times10^3$ whereas oxygen depleted is $y = -84.6x - 14.09\times10^3$.

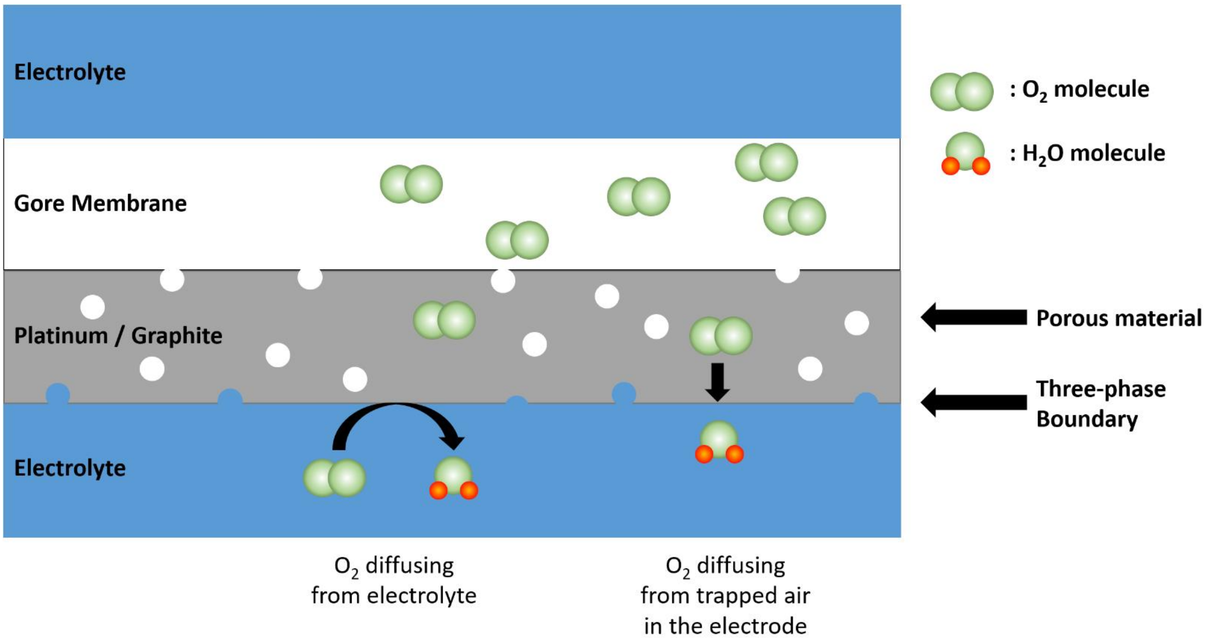

Figure 2.30 Schematic presentation of the gas diffusion towards the three-phase boundary in the Pt/C electrode.

This concludes that oxygen adsorption is expectedly occurring on the Pt/C electrode. Removal of adsorbed oxygen by electrochemical reduction is efficient. If the oxygen scavenging is required within minutes, pre-removal of adsorbed oxygen should be performed by polarizing the Pt/C electrode at a cathodic potential for 3 minutes for more reproducible oxygen scavenging.

III. II. Oxygen scavenging by Pt/C electrode

III. II. I. Characterization of Clark electrode

As also seen in the previous section, oxygen reduction reaction peak(s) were observed in the CV (fig. 2.27 and fig. 2.29). In PBKCl, two reduction peaks were observed, as expected, at –0.4V and –0.7V (vs Ag/AgCl) in the aerated electrolyte but absent in the N_2 conditioned electrolyte (fig. 2.31). The peaks were associated to the reduction of the oxygen. The hydrogen evolution peak was observed from –0.9V that provided a good window for detecting dissolved oxygen in the electrolyte at less cathodic potentials. However, in PBS, only one oxygen reduction peak was observed at –0.7V (fig. 2.33). Chronoamperometry was conducted in PBKCl and PBS at –0.5V and –0.7V, respectively. The steady-state current after 120s of polarization (n = 3) were recorded and plotted as the calibration curves (fig. 2.32 and fig. 2.34). The respective linear fits of the curves were calculated as:

$$I = -1.24 \times 10^{-3} \times [O_2] - 1.66 \times 10^{-3} \tag{2.22}$$

$$I = -1.93 \times 10^{-3} \times [O_2] - 2.42 \times 10^{-3} \tag{2.23}$$

These calibration curves were used for predicting the spatiotemporal change of oxygen concentration resulted from electrochemical oxygen scavenging.

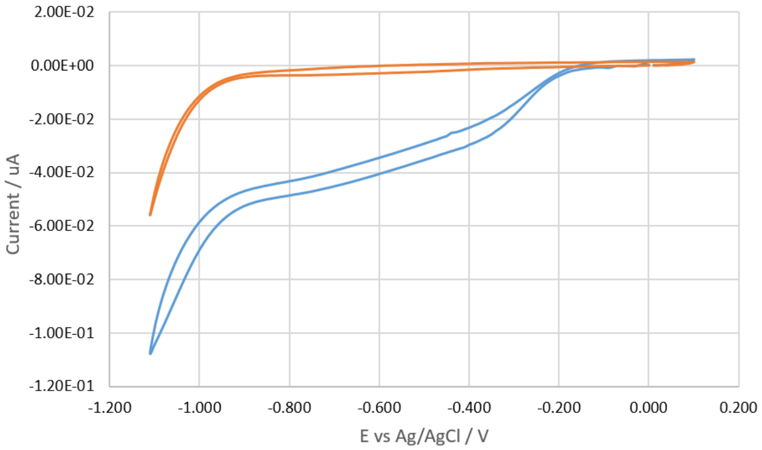

Figure 2.31 Cyclic voltammetry of the Clark electrode (Ø: 125µm) used at the centre of the base of the culture well in PBKCl (pH 7.4) at 50 mV/s. Blue (air); Orange (degassed).

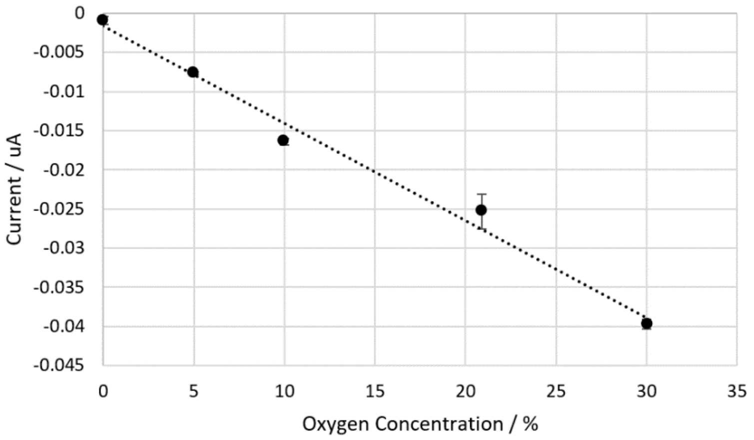

Figure 2.32 Calibration curve of Clark electrode (–0.5 V vs Ag/AgCl) in PBKCl (pH 7.4). Mean ± S.D. Linear fit (dotted line) is $y = -1.24 \times 10^{-3}\, x - 1.66 \times 10^{-3}$.

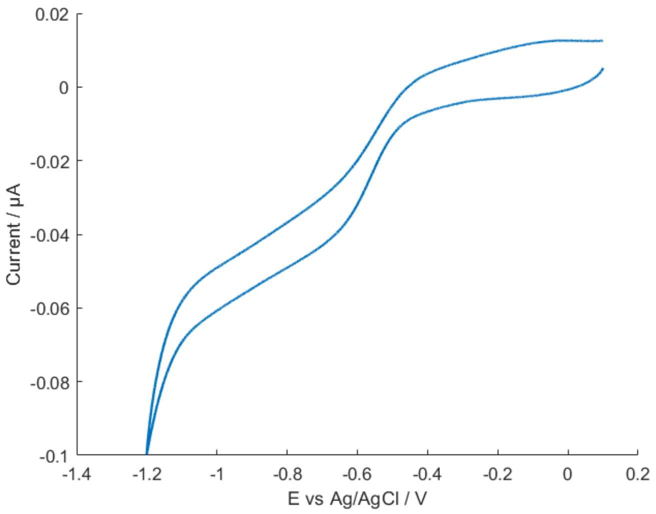

Figure 2.33 Cyclic voltammetry of the Clark array electrode 8 (Ø: 125µm) (at the centre of the base of the culture well) in PBS (pH 7.4) in air at 50 mV/s.

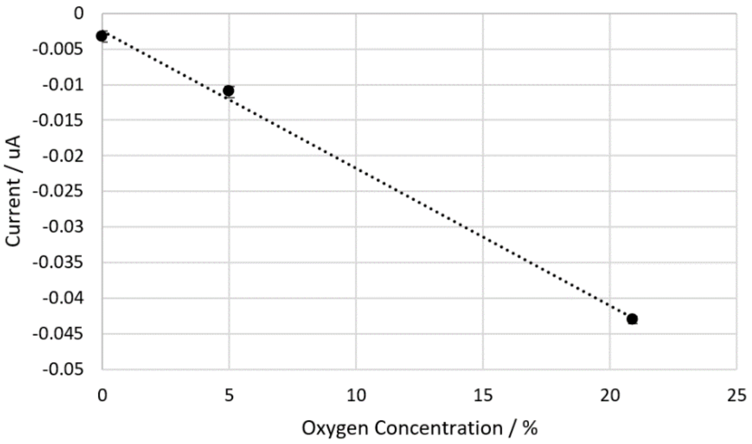

Figure 2.34 Calibration curve of Clark electrode (@ – 0.7 V vs Ag/AgCl) in PBS. Mean ± S.D. Linear fit (dotted line) is $y = -1.93 \times 10^{-3}x - 2.42 \times 10^{-3}$.

III. II. II. Oxygen equilibration in incubator

The Clark electrode was used to measure the oxygen equilibration occurring in the incubator. Oxygen concentration measured showed a decrease in concentration in the electrolyte over time and eventually reaching steady state, with equilibration with the ambient 5% O_2 set by the low oxygen incubator (fig. 2.35). It was also noted that after removing non-Faradaic current in the first 50 seconds, initial oxygen concentration measured was at 14%, below the external ambient air concentration of 20.9%. This may be due to the brief delay for setting up the device in the incubator allowing early gas exchange from 21% O_2 before measurements began. The average time required for full equilibration was 3.3 ± 0.8h (mean ± S.E.M., n = 3). The duration recorded here is comparable to the time needed to equilibrate from 21% O_2 to 0% reported in literature and will be limited by exchange at the electrolyte-air interface area and dependent on the volume height of electrolyte used here (7.5mm) compared with that in the literature (2.5mm). Still, dependence on diffusion-based equilibration for creating low oxygen environment in cell models is unsuitable for studying acute hypoxia. A more robust, controllable and efficient oxygen removal is required.

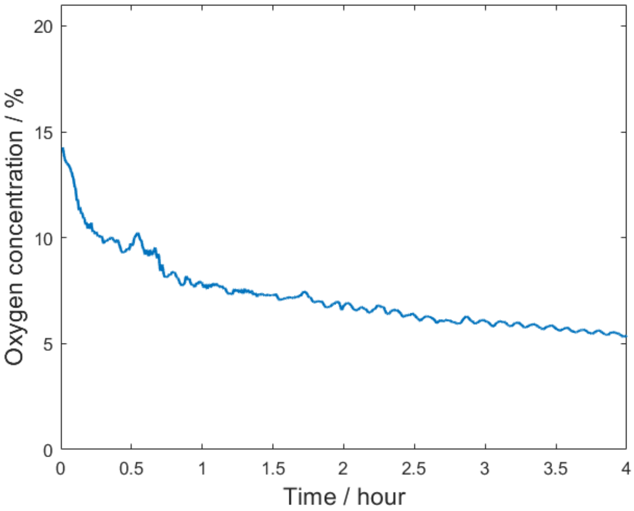

Figure 2.35 Oxygen concentration change under equilibration in incubator. Oxygen concentration setpoint was at 5.0% O_2.

III. II. III. Electrochemical cell design and oxygen scavenging

To create a translatable hypoxia device for generating oxygen gradients, an electrochemical system was constructed. The electrochemical cells were constructed in a polystyrene petri dish (Ø: 55 mm). Three wells were created in the system to facilitate future experiments which require one negative control, one positive control and one electrochemical cell for hypoxic stress induction. The wells were designed as 17mm in diameter, similar to that in a 24-well plate to facilitate the use of glass coverslips of 12mm diameter. PDMS was chosen as the material due to the oxygen diffusion in PDMS being two orders of magnitude larger than in polystyrene ($D_{O2,\ PDMS} = 3.25 \times 10^{-9}\ m^2/s$;

$D_{O2, PS} = 0.011 \times 10^{-9}$ m^2/s), allowing lateral oxygen diffusion for generating oxygen gradients in the culturing wells.[133]

It was investigated whether Pt/C could generate a spatiotemporal change of oxygen concentration at the base of the electrochemical cell where adherent cells would be cultured. The Clark electrode array was thus positioned at the base to record the residual oxygen concentration under oxygen scavenging under different conditions (see fig. 2.16).

III. II. III. I. Effective oxygen scavenging in low and normal ambient oxygen level

The effectiveness of oxygen scavenging was investigated in both normal and reduced ambient oxygen concentration (fig. 2.36). The reduced ambient oxygen level investigated was 38mmHg (5%) O_2 which is the physiological oxygen concentration and is commonly used in cell cultures. Oxygen concentration measured on the Clark electrode in the centre, at the base of the cell, decreased upon Pt/C polarization and steady state was attained within 30 minutes. Notably, oxygen concentration halved in 5 minutes in both cases and tailed off to 0mmHg (0%) O_2 at 22 minutes and 27 minutes from 38mmHg (5%) and 159mmHg (20.9%) O_2, respectively. This provided promising evidence of effective oxygen scavenging, irrespective of the ambient oxygen level. In addition, time required to equilibrate oxygen concentration from 159mmHg (20.9%) to 38mmHg (5%) O_2 was significantly reduced to 7 minutes with the oxygen scavenging electrode at 1 mm height, compared with circa 3 hours required by a conventional low oxygen incubator, as was evident by the experiment reported previously (section III.II.II.). Electrochemical oxygen scavenging effectively reduced the time needed by 96%, demonstrating the potential superiority of electrochemical oxygen scavenging to diffusion-based concentration change.

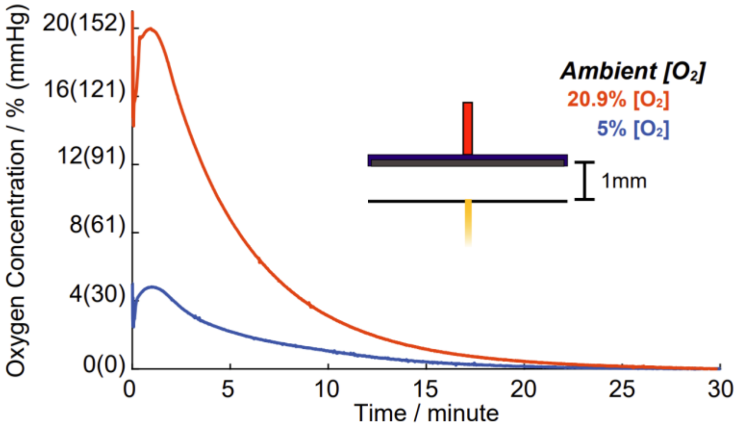

Figure 2.36 The Clark electrode (–0.5V vs Ag/AgCl) positioned at the centre of the electrochemical cell measured the resultant oxygen concentration under Pt/C polarization (–0.7V vs Ag/AgCl) in air and 5% O_2. Current measurement at first 2 minutes were due to current limiting caused by non-Faradaic current of Pt/C polarization.

III. II. III. II. Controlled steady state oxygen concentration

Reduction of local oxygen concentration was observed by positioning the Pt/C electrode at different heights (fig. 2.37). All heights tested resulted in an exponential decrease of oxygen concentration upon Pt/C polarization and reached the steady state after 30 minutes, measured at the centre of the electrochemical cell. The steady state oxygen concentration was expectedly dependent on the position of the Pt/C electrode, giving 0% (0 mmHg), 1.7% (14 mmHg) and 7% (53 mmHg) from 1, 2 and 3mm in height, respectively. Oxygen diffusing from the perimeter and bulk solution, beyond the oxygen depletion zone to the point of measurement were accountable for the difference in steady state oxygen concentration.

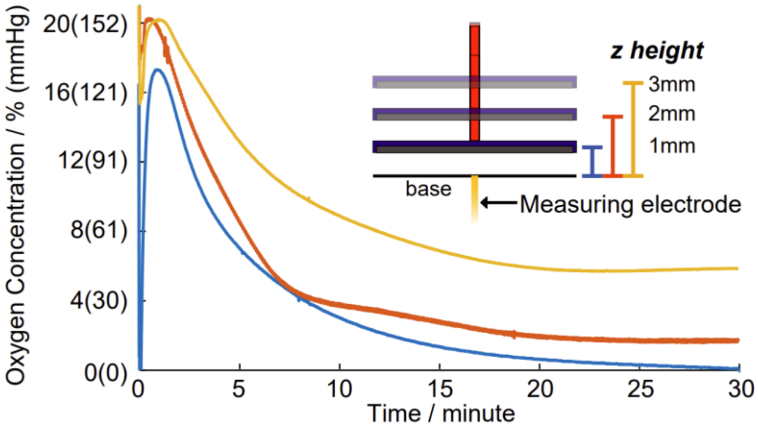

Figure 2.37 Oxygen concentration measured by Clark electrode (–0.5V vs Ag/AgCl) at the centre of the electrochemical cell. The height of the Pt/C electrode was varied from 1mm (blue) to 2mm (orange) to 3mm (yellow). Pt/C polarized at –0.7V vs Ag/AgCl for 30 minutes. Current measurement at first 2 minutes were due to current limiting caused by non-Faradaic current of Pt/C polarization.

Electrode height positioned	$[O_2]$ steady state
1mm	0mmHg (0%)
2mm	14mmHg (1.7%)
3mm	53mmHg (7.0%)

Table 2.5 Table of steady state oxygen concentrations at the centre of the base under different scavenging electrode heights in air ($[O_2]$: 159mmHg/20.9%).

III. II. III. III. Radial oxygen gradient

Similarly, an oxygen concentration gradient was evident across the base of the electrochemical cell under the scavenging electrode (fig. 2.38). Oxygen concentration increased radially when the scavenging electrode was kept constant at 2mm in height. The steady state oxygen concentrations were 1.7% (13mmHg), 2.2% (17mmHg) and 5.0% (38mmHg) at 0mm, 2mm and 6mm radial distances from the centre, respectively. The increase in oxygen concentration was accounted for by the oxygen diffusing from the solution and through the PDMS-electrolyte interface.

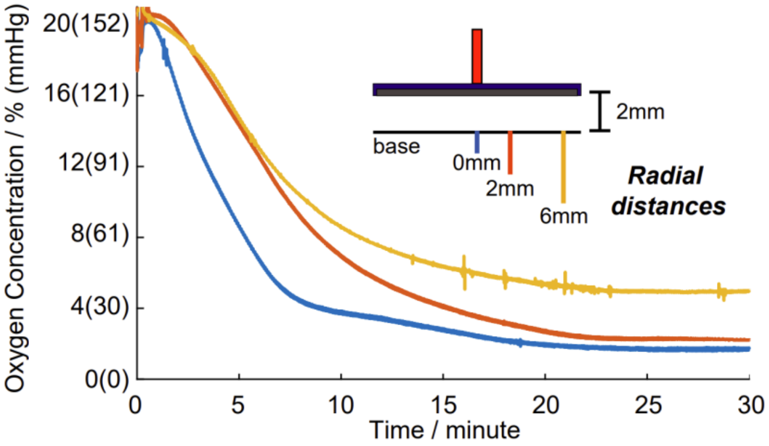

Figure 2.38 Clark electrode (–0.5V vs Ag/AgCl) was used to measure resultant oxygen concentration under Pt/C polarization (–0.7V vs Ag/AgCl). The position of the Clark electrode was at radial distances 0mm (blue), 2mm (orange) and 6mm (yellow). Current measurement at first 2 minutes were due to current limiting caused by non-Faradaic current of Pt/C polarization.

Radial distances	**[O_2] steady state**
0mm	13mmHg (1.7%)
2mm	17mmHg (2.2%)
6mm	38mmHg (5.0%)

Table 2.6 Table of steady state oxygen concentrations at various radial distances under scavenging electrode height at 2mm in air ([O_2]: 159mmHg/20.9%).

III. II. III. IV. Oxygen gradient within the electrochemical cell

To investigate if an oxygen gradient could be generated in the culture by changing the electrode size, the Pt/C electrode was cut into half (half circle of 8mm radius) and positioned at 2 or 3mm above the base of the right-half of the electrochemical cell (fig. 2.39). Based on the fact that the oxygen diffusion coefficient in PDMS is two orders of magnitude higher than that of PS, PDMS chosen over PS can facilitate diffusion across the walls to generate focal hypoxia instead of a no flux bulk hypoxia in conventional 24-well PS plates. After 30 minutes of oxygen scavenging in air, oxygen concentration reached steady state and Clark electrodes in the array were sequentially selected in random order for measuring the residual oxygen concentration until all positions were measured (fig. 2.40). The oxygen concentrations measured by each electrode were plotted in figure

2.41. An oxygen gradient was observed to correlate with the position of the electrode (shaded region). The biggest oxygen decrement was observed from Clark electrode 1 to Clark electrode 6 (–7.5 mm to –2.5mm radial distances), creating an oxygen gradient from ambient concentration to c.a. 60 mmHg (8%) O_2 respectively in both heights. This gradient was predictably a result of oxygen diffusing into the oxygen depleted zone underneath the scavenging electrode. Expectedly, the oxygen concentration underneath the scavenging electrode was the lowest within the measurements. At 3mm, oxygen concentration remained low and steady at circa 60 mmHg (8%) O_2 from –2.5mm till 4.5mm radial distance. At 2mm, the oxygen concentration decreased from –2.5mm and reached the lowest concentrations between 1.5mm to 4.5mm radial distances from the centre. The lowest oxygen concentration measured was 27mmHg (3.5%) O_2 at 3.5cm, which coincides with the centre of the electrode. The relatively similar oxygen concentration measured under the scavenging electrode was anticipated by the planar diffusion model commonly used for macro-electrodes. For the scavenger electrode at both heights, an increase in oxygen concentration was observed at the outer edge, from 4.5cm to 7.5cm. This is expected due to the oxygen diffusing from the PDMS into the electrolyte.

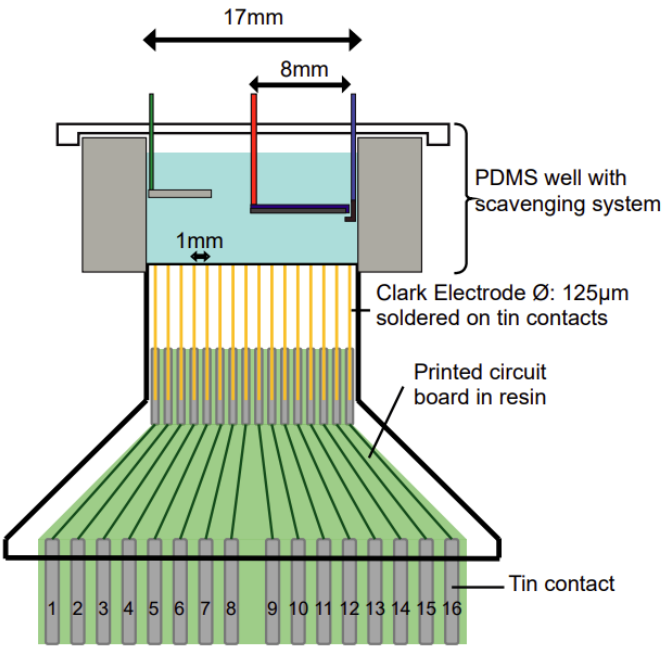

Figure 2.39 Schematic diagram of Clark electrode array assembled with the PDMS well and oxygen scavenging system. Clark electrodes are 1mm apart from each other, evenly distributed across the Ø:17mm base of the electrochemical cell.

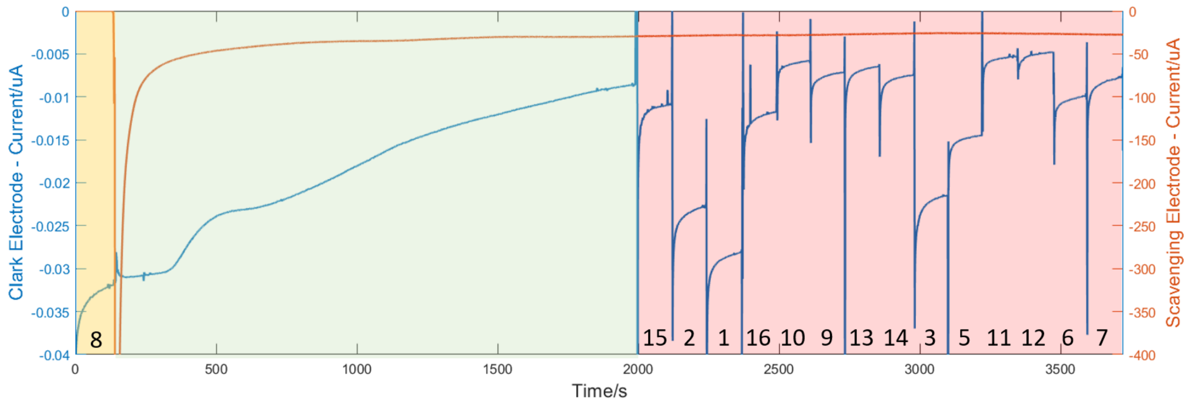

Figure 2.40 Oxygen measurement by Clark electrode (blue curve) under half circle Pt/C electrode oxygen scavenging at 2mm height. Clark electrode 8 was polarized first for 120 seconds (Yellow zone). Pt/C electrode was polarized at t=120s and steady state is reached after 30 minutes of scavenging (Green zone). The Clark electrodes were randomly measured for 120s each, in a sequence of 15-2-1-16-10-9-13-14-3-5-11-12-6-7 (Electrode 4 was faulty and omitted from all measurements) (Red zone). Electrodes 1-8 are positioned in the control half while electrodes 9-16 were in the hypoxia half. The orange curve is the current measured by Pt/C scavenging electrode. Spikes in current observed were due to artefacts caused by electrode clipping.

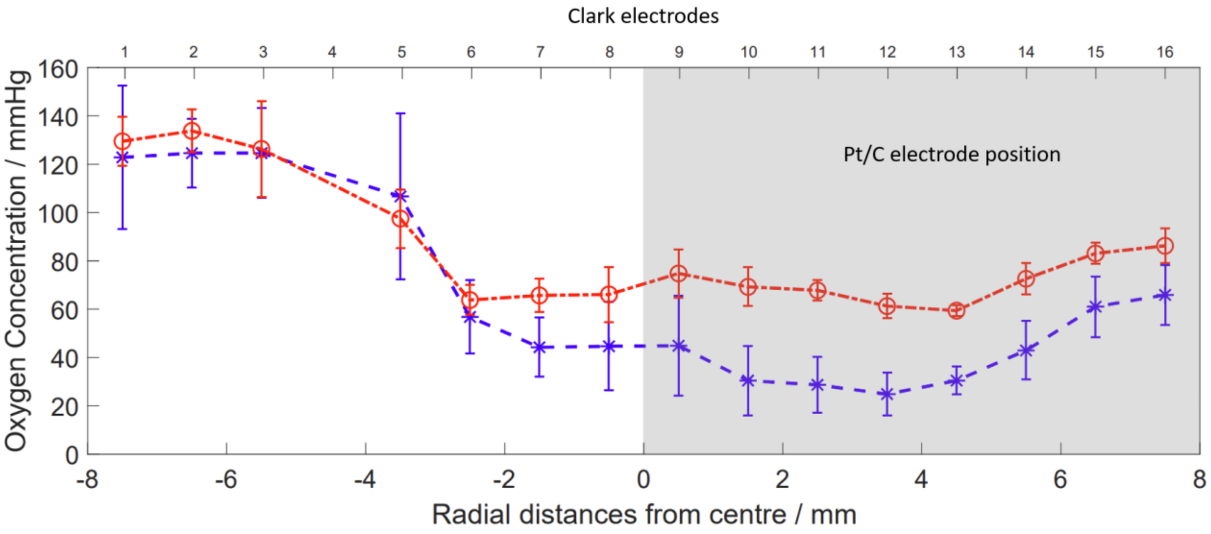

Figure 2.41 Oxygen measurement (mean ± S.E.M.) across the base of the well at 2mm (blue) and 3mm (red). Radial distances are presented at bottom x axis where position under the electrode were denoted as the positive. Top x axis denotes the relative positions of the numbered Clark electrodes, schematically presented in figure 2.35.

IV. Conclusions

The key component for developing an electrochemical oxygen scavenging model is the choice of electrode material for efficiently removing dissolved oxygen from the aqueous medium. Based on previous studies, 5% platinum / graphite (Pt/C) was identified as the ideal candidate of oxygen scavenging material.[93] Its high exchange current density and catalytic activity for the oxygen reduction reaction are highly beneficial to the application. Investigations reported in this chapter provided extended evidence of the promising properties of the material for the generation of low oxygen environment in a biocompatible electrolyte.

The oxygen scavenging electrode material was sintered on a semi-rigid Gore membrane that provides structural support, flexibility and oxygen permeability for efficient scavenging in all dimensions. The electrode can be formed or cut to different shapes and sizes, so a simple reshaping process can tailor the electrode for the purposes of cell cultures, but the specifications for oxygen scavenging in this environment, as clearly identified in this study, allow further electrode design to be achieved.

The electrochemical window of Pt/C was advantageous for oxygen reduction reaction to occur without hydrolysing water. The significant cathodic shift of the electrochemical window on Pt/C compared to Pt was probably due to the high amount of graphite in the material mixture and low platinum content. This causes an increase in surface energy required to adsorb hydrogen and thus a more cathodic potential was needed for hydrogen evolution. Polarization of the electrode for oxygen reduction reaction can be achieved to avoid reaching such potential.

Pt/C expectedly catalysed oxygen reduction reaction as evidenced by cyclic voltammetry performed in aerated electrolytes. The absence of a reverse anodic peak and cathodic peak shift, from –0.25V to –0.6V (vs Ag/AgCl) when scan rates were increased from 1mV/s to 30mV/s, demonstrated the chemical irreversibility of the reaction. The slow kinetics of the material was proven by the double Tafel slopes at 277 ± 14mV/Dec and 601 ± 51mV/Dec in PBKCl and 232 ± 10mV/Dec and 492 ± 37mV/Dec in N2B27(–), significantly slower than the theoretical values of Pt at 60mV/Dec and 120mV/Dec. The respective exchange current densities measured were –5.90 and –5.34 in PBKCl, and –6.11 and –5.40 in N2B27(–). This does not inhibit the use of the material for this application since a diffusion-controlled cathodic potential could be used to scavenge the dissolved oxygen in the solution.

Large surface area was an advantageous property of the material for increasing oxygen scavenging efficiency. The electrochemical active surface areas of Pt/C calculated from the Randles-Sevcik equation in PBKCl and N2B27(–) were 5.97 cm^2 and 5.19 cm^2 respectively, which are more than three-fold larger than the geometric surface area (1.53cm^2). It was further confirmed by the BET surface area at 52.9m^2/g, significantly larger than the literature values of mesoporous Pt and polycrystalline Pt. The irregular surface and high carbon content in the micropore material was accounted for the significant increase in surface area, proved by the SEM micrographs. Another property of carbon is the oxygen adsorption capacity. High oxygen adsorption on Pt/C was observed at 40.93nmol (15.80mC) O_2 measured in degassed electrolyte. In aerated electrolyte, the additional 15.19mC measured suggested efficient oxygen reduction reaction catalysed by Pt/C and gas trapped within the void of the electrode.

The electrochemical cell designed for oxygen scavenging was capable of creating an oxygen gradient environment with spatiotemporally advancements for cell culture. Oxygen concentration measured with the Clark electrode in the base of the culture cell proved that electrochemical removal of oxygen from ambient culture medium required only 7 minutes to reach 38mmHg (5%) O_2 as compared to circa 3 hours needed by low oxygen incubators. The remarkable improvements were further evident in oxygen depletion at physiological oxygen level (38mmHg / 5% O_2) to hypoxic level (11mmHg / 1.5% O_2 at which cells are reported to show 50% of their maximum hypoxia response[23]) in 6 minutes. In unconditioned medium (159mmHg / 20.9% O_2), 11mmHg (1.5%) and 4mmHg (0.5%) O_2 are reached in 13 minutes and 18 minutes, respectively.

The oxygen gradient over radial distances under the scavenging electrode can be adjusted both by the vertical height of the scavenger above the cells and by controlling the position and size of the scavenging electrode. Scavenging oxygen with a half electrode for 30 minutes showed steady-state oxygen concentrations at 25mmHg (3.5%) and 60mmHg (8%) O_2, plus an oxygen gradient over 4mm due to the high oxygen diffusion coefficient of PDMS.

In conclusion, Pt/C was an ideal material for oxygen scavenging in cell culture. Graphite alone has very slow kinetics for oxygen reduction whereas platinum has fast kinetics for oxygen reduction reaction but has low malleability and also catalyses hydrogen evolution at a lower overpotential. The mixture of two materials had the edge in increased surface area and widening the electrochemical window by having more cathodic potential of hydrogen evolution. Its significant reduction in cost is also beneficial for mass production and general use. These remarkable characteristics proved the degree of flexibility and efficiency of the oxygen scavenging system, in combination of Pt/C electrode and the electrochemical cell, for achieving a spatial and temporal controlled cell model for studying focal hypoxia.

Chapter 3: Electrochemical focal hypoxia in human *in vitro* cell model

I. Introduction

Animal models for cerebral hypoxia can be classified into two major types (1) using gas chambers and (2) performing surgeries.[4,134] Animals can be exposed to hypobaric chambers or normobaric hypoxia chambers to study diseases such as pulmonary hypertension, hypoxia/reperfusion injuries and hypoxic insults in the brain. Surgical hypoxia is commonly induced by electrocoagulation of the artery, occlusion and application of the vasoconstriction drug endothelin-1.[62] All these methods, apart from electrocoagulation, generate bulk cerebral hypoxia that can hardly be confined to the millimetre range. Electrocoagulation can create more focal occlusion, but it is permanent unless the part of the artery is replaced, or the obstruction is relieved. These methods usually incur surgical scars that can compromise and alter the hypoxia pathophysiology of the local tissue.

In vitro cell models are attractive alternatives that provides more control to study the disease. The most common *in vitro* equipment are hypoxia chambers and incubators that create global hypoxia in the cell culture. Other common methods utilize enzymatic oxygen scavengers (e.g. glucose oxidase with catalase) and HIF-1α degradation inhibiting chemicals (e.g. $CoCl_2$ and DMOG).[135,136] All these methods usually mimic hypoxia biology with a non-localized oxygen concentration across the cell culture and are hindered by the slow diffusion and equilibration of oxygen in liquid, making induction of hypoxia a slow process. Relevant to partial hypoxic insults, this however does not simulate the sudden/instantaneous hypoxic shock experienced *in vivo*.

Microfluidic devices and culture medium pre-treatments have been used to overcome some of these limitations.[137–139] For example, separation of toxic chemicals and reduction in equilibration time by flowing pre-equilibrated medium significantly improved mimicking hypoxia. Still, these methods are limited in their closed environment, impedance in intercellular interaction, the complexity in fabrication and maintenance and, most importantly, omission of spatial focal control of different oxygen levels in a single cell culture.[89,140,141]

The limitation in existing methodologies has caused complications in modelling acute hypoxic events, resulting in inaccuracy in using the definition of "acute hypoxia" in literature. Many publications have reported acute hypoxia in timescale of hours or more, occurring in the whole brain.[142] Acute hypoxia within minutes are also important in pathology but are less reported. For example in the brain, hypoxic stress on neurons can cause permanent damages within minutes but methods requiring hours to create hypoxia are still widely adopted in research.[75] A simple, robust, and spatiotemporally translatable *in vitro* cell model is required to address the cellular mechanisms underlying focal hypoxia.

The electrochemical oxygen scavenging model reported in the previous chapter offers an ideal solution to improve the spatiotemporal resolution of an acute focal hypoxia cell model. The work presented in this chapter is the proof-of-concept on applying the oxygen scavenging system on human neural progenitor cells. This study took advantage of the higher resilience to low oxygen concentration of progenitor cells than that of matured cells, for a clearer demonstration of the hypoxic response under electrochemically induced hypoxia. The spatiotemporal relationship of focal hypoxia to HIF-1α stabilization was investigated. Undesired side-effects of the electrochemical oxygen reduction reaction, generation of H_2O_2 and pH change, were also investigated for the impact on the normal cell culture growth (Fig. 3.1). The oxygen scavenging model was also tested on human cortical neurons, designed to investigate the cell fate after hypoxia and hypoxia/reoxygenation.

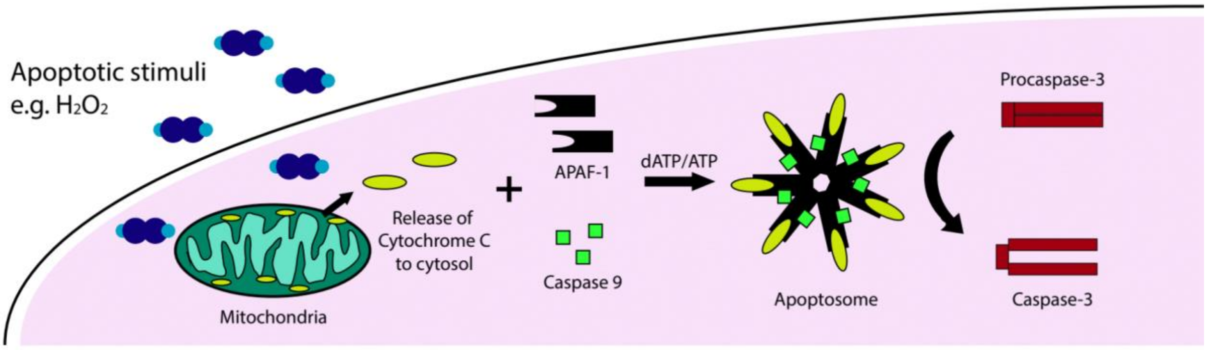

Figure 3.1. Schematic diagram of the cell signalling pathway of H_2O_2-induced apoptosis.

II. Materials and methods

II. I. Materials

The following items are obtained from Gibco: DMEM/F-12 with GlutaMAX (with or without phenol red), neurobasal medium (with or without phenol red), GlutaMAX, sodium bicarbonate, beta-mercaptoethanol, N2 supplement, B27 supplement (50x), B27 supplement without vitamin A (50x), insulin (human recombinant, zinc solution) and bovine serum albumin (BSA) fraction V (7.5%).

Phosphate buffer saline, water for cell culture, borate buffer (pH 8.5), glycine, triton x 100, Mowiol solution, bisBenzimide H 33258, hydrogen peroxide, horseradish peroxidase (HRP) and dimethyloxalylglycine (DMOG) were purchased from Sigma Aldrich.

Animal-free blocking solution, FGF, CHIR99021, Heparin and SB50 were obtained from Cell Signaling Technology. Poly-d-lysine 1mg/mL in water was obtained from Millipore. Accutase and MitoSpy Green FM were obtained from BioLegend. Laminin used was obtained from Cultrex.

Polydimethylsiloxane Sylgard 184 elastomer set was obtained from Sylgard. German glass coverslips (ø:12mm) were purchased from Bellco Glass Inc. and Fisher Scientific.

The primary antibodies used are the rabbit anti-HIF-1α monoclonal IgG antibody (#ab51608) from Abcam and cleaved-caspase-3 (Asp175) antibody #9661 from Cell Signal Technology. Phalloidin conjugated F-actin dye (CF® Dye Phalloidin Conjugates 00042-T Phalloidin CF488A Abs/Em(nm):490/515) was obtained from Biotium. Secondary antibodies used include Alexa Fluor 555-conjugated goat anti-rabbit polyclonal antibody and goat anti-mouse 647, and both were obtained from Invitrogen.

Amplex UltraRed was obtained from Thermofisher.

Human neural progenitor cells (Sheffield 6: PMID: 28594288) were obtained and investigated in this study.

II. II. Equipment and instrumentation

The following equipment and instruments were used:

2.6- litre Zepto Low Cost Plasma Laboratory Unit by Diener Plasma-Surface Technology, Centrifuge 5702 by Eppendorf, Low oxygen Incubator by Binder, Leica TCS SP5 Confocal and fluorescence spectrometer.

II. III. Cell culture conditions and maintenance

Three separate culture media, adopted from the Karadottir lab, were used in these experiments. First culture medium is the Neural progenitor Maintenance Culture Medium (NMCM). It contains 1:1 ratio of DMEM/F-12 (1:1) with GlutaMAX: Neurobasal medium, GlutaMAX (2mM), Beta-mercaptoethanol (0.1mM), N2 supplement (1x), B27 supplement without Vitamin A (0.1x), Insulin (10 µg/mL), FGF (10 ng/mL), CHIR99021 (3µM), Heparin (200ng/mL), SB50 (1µM), LDN-193189 (200nM), K02288 (100nM), MK-2206 (75nM) and AKTi8 (100nM). Second culture medium is the Neuron Differentiation Culture Medium (N2B27). It contains 1:1 ratio of DMEM-F12: Neurobasal medium, Glutamax (2mM), Beta-mercaptoethanol (0.1mM), N2 supplement (0.5x), B27 supplement (0.1x) and Insulin (10 µg/mL). The last culture medium used was the culture medium for oxygen scavenging, N2B27(–). It was the same components as N2B27 but without phenol red. Washing buffer (WB) was created by adding 0.075-0.1% BSA to DMEM/F-12.

Two different culturing surfaces were used in this study. Polystyrene surfaces such as 6-well plates / 12-well plates were prepared by adding laminin (1.5µg/cm^2) in PBS solution overnight in 4°C. Glass surfaces such as glass coverslips (ø: 12mm) were first placed in 24-well plates and cleaned with the plasma cleaner at 80% power for 10 minutes. They were first coated with poly-D-lysine at 3µg/cm^2 in pH 8.5 borate buffer for 1 hour at room temperature, followed by coating 1.5µg/cm^2 of laminin in PBS overnight in 4°C.

NPC stocks (5,000,000 cells / 500 µL) were stored in 10:1 culture medium:DMSO, stored in –80°C freezers. They were thawed at room temperature and immediately transferred to a 15mL

Falcon tube. WB were added to top up the media volume to 5mL. The cell stock was then centrifuged at 400x g for 3 minutes. Supernatant was aspirated and the cell pellet was resuspended in the NMCM and expanded on a 6-well plate. All cells are cultured in 5% O_2 / 7% CO_2 / N_2 balance at 37˚C unless specified.

Cells were re-plated when the cultures reached about 70% confluency. NPC were detached into small colonies (few cells as a clump) by incubating in PBS with 500 µM EDTA for 2 minutes. EDTA/PBS was aspirated, and WB was used to rinse and flush off the cells from the culturing wells. The solution was then collected in a 15mL Falcon tube and topped up with WB to 5mL. It was centrifuged at 300x g for 3 minutes. Cell pellet obtained was resuspended in NMCM. NPC were replated at cell density of 50,000 cells /cm^2 and 100,000 cells /cm^2 in maintenance culture and coverslips for experiments, respectively.

NPC differentiation was performed mostly on 6-well plates. NPC were detached as single cells by incubating in Accutase at 37°C for 5 minutes. The cell containing solution was briefly triturated, at most 5 times, to separate the cells and transferred into a 15 mL tube. The solution was topped up till 5mL and then centrifuged at 400x g for 3 minutes. Cells were replated at 100,000 cells/cm^2 in 6-well plates and cultured in N2B27 for 14 days, changing culture medium for every 2-3 days, till matured.

Cell culture technique was trained by Dr. Balazs Varga in the Karadottir Lab. All subsequent cell culture maintenance, differentiation, cell plating and preparation for experiments were my own effort.

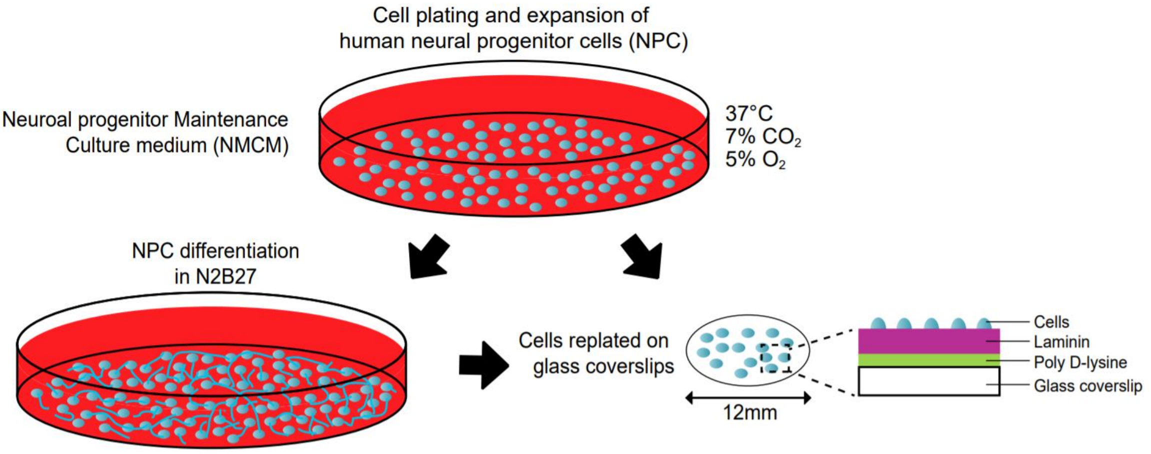

Figure 3.2. Schematic diagram of neural progenitor cell culture and neuron cell culture and glass coverslip for hypoxia experiments

II. IV. Local hypoxia device fabrication and assembly

Double sided tapes were applied to adhere the bases of three cylindrical sample holders (ø: 17mm) on the polystyrene petri-dishes (ø: 55mm). PDMS was chosen as the preferred material here due to its superior oxygen diffusion capability and high oxygen capacitance for developing an oxygen gradient. PDMS with 10:1 elastomer and curing agent ratio was used to fill up the space in the petri-dish. The device was placed under vacuum to remove the gas trapped in the PDMS mixture. It was then placed in a pre-heated oven at 80°C for 1.5 hours until the PDMS had cured. The sample holders were thus removed, and the final product was placed in room temperature overnight before ready. To connect the electrodes, 3 holes was opened at the lids of the petri-dishes with a soldering iron. Prior to experiments, the hypoxia devices were plasma cleaned. Electrodes, cleaned as reported previously, were pulled through the holes, and fixed with Blu Tack.

II. V. Hypoxic stress induction

II. V. I. Hypoxic response in NPC

Electrochemically induced hypoxic stress was applied on NPC and their hypoxia response was investigated. Experiments were conducted on NPC 2-4 days after replating onto the glass coverslips. Before conducting the oxygen scavenging, the coverslips were transferred from a 24-well plate to the PDMS electrochemical system (fig. 3.3). 1.7 mL of N2B27(–) medium was added to each well. Since HIF-1α was used as the readout of hypoxic response in immunofluorescent imaging, the positive control contains 250μM DMOG, a prolyl-4-hydroxylase inhibitor which upregulates HIF-1α in cells. The electrodes were cleaned as discussed in the previous chapter and slotted through the holes at the polystyrene lid, fixed by Blu Tack. The scavenging electrode was positioned at 2 ± 0.5 mm above the cells and polarized at –0.7V for 1 hour, 3 hours and 6 hours. Immunofluorescent staining of hypoxic sensing protein, HIF-1α was performed for investigating the translocation and colocalization with cell nucleus. Six fields at 63x magnification were randomly selected and imaged by confocal microscopy on each of the three biological replicas, resulting in a total of 18 images per condition for analysis.

In the investigation of acute hypoxia, the scavenging electrode was polarized for 20 minutes, 40 minutes and 60 minutes. Immunofluorescent staining of HIF-1α and actin was performed to investigate the cytoplasmic stabilization of HIF-1α prior to translocation to the cell nucleus. 63x magnification was used for imaging. Other settings are the same as that described above.

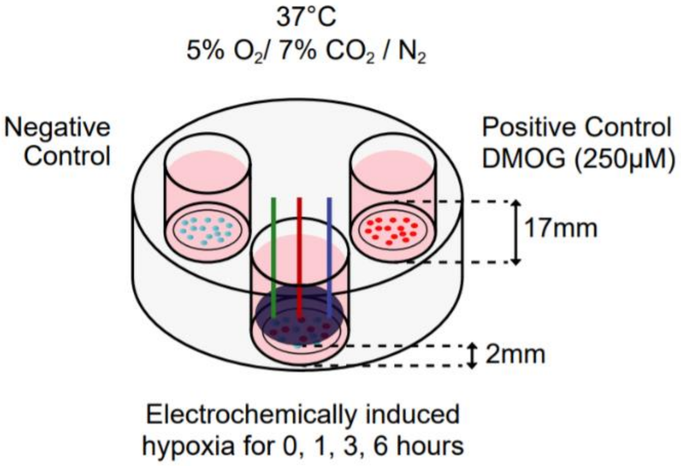

Figure 3.3. Schematic diagram of the experimental set up for investigating hypoxic stress induction on NPC.

II. V. II. Focal hypoxia in NPC

Generation of focal hypoxia was investigated by using half of the Pt/C electrode, characterized in the previous results chapter. In brief, the disc shaped Pt/C was cut in half and placed at the right half of the electrochemical cell (fig. 3.4). The distance between the cells and the polarized electrode was maintained at either 2 mm or 3 mm. Electrochemically induced focal hypoxia was applied for

3 hours and results were compared with negative control, positive control with 250µM DMOG and an unpolarized half electrode at 2 mm height. HIF-1α in NPC were thus immunofluorescent stained. Tile scans (2 x 12) were conducted with confocal microscopy along the axis from the left to right, spanning from the area furthest from the scavenging electrode to that directly underneath. Tiles were grouped and analysed based on their respective radial distances. Minimum intensity thresholds are selected as the signal intensity at mean + 3 S.D. at 0-hour treatment while maximum intensity was selected as the mode of the respective positive control.

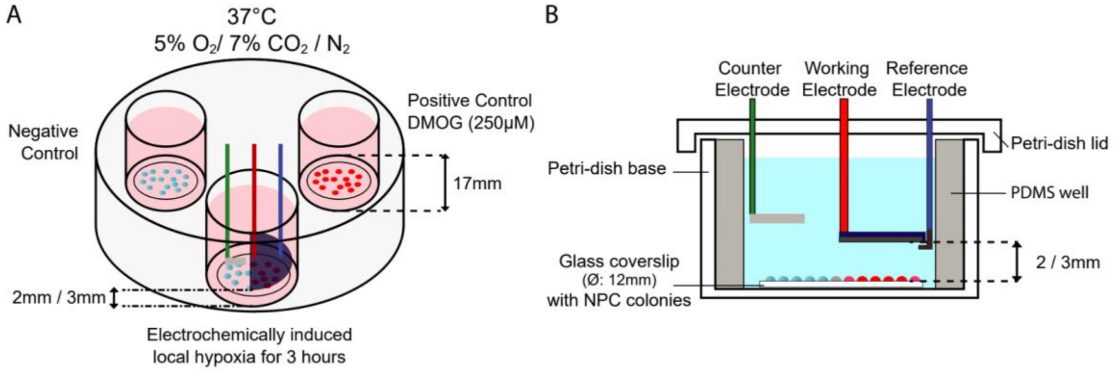

Figure 3.4. A: Schematic diagram of experimental set up for investigating focal hypoxia on NPC. B: Cross section of the electrochemical cell.

II. V. III. Hypoxia and reoxygenation in neurons

Hypoxia tolerance and effect with reoxygenation were investigated on human cortical neurons with infused oxygen degradation domain (ODD) – GFP clone. Human cortical neurons 28+ days (differentiated for 14 days in N2B27 and replated for 14+ days) were subjected to electrochemically induced hypoxia. The experimental set up was the same as that in figure 3.3. Neurons were subjected to hypoxic stress for 3 hours and 6 hours by scavenging electrode at 2mm height. Half of the samples was fixed in 4% PFA immediately after hypoxia whereas the other half had medium changed to fresh N2B27 and were cultured overnight before fixing. HIF-1α and TUBB3 were immunofluorescent stained.

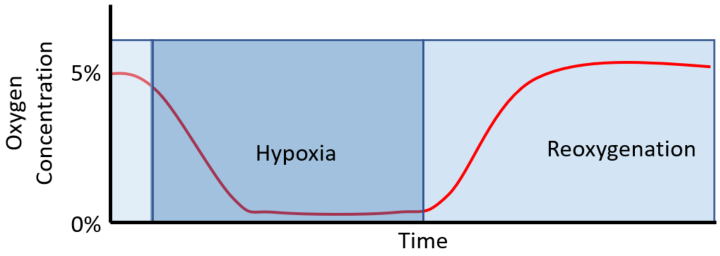

Figure 3.5 Schematic of oxygen concentration change in the neuron cell culture.

II. VI. Possible adverse side-effect by electrode

II. VI. I. Hydrogen peroxide generation and pH

pH and H_2O_2 concentration were measured after polarizing the electrode for 30 minutes and 3 hours. Measurements were conducted in a 100mM KCl with 40mM phosphate buffer electrolyte (PBKCl) with or without catalase (1.25µg/mL), which simulates the buffering capacity and catalase concentration present in the neural maintenance medium. H_2O_2 measurement by fluorometric assay is reported in the latter section.

II. VI. II. Hydrogen peroxide induced apoptosis in NPC

The effect of H_2O_2 at different concentrations were studied on NPC cultures. Cells were cultured in their basic culture medium with H_2O_2 which are supplemented with or without 1.25µg/mL of catalase. H_2O_2 of final concentrations 1µM, 10µM and 100µM were added to both types of culture medium immediately before loading to cell cultures. Staurosporine 100nM, a broad-spectrum protein kinase inhibitor was added to the media as the positive control. Cells were cultured for 4 hours in 5% O_2 incubator and fixed afterwards. Caspase-3 and actin were imaged with confocal immunofluorescent staining. 7 fields were imaged per biological replicate (n = 3). Apoptotic cells were quantified by their respective caspase-3 positive signal around the cell nucleus. Results were quantified and compared with paired t-test.

II. VI. Immunofluorescent staining

The cell culture coverslips were fixed with 4% paraformaldehyde (PFA) for 10 minutes and rinsed twice with PBS. Fixed samples first had the non-specific binding sites blocked with Animal Free Blocker and Diluent (AFB) containing 0.3M glycine and Triton x 0.1 for 1 hour in room temperature. The primary antibody stocks were diluted in AFB at 1 in 200 and added to samples for 2-hour binding reaction at room temperature or overnight at 4°C. Slides were then rinsed three times in PBS with Triton x 0.1 for 5 minutes. They were incubated in AFB containing 2μg/mL Alexa Fluor 555-conjugated goat anti-rabbit polyclonal antibody for 1 hour at room temperature in the dark. Slides were rinsed 3 times with PBS Triton x 0.1. Phalloidin iFlour conjugate stock (for actin staining) was diluted at 1 in 50 with PBS and incubated with each coverslip for 20 minutes in room temperature. Slides were rinsed 3 times with PBS Triton x 0.1. BisBenzimide H 33258 (1:10000 in PBS) were added to each coverslip to incubate for 1 minute and rinsed in deionized water. Excess water was soaked with a tissue. 7μL of Mowiol solution was dropped onto glass slides for each coverslip mounting. The glass slides were dried in the dark overnight and stored in 4°C before confocal images were taken.

In the neuron culture, mouse anti-TUBB3 and rabbit anti-HIF-1α were diluted 1:1000 and 1:200 in AFB respectively for the 4°C overnight primary antibody staining. Goat anti-rabbit 555 and goat anti-mouse 647 were both diluted by 1:500 in AFB for 1-hour secondary antibody staining.

II. VII. Fluorescence assay for H_2O_2 detection

The fluorometric assay was performed to measure H_2O_2 concentration in PBKCl and culture medium, using the enzymatic assay as follow:

$$\mathrm{H_2O_2} + \text{Amplex UltraRed} \xrightarrow{\text{Horseradish Peroxidase}} \text{Resorufin} + \mathrm{H_2O} \tag{3.1}$$

HRP catalyzes the H_2O_2 and Amplex UltraRed reaction to produce resorufin and water molecule. Horseradish peroxidase (HRP) stock solution was made at 10 U/mL in water, stored in the fridge. Stocks of Amplex UltraRed reagent were created by adding 340 μL of DMSO into the vial containing 1 mg of the reagent, giving 10 mM stock. Small aliquots of the stock were stored in the –20ºC freezer to avoid the freeze-thaw cycle and exposure to light. Upon measurements, the aliquots were thawed and diluted 100-fold in DMSO to 100 μM stock solution. The final working solution contains the final concentration of 50 μM Amplex UltraRed stock, 1 U/mL HRP and 40 μL sample in the 100 μL solution. The standard curve for H_2O_2 was made for the concentration range 0 – 2 μM H_2O_2, which is freshly titrated from 30% H_2O_2 stock. The fluorescence emission spectrums were conducted at Em: 490nm and calibration curves were fitted at Ex./Em.: 490nm/592nm in PBKCl (Fig. 3.6) and at Ex./Em.: 490nm/582nm culture medium (Fig. 3.7).

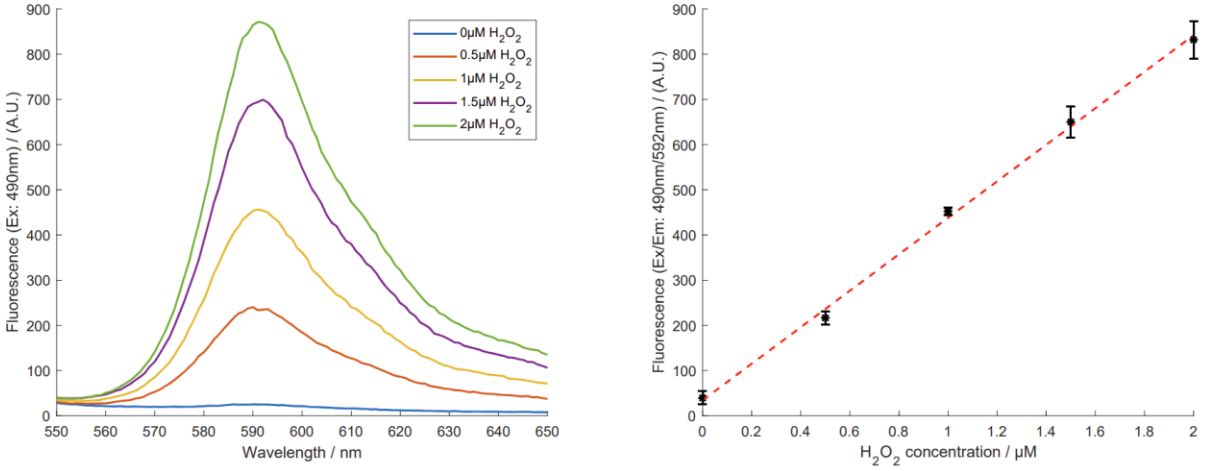

Figure 3.6. A: Fluorescence spectrum of Amplex UltraRed in PBKCl under excitation wavelength 490nm. B: Calibration curve of Amplex UltraRed emission intensity against hydrogen peroxide concentrations (Ex.: 490nm; Em.: 592nm). The linear fit is y = 403.7x + 34.4.

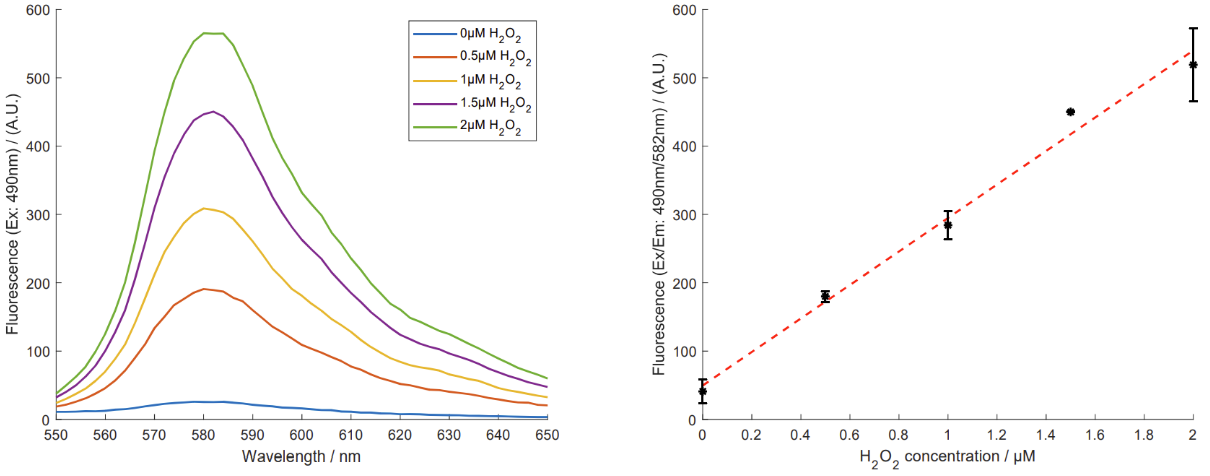

Figure 3.7. A: Fluorescence spectrum of Amplex UltraRed in culture medium under excitation wavelength 490nm. B: Calibration curve of Amplex UltraRed emission intensity against hydrogen peroxide concentrations (Ex.: 490nm; Em.: 582nm). The linear fit is y = 245.2x + 49.7.

II. VIII. Data processing and statistical analysis

The immunofluorescence images had the cell count and respective signal intensities quantified by the Volocity software and ImageJ. Results are plotted in graphs presenting the mean percentage ± standard deviation. Signal intensities were compared after being normalized to their respective positive controls. All results were compared statistically by paired t-test or ANOVA. Holm-Bonferroni test and Dunnett's test were conducted on the resultant p values to avoid type I errors and p values less than 0.05 were considered statistically significant.

III. Results and discussions

III. I. Electrochemical hypoxia on human neural epithelial cells

III. I. I. Hypoxic response induced by electrochemical oxygen scavenger

The efficiency of electrochemically induced hypoxia was investigated on HIF-1α nuclear accumulation in NPC (fig. 3.8). Confocal images of immunofluorescent staining showed that HIF-1α accumulation co-localised with nuclear staining with the duration of electrochemical oxygen scavenging (fig. 3.8A). This was equally observed in treating NPC with DMOG, the prolyl-4-hydroxylase inhibitor, for 6 hours. The lowest HIF-1α intensity was expectedly observed at negative control which cultured in 5% O_2. Nucleus integrity was evident in all electrochemistry-induced hypoxia, providing evidence against anoxia-induced necrosis. HIF-1α intensity was quantified and plotted against the duration of electrochemical hypoxia (fig. 3.8B). Nuclear HIF-1α accumulation increased over time. Percentage of cells in the field above background HIF-1α value (negative control) were recorded as 42% at 1 hour ($p < 0.05$), 86% at 3 hours ($p < 0.05$) and 95% at 6 hours ($p < 0.05$). The intensity plateaued after 3 hours at an intensity comparable to the positive control. A time-dependent sigmoidal increase of cells attained maximum nuclear HIF-1α intensity (compared to that in DMOG) whereat 12% at 1 hour, 66% at 3 hours ($p < 0.05$) and 73% at 6 hours ($p < 0.05$) (fig. 3.8C). This suggested that the electrochemical oxygen scavenger was competent in creating rapid hypoxia sensed by NPC in real time.

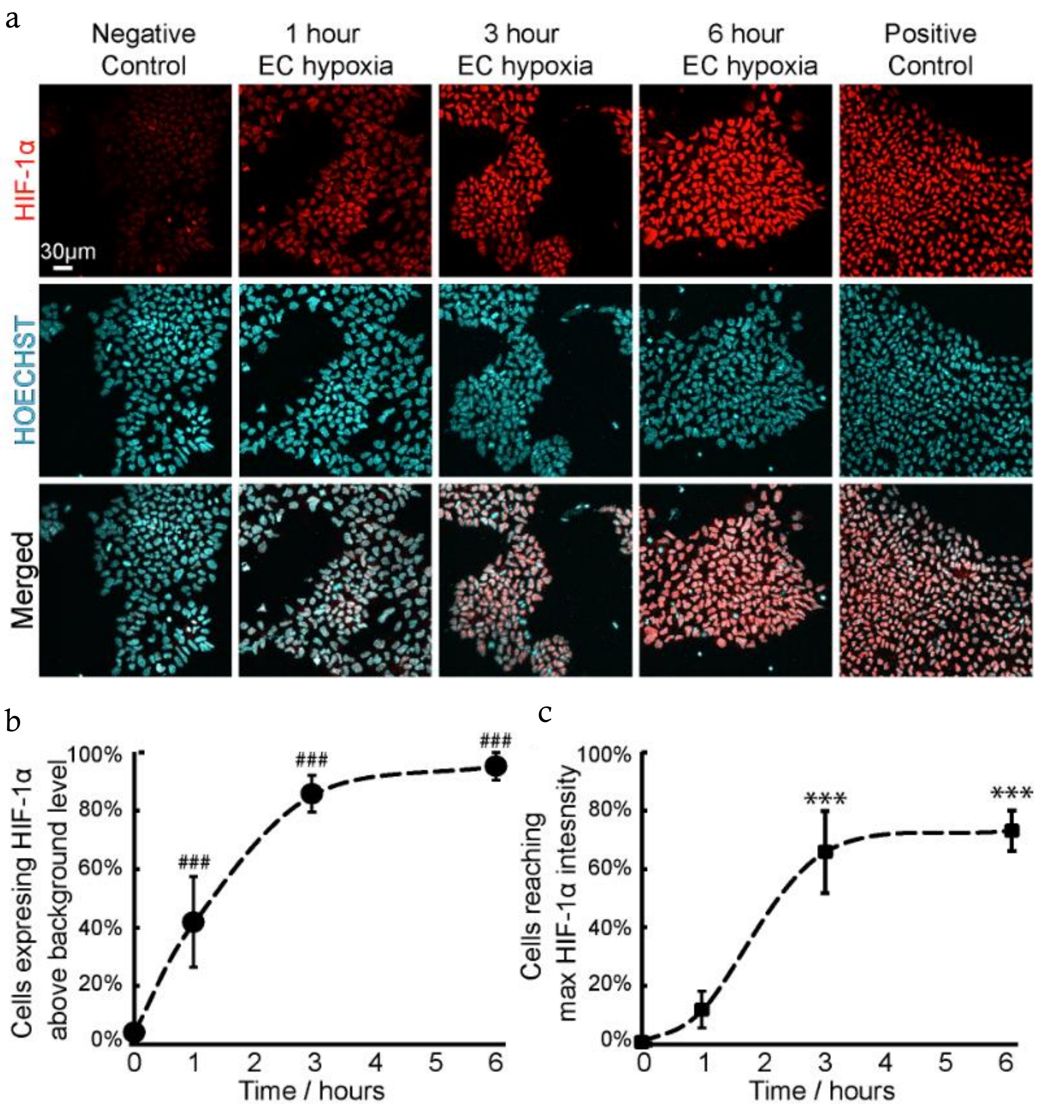

Figure 3.8. Human neural progenitor cells subjected to varying degree of electrochemical hypoxia. Each time point was a separate experiment fixed with 4% PFA and thus immunofluorescent stained. A. Confocal images of neural progenitor cells with immunofluorescent staining (HIF-1α: red; nucleus: blue) under different duration of hypoxic stress by electrochemical oxygen scavenging. Positive control: 250μM DMOG for 6 hours. B. Percentage of cells with HIF-1α expression above base fluorescence intensity (mean of negative control). C. Percentage of cells reaching maximum HIF-1α fluorescence intensity (mode of positive control) (n = 3, error bars indicate standard deviation). Scale bar: 30μm.

III. I. II. Acute hypoxia

To investigate the competence in the system in creating acute hypoxia, the dynamics in cytoplasmic and nuclear HIF-1α in NPC within the first hour was investigated before the steady state hypoxia was achieved in the cell culture. Confocal images showed nuclear co-localised HIF-1α increased after 20 minutes of hypoxia ($p = 0.0026$) but gradually decreased over time (Fig. 3.9). However, the cytoplasmic HIF-1α lagged and increased drastically thereafter ($p = 0.0328$ at 40 minutes of hypoxia). This suggests rapid HIF-1α nuclear translocation when oxygen level just dropped below ~2% (15mmHg), shown in the characterisation experiment reported in the previous chapter (fig. 2.37). These results are expectedly related to the stabilisation of proline (Pro^{402}) at the N-terminal of oxygen degradation domain in HIF-1α, whereat PHD1 and PHD2 fails to hydroxylate from 2% O_2.[24] The spatiotemporal relationship of HIF-1α stabilization is however not understood and should be further investigated. These results showed how the control of oxygen scavenging can reveal details of the effect of hypoxia. The difference against the observation in figure 3.8 is attributed to the difference in analytical method that laser power, gain and thresholding were different.

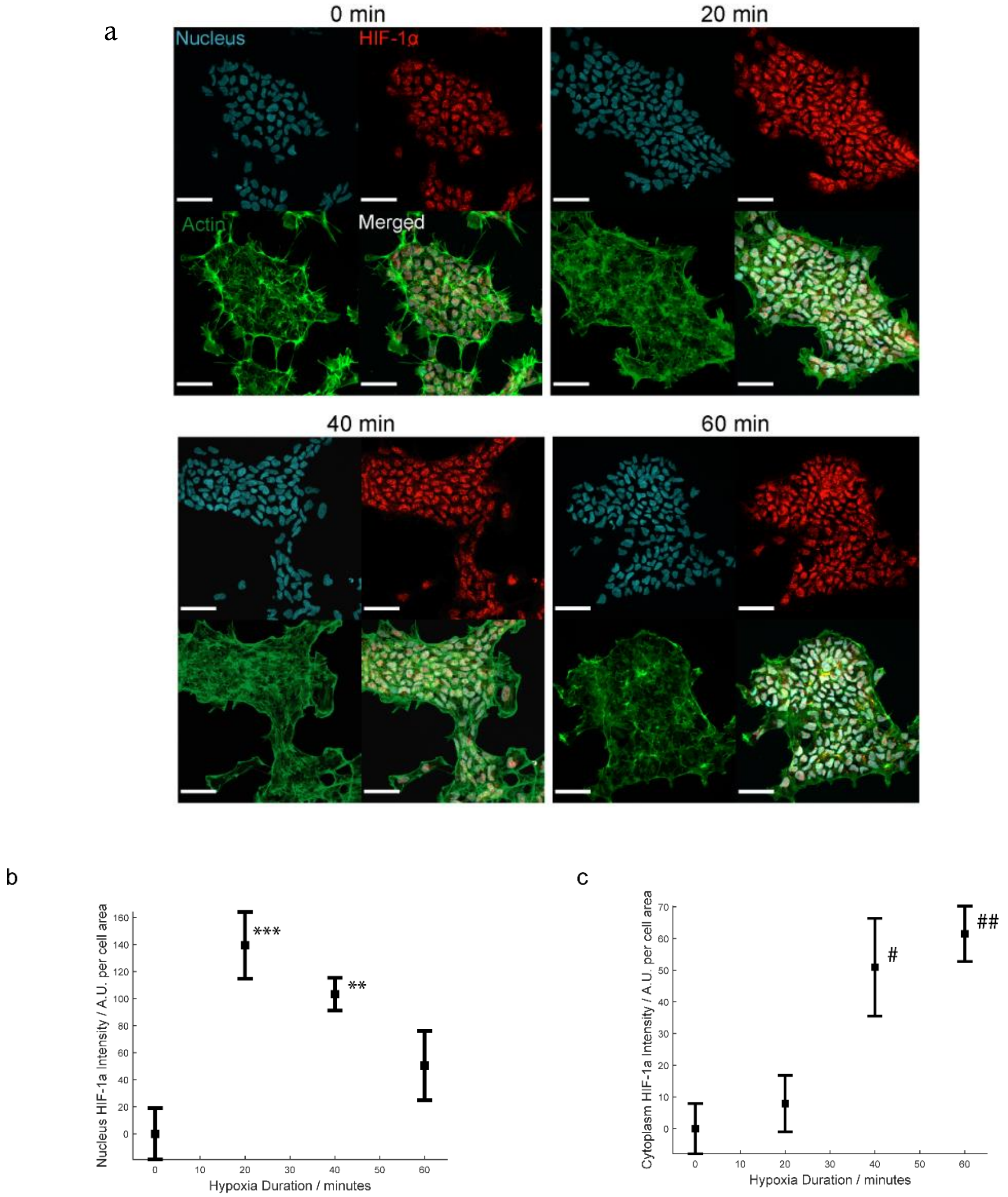

Figure 3.9 A. Confocal images of NPC for different durations of electrochemical hypoxia: HIF-1α (red), nucleus (blue) and actin (green). B, C, Quantitative analysis of nuclear HIF-1α (B) and cytoplasmic HIF-1α (C) normalized to respective negative control. Mean ± S.E.M. were plotted and compared with ANOVA and Dunnett's test. ** $p = 0.0026$; *** $p = 0.0002$; # $p = 0.0328$; ## $p = 0.0259$. Scale bar: 50µm. Note that the laser power and gain used here is different from that in figure 3.8.

III. II. Elimination of undesired side-effects

III. II. I. pH change and H_2O_2 generation

It is important to eliminate the incidental undesired side-effects incurred from electrochemical-induced hypoxia in cell cultures. Oxygen reduction is a 2 or 4-electron reduction reaction and the preferred pathway, depending on pH, on platinum/platinum-containing materials reported in literature is the 4-electron pathway producing H_2O. Other products can include H_2O_2 and OH^-; the former is known as a cell apoptotic signalling molecule at high concentrations. Besides, pH homeostasis is important for biological functions, protein activity and stability.[143–145] To test the rate of product accumulation in the electrochemical scavenging system, H_2O_2 concentration and pH were measured in PBKCl and culture medium undergoing oxygen reduction.

Before electrochemical scavenging, pH recorded in both conditions of PBKCl were 7.3 ± 0.1. After 30 minutes and 3 hours of electrochemical oxygen scavenging, pH in all conditions (n = 3 for each condition) did not change, or within the standard deviation. In DMEM / F-12, the initial pH of catalase (+) and catalase (–) electrolytes were 7.4 ± 0.1 and 7.6 ± 0.1 respectively. Electrochemical oxygen scavenging for 30 minutes and 3 hours did not change the pH in either case. While it is expected that catalase should not affect the pH, it was discovered that the buffer in the electrolytes (40mM in PBKCl and 29mM in DMEM / F-12) were able to maintain the pH at a stable value. It was concluded that pH changes were insignificant under all conditions tested. In addition, these pH measurements were recorded in bulk after the experiments. The localized pH should also be investigated in the future to complement the study. Since most fluorescent dyes are electrochemically active, fluorescence dyes should be fixed or crosslinked to the glass at the base for imaging. Carbon quantum dots serves as a potential candidate due to its stability, biocompatibility and pH sensitivity.[146]

H_2O_2 concentrations increased slightly over time as detected by the Amplex UltraRed fluorescence assay with the limit of detection of 0.3μM. Low and steady levels of H_2O_2 were detected in PBKCl at 30-minute and 3-hour electrochemical oxygen scavenging (0.8 ± 0.3μM), suggesting an equilibrium of production and degradation was reached. This is well below apoptotic H_2O_2

concentration. Furthermore, in DMEM/F-12 culture medium, H_2O_2 was barely detected with this fluorometric method. 0.4 ± 0.2μM and 0.2 ± 0.0μM H_2O_2 were estimated to present at 30 minutes and 3 hours, respectively. The decrease in H_2O_2 concentration over time may be accounted for by reactions of H_2O_2 with the components in the medium. It can also be related to the rise in pH and temperature that increases the decomposition of H_2O_2. Additionally, importantly, H_2O_2 accumulation could be further minimized with the addition of catalase at the concentration that is conventionally added to cell culture media. Localized H_2O_2 should also be studied in the future to complete the understanding of the scavenging system.

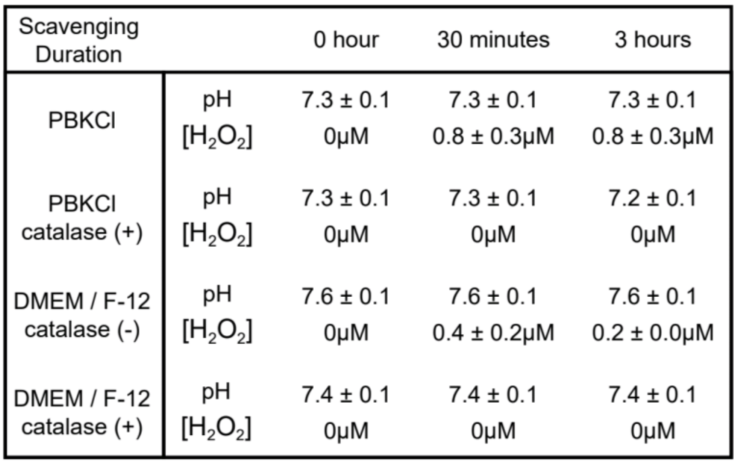

Scavenging Duration		0 hour	30 minutes	3 hours
PBKCl	pH	7.3 ± 0.1	7.3 ± 0.1	7.3 ± 0.1
	$[H_2O_2]$	0μM	0.8 ± 0.3μM	0.8 ± 0.3μM
PBKCl catalase (+)	pH	7.3 ± 0.1	7.3 ± 0.1	7.2 ± 0.1
	$[H_2O_2]$	0μM	0μM	0μM
DMEM / F-12 catalase (-)	pH	7.6 ± 0.1	7.6 ± 0.1	7.6 ± 0.1
	$[H_2O_2]$	0μM	0.4 ± 0.2μM	0.2 ± 0.0μM
DMEM / F-12 catalase (+)	pH	7.4 ± 0.1	7.4 ± 0.1	7.4 ± 0.1
	$[H_2O_2]$	0μM	0μM	0μM

Table 3.1 Table of pH and H_2O_2 generation in electrolytes under different durations of scavenging.

III. II. II. H_2O_2 induced apoptosis in NPC

To further investigate the H_2O_2 threshold at which morphological changes and apoptotic response become apparent, NPC were cultured in H_2O_2 for 4 hours (Fig. 3.10). Immunofluorescent images of NPC nucleus were intact in all catalase (+) culture medium and no signs of caspase-3 activation even up to 100μM H_2O_2. In catalase (–) culture medium, caspase-3 activation was observed at 10μM H_2O_2 ($p = 0.0036$) (Fig. 3.11). Morphological changes like actin degradation, nuclear condensation and fragmentation were only observed at 100μM H_2O_2 (Fig. 3.10). This confirmed that H_2O_2 accumulation by electrochemical oxygen scavenger is below the limit for caspase-3 activation such that the scavenging should not cause H_2O_2-induced apoptotic responses even in the absence of catalase.

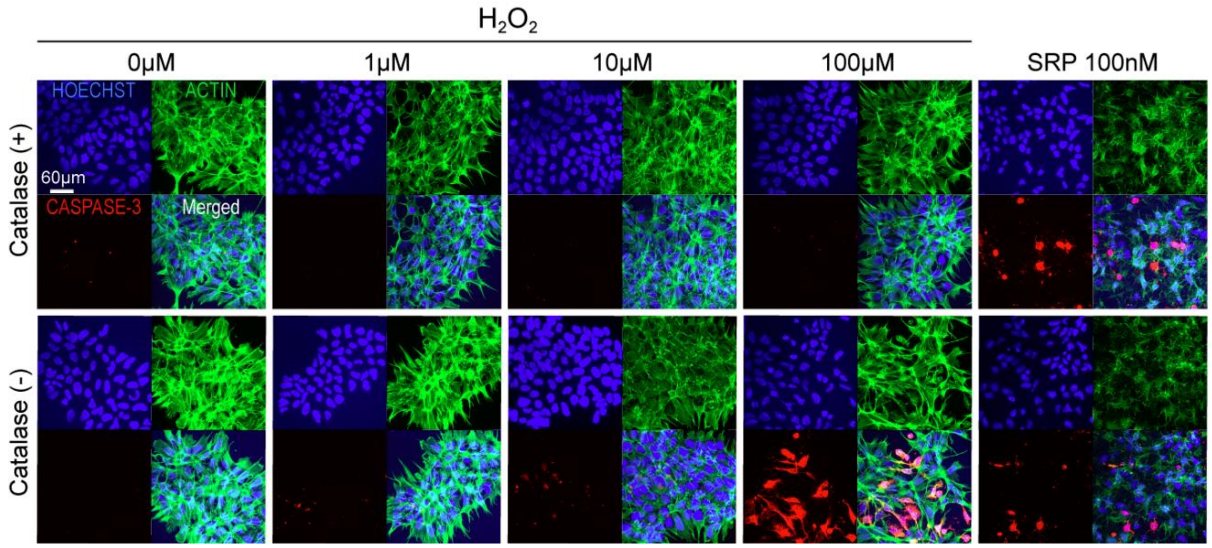

Figure 3.10 Confocal images of NPC caspase-3 upregulation study after subjecting to increasing concentration of H_2O_2 in culture medium with and without catalase. 100nM staurosporine was added the culture medium as positive control. All conditions were cultured for 4 hours before fixing and staining: nucleus (blue); actin (green); caspase-3 (red). Scale bar: 30μm. SRP: Staurosporine.

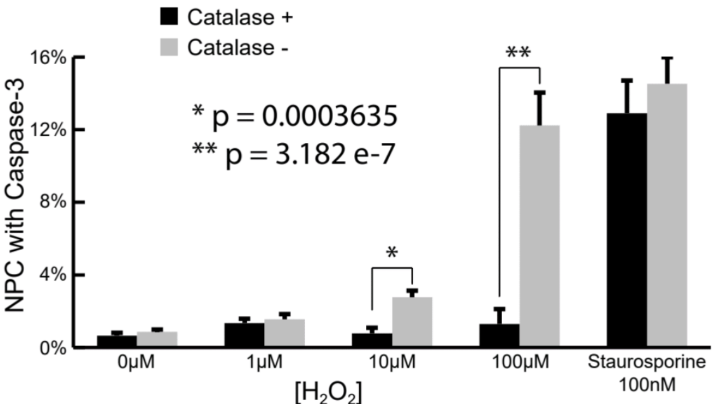

Figure 3.11 Quantified analysis of percentage of NPC showing caspase-3 activation under hydrogen peroxide. Results were compared with paired t-test.

III. II. III. Focal hypoxia under oxygen gradient

Electrochemically induced hypoxia was applied on one half of the cell culture and the cell responses were investigated (fig. 3.12). This system was characterized and reported in the previous chapter (see fig. 2.40). As expected, NPC subjected to electrochemical hypoxia showed remarkable similarities to the oxygen gradient recorded by the Clark electrode array. Immunofluorescent images of NPC at 2mm / 3mm electrochemical oxygen scavenging showed a gradient of HIF-1α intensity after 3 hours (fig. 3.13). The HIF-1α intensity was dependent on the respective positions of cells within the system, as well as the position of the electrode where 2mm in height expectedly caused a more hypoxic environment than the 3 mm set-up. The gradient hypoxic stress of NPC confirmed that the characterised oxygen gradient reported in fig. 2.40 was maintained over 3 hours. Quantifying the HIF-1α intensity verified that maximum hypoxic stress was observed under the oxygen scavenging electrode (shaded region) and reduced hypoxic stress was apparent at the edges due to the influx of oxygen from the air-water interface and across the PDMS-electrolyte interface (fig. 3.14). Cells under the 2mm set-up had a larger area with significantly increased HIF-1α. Yet, it is interesting to observe that the maximum HIF-1α intensity in both cases were relatively similar, likely due to reaching the maximum accumulation rate despite having a lower oxygen concentration at 2mm (figure 2.41). In the negative control and unpolarized electrode culture (at 2mm), HIF-1α intensity remained low and uniform across the plane.

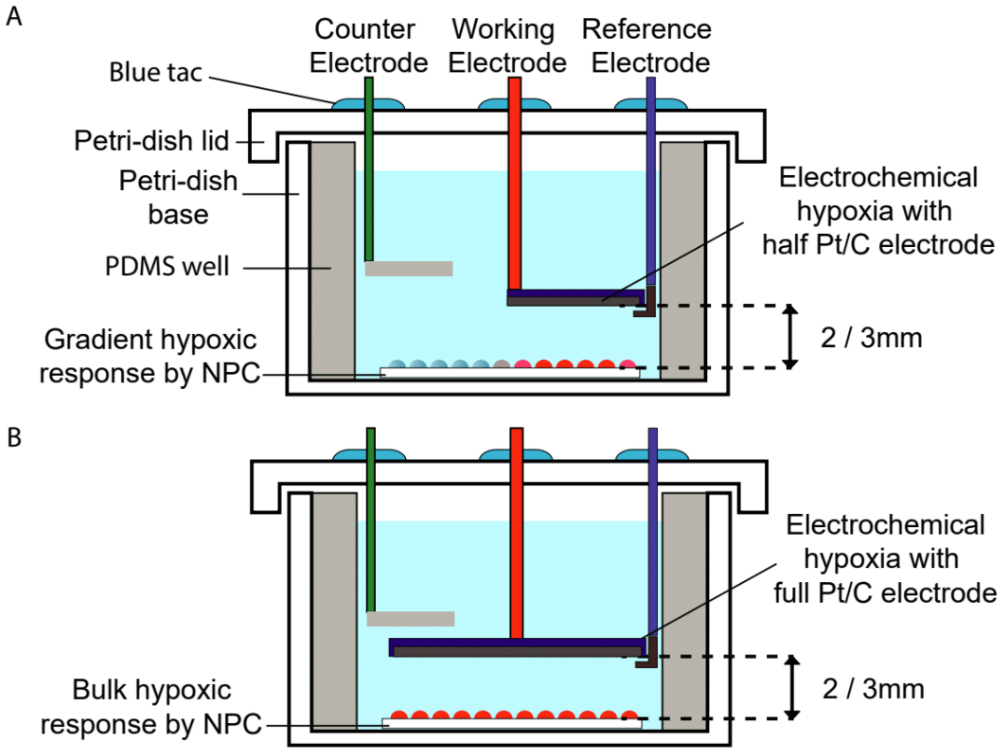

Figure 3.12 Schematic presentation of the hypoxic responses incurred by the modification of the oxygen scavenging electrode coverage.

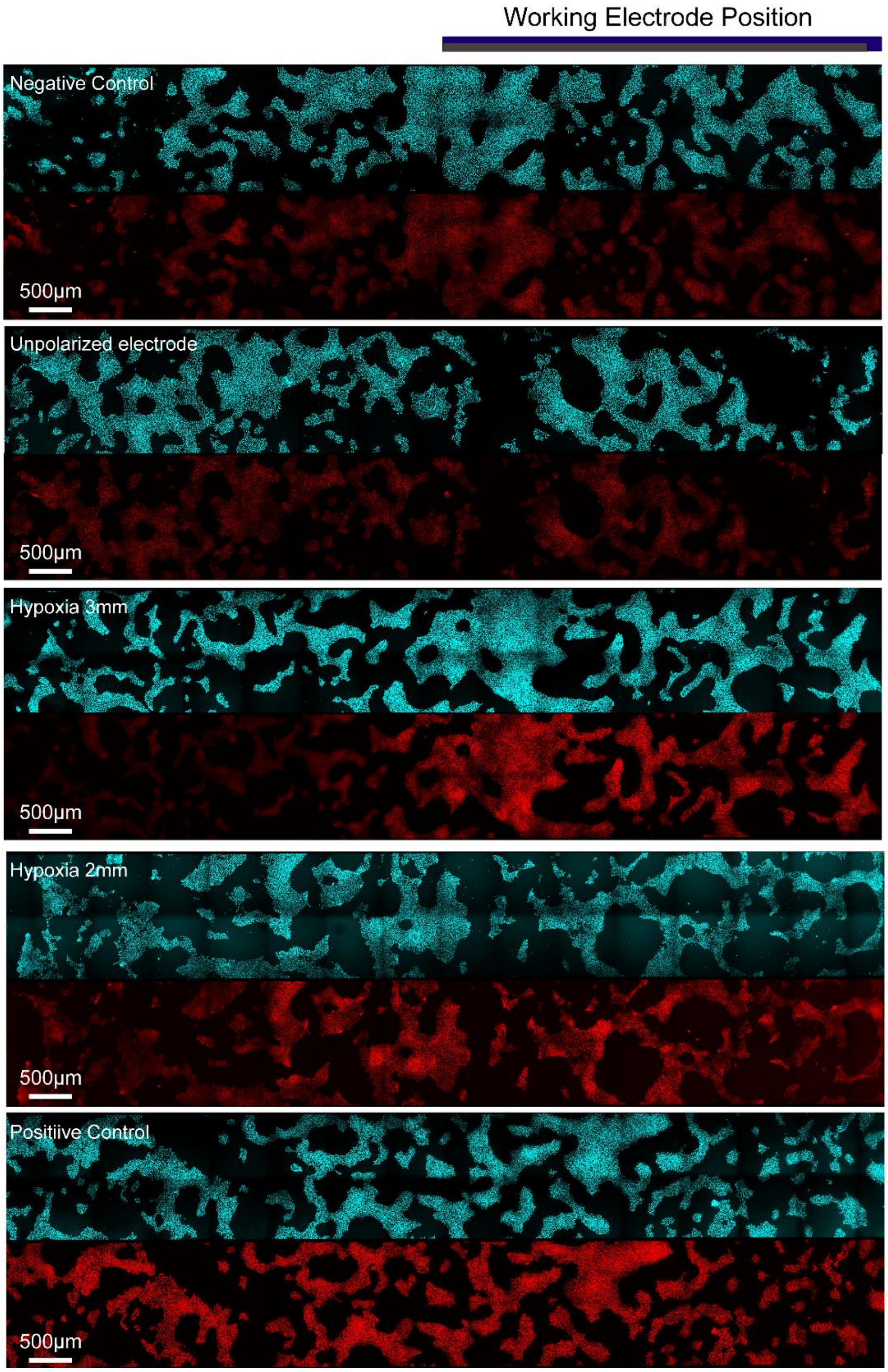

Figure 3.13 Confocal images of NPC culture subjected to focal hypoxia. Scavenging electrode is positioned on the right half. Its physical location is indicated by the schematics at the top of the figure. Immunofluorescent staining is nucleus (cyan, at the upper half of the image) and HIF-1α (red, at the lower half of the image).

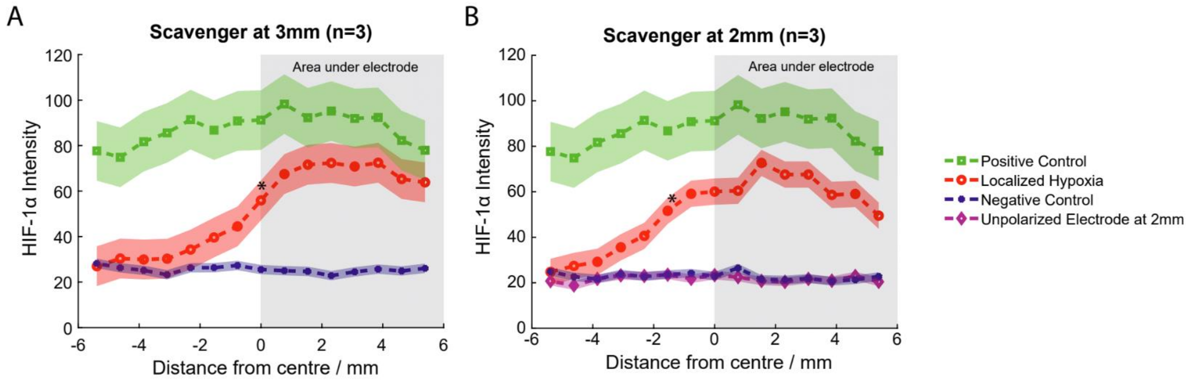

Figure 3.14 Quantitative analysis of mean HIF-1α intensity (curve) ± standard deviation (shaded region) across the base under 3mm (A) and 2mm (B) height of scavenging electrode. Green: Positive control (250µM DMOG); Red: Scavenging electrode polarized; Purple: Scavenging electrode unpolarized at 2mm; Blue: Negative control. Grey shaded area indicates regions under oxygen scavenging electrode. Tukey multiple comparison: * $p < 0.05$ for significant difference against respective negative control at the same position.

III. III. Hypoxia and reoxygenation on human neurons

To investigate the impact of hypoxia in the human brain, a preliminary experiment was conducted by applying electrochemical hypoxia on a simple *in vitro* model of human cortical neurons. These preliminary results were not completed with biological replicates for a conclusive discussion on the biological implications of hypoxia to human neurons.

Immunofluorescent stained neurons had HIF-1α and TUBB3 imaged by confocal microscopy to investigate the hypoxic signal response and axon integrity (fig. 3.15). HIF-1α in the negative control was at a relatively high intensity but sparsely distributed in both the cytoplasm and the nucleus. This showed despite culturing in 5% O_2, there were limited stabilized HIF-1α translocating to the cell nucleus for dimerization and transcription. Class III β-tubulin (TUBB3) were intact with no apparent fragmentations. When neurons were subjected to hypoxia, axon fragmentations were clear and became severe. However, it was interesting that HIF-1α nuclear colocalization was only observed after 3 hours but not after 6 hours of hypoxia. This could be accounted for by the cell death caused by prolonged hypoxic stress, evident from nuclear condensation observed at 6 hours but not 3 hours of hypoxia. The disruption in the plasma membrane and nuclear membrane integrity might lead to the leakage of HIF-1α to the surroundings.

Culturing in oxygenated medium overnight after hypoxia did not revitalize the neurons in both cases. Severe axon fragmentation was observed in both cases after reoxygenation. Despite not showing immediately after hypoxic stress, reoxygenation after 3-hour hypoxia also caused nuclear condensation, similar to that seen after 6-hour hypoxia. It also occurred that the HIF-1α intensity decreased significantly after the overnight culture, explained by the axonal fragmentation. The continuous neuron death at both time points may be triggered by uncontrolled glutamate and potassium ion releases and thus secondary damages due to the excitotoxicity.[39,147]

The absence of glial cells to support matured cortical neurons also contributed to the hypoxia susceptibility. For example, oligodendrocytes have been reported to provide metabolic support to axons and cell body in the brain, whereas astrocytes regulate and uptake the extracellular glutamate.[148,149]

It was also worth noting that the chemically induced hypoxia showed an obvious difference to that by hypoxia. HIF-1α nuclear colocalization and intact axons were visible after 15 hours of treating with DMOG, a prolyl-4-hydroxylase inhibitor, which only inhibits hydroxylating HIF-1α and thus its degradation via ubiquitination. There was however no sign of nuclear condensation and axon fragmentation despite the prolonged treatment. This proved that chemical-induced HIF stabilisation by DMOG could only mimic HIF-1α stabilization but not the entire range of biological effects caused by hypoxia.

Although the results of this experiment are non-conclusive, it was observed in the confocal images that axons grew erratically. This provides a strong reason in developing a microchannel device for more accurately model the human brain. Separating the axons from human cortical neurons is useful to understand the impact of oxygen gradients to their vitality. In addition, more robust investigation can be useful for discussing the role of oxygen in determining cell proliferation, fate, and morphogenesis of cells, particularly comparing with neural progenitor cells.[34,150]

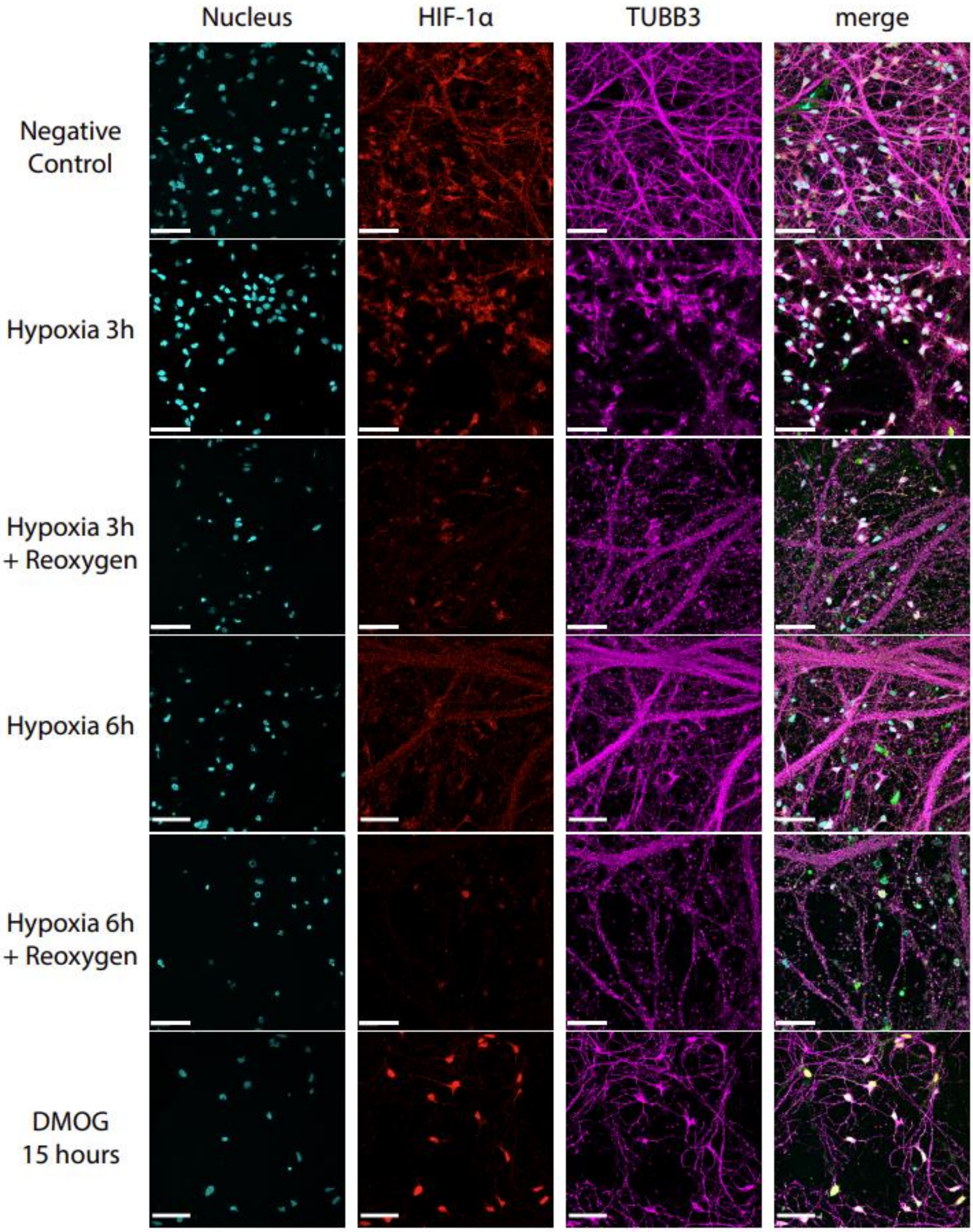

Figure 3.15 Confocal images of neurons after hypoxia and after reoxygenation. Positive control was incubated in 250µM DMOG for 15 hours. Blue: nucleus; Red: HIF-1α; Magenta: TUBB3. Scale bar: 50µm.

Hypoxic treatment with Scavenger 2mm	Nucleus condensation after hypoxia treatment	Tubulin fragmentation	Nucleus condensation after reoxygenation	Tubulin fragmentation after reoxygenation
3 Hours	No	Mild – Severe	Yes	Severe
6 Hours	Yes	Severe	Yes	Severe

Table 3.2 Summary of the morphological changes of human cortical neurons after hypoxic stress and overnight reoxygenation.

IV. Conclusions

Electrochemical hypoxia induced by the oxygen scavenging model was investigated for its efficiency and spatiotemporal potentials in this chapter. Experiments conducted on human neural progenitor cells and neurons showed hypoxia-dependent responses in HIF-1α transcription factor and morphological changes. Most importantly, it has achieved both spatial and temporal control without the use of chemicals and complicated microfluidic compartmentalisation of the reagents.

Initial experiments conducted on neural progenitor cells showed rapid cellular responses in 20 minutes and HIF-1α intensity plateaued after 3 hours, quicker than those reported in literature (4-8 hours, with continuous hypoxia).[151] Confocal images also revealed that HIF-1α accumulation occurred initially at the cell nucleus, followed by the slight decrease in the nucleus and an increase in the cytoplasm. Such interaction might be related to the complex relationships among prolyl-4-hydroxylases (PHD1, PHD2 and PHD3), ubiquitin and HIF-1α. Excitingly, local hypoxia can be tailored by modifying the electrode geometry to create different predetermined oxygen gradients in the cell culture. Preliminary results with the scavenging electrode covering half of the cell culture induced patterned HIF-1α response in the cells based on acute hypoxia by oxygen scavenging. Investigations in H_2O_2 generation and pH showed that the inexistence of undesired side-effect to cell culture. This evidence showed promising potentials of the system to investigate secondary damages caused by focal hypoxia to the surrounding normoxic tissues, as is commonly observed in many diseases.

Differentiated cortical neurons showed nuclear condensation and axon fragmentation after 3 hours of hypoxia. Reoxygenating the culture environment after hypoxic stress did not improve the damage but showed continued and widespread irreversible cell death. The follow-up investigations should consider (1) what the minimum time is that is needed to cause permanent damage to neurons,(2) whether focal hypoxia on axons only could cause axon fragmentation and nuclear condensation despite the cell body receiving sufficient oxygen and (3) how hypoxia preconditioning could affect the neuron responses to acute hypoxia.

Chapter 4: Microchannel device for neuron culture

I. Introduction

The human brain does not have a proper energy reserve, so that fluctuations in oxygen supply can cause severe and long-lasting neuronal damage, typically within minutes of hypoxic stress.[42,45,46] As reported in the preliminary results in the last chapter, human cortical neurons were shown to be more susceptible to hypoxic stress, compared to the neural progenitor cells. The hypoxic stress induced irreversible damage so that cell death could not be reverted simply by reoxygenation.

Interestingly, white matter, where most axons are located, was discovered to be at further distances than grey matter from the closest capillaries. It is thus reasonable to hypothesize that white matter is more vulnerable to hypoxia than grey matter. It was also reported in the literature that focal hypoxia in the brain deteriorates prognosis in age-related diseases. Yet, most *in vitro* cell models had axons crossing paths with neuron cell bodies and no clear separation of the tissues, that show minimum translatability to the layered tissue structure of the brain (fig. 4.1). It is thus of interest to develop a cerebral cell model and induce compartmentalized hypoxia, which has not been achieved by existing methodologies.

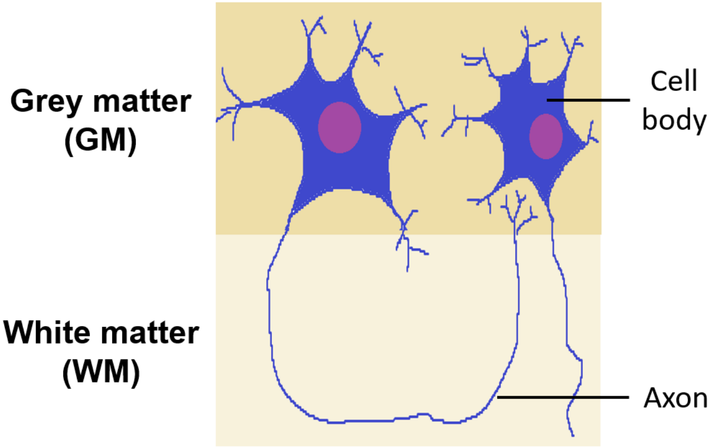

Figure 4.1 Schematic diagram of a human neuron showcasing the respective locations of the cell bodies and axons in the brain.

Commonly used neuron compartmentalizing methods are the Campenot chamber and closed-channel microfluidic devices. Campenot chambers are Teflon dividers attached to surface coated culturing plates with silicone grease.[152] It provides open chambers for containing culture medium and axons can grow through the silicone grease into the adjacent chambers. However, the chambers are difficult to maintain and fabricate since no strong chemical bonds were established to bind with the base. Moreover, silicone grease is not highly inviting for axonal growth, so that certain central nervous system neurons (such as cortical, spinal cord and hippocampal neurons) could hardly be developed in the Campenot chambers.[153] Many of these limitations were overcome by the development of microfluidic systems. Most microfluidic systems require pumps and pipes to maintain constant flow of the culture medium for maintenance. This not only increases the running cost of the culture maintenance, but also increases the risk of contamination and limits the culture medium conditioning required for healthy neuronal cultures. Improved microfluidic devices removed the pumps and pipes but still adopted closed channel designs. These designs are not applicable to efficient nutrient transfer and most importantly, the generation of hypoxic gradient to study diseases. A new approach is required for deciphering the pathophysiologies of Alzheimer's disease, stroke, and other hypoxia-related diseases.

The work presented in this chapter describes an *in vitro* human cerebral model engineered for investigating focal hypoxia. To simulate the local tissue structure of the human brain, a microchannel system was designed to separate the neuron cell bodies from the axons. The oxygen scavenging system developed and presented in the previous chapters was adapted for inserting into the microchannel system. Neurons subjected to focal axonal hypoxia were investigated for their cellular responses and morphological changes.

II. Materials and methods

II. I. Materials

Silicon wafer (4 in. diameter) was purchased from MicroChemicals GmbH, Germany. SU-8 2005 negative photo resist and SU-8 2025 negative photoresist were manufactured and purchased from MicroChem. The photolithography mask was purchased from Microlithography Services. Sterile disposable scalpel no. 10 was purchased from Swann Morton. Glass cover slides (22 x 60 mm, #1.5) were obtained from Fisher Scientific Menzel. Other biological materials used were the same as the previous chapter.

II. II. Equipment and instrumentation

Equipment used were the Karl Sus Contact Mask Aligner MJB-4, the POLOS spin coater, 2.6-litre Zepto Low Cost Plasma Laboratory Unit by Diener Plasma-Surface Technology, dataphysics OCA, DektaXT and ZEISS LSM 710 confocal microscope.

II. III. Silicon wafer mask fabrication

The microchannel device was fabricated with two layers aimed for creating the cell culture areas and the physical barriers on the silicon wafer. The silicon wafer (ø: 4in / 10.2cm) was cleaned, in sequence, with isopropanol and acetone for 10 seconds each. Clean wafer was dried with compressed gas or nitrogen gas. It was placed on a heating plate at 140°C for 5 minutes to allow solvents to completely evaporate and then cooled for 1 minute in room temperature. It was then placed at the centre of the spincoater and was held in place with vacuum. Protective shields were placed inside the spincoater to avoid spillage of photoresists. Two pipettes were used to deposit a total of 4mL of SU-8 2005 negative photoresist at the centre of the wafer and the spincoating process was begun swiftly to avoid evaporation of the photoresist and thus the coffee ring effect.

For the first layer, the spincoating process began with 5 seconds of 500rpm at 100rpm/s acceleration, followed by 30 seconds of 3000rpm at 300rpm/s acceleration. Upon completion, the wafer was pre-baked to remove the coating solvents in a two-step process, starting with 1 minute at 65°C and 2 minutes at 95°C. The UV mask (fig. 4.4B) was taped on the Telic glass panel with

Keplon tape and held on the holder of the photolithography machine. The wafer was placed on the platform and aligned with the UV mask. A soft contact UV exposure was set up to 2 doses of 4 seconds. The post-exposed wafer was placed at 65°C for 1 minute and 95°C for 3 minutes. It was then transferred to a wide bottom beaker containing PGMEA for the 2-minute feature development stage. The beaker was constantly moved to allow fresh PGMEA to react with the photoresist. The wafer was then cleaned with IPA and acetone and air-dried with pressured gas. The wafer was hard baked at 150°C for 15 minutes.

The process of creating the second-layer feature was done in similar procedures to the first layer with few parameter changes (mask used: fig. 4.4A). SU-8 2025 negative photoresist was spincoated on the surface with a maximum speed of 1700rpm. The wafer was then pre-baked at 65°C for 3 minutes and 95°C for 9 minutes. Before exposure to UV, the wafer had to be aligned with the UV mask for feature alignment. UV exposure was 2 does of 10 seconds, followed by a post-exposure baking at 65°C for 3 minutes and at 95°C for 7 minutes. A feature development time of 6-7 minutes was required. The final hard baking step requires 150°C for 45 minutes.

The microfabrication technique was introduced and trained by Dr. Janire Saez. Castaño. Design, optimisation of the technique for device fabrication and construction were my own effort.

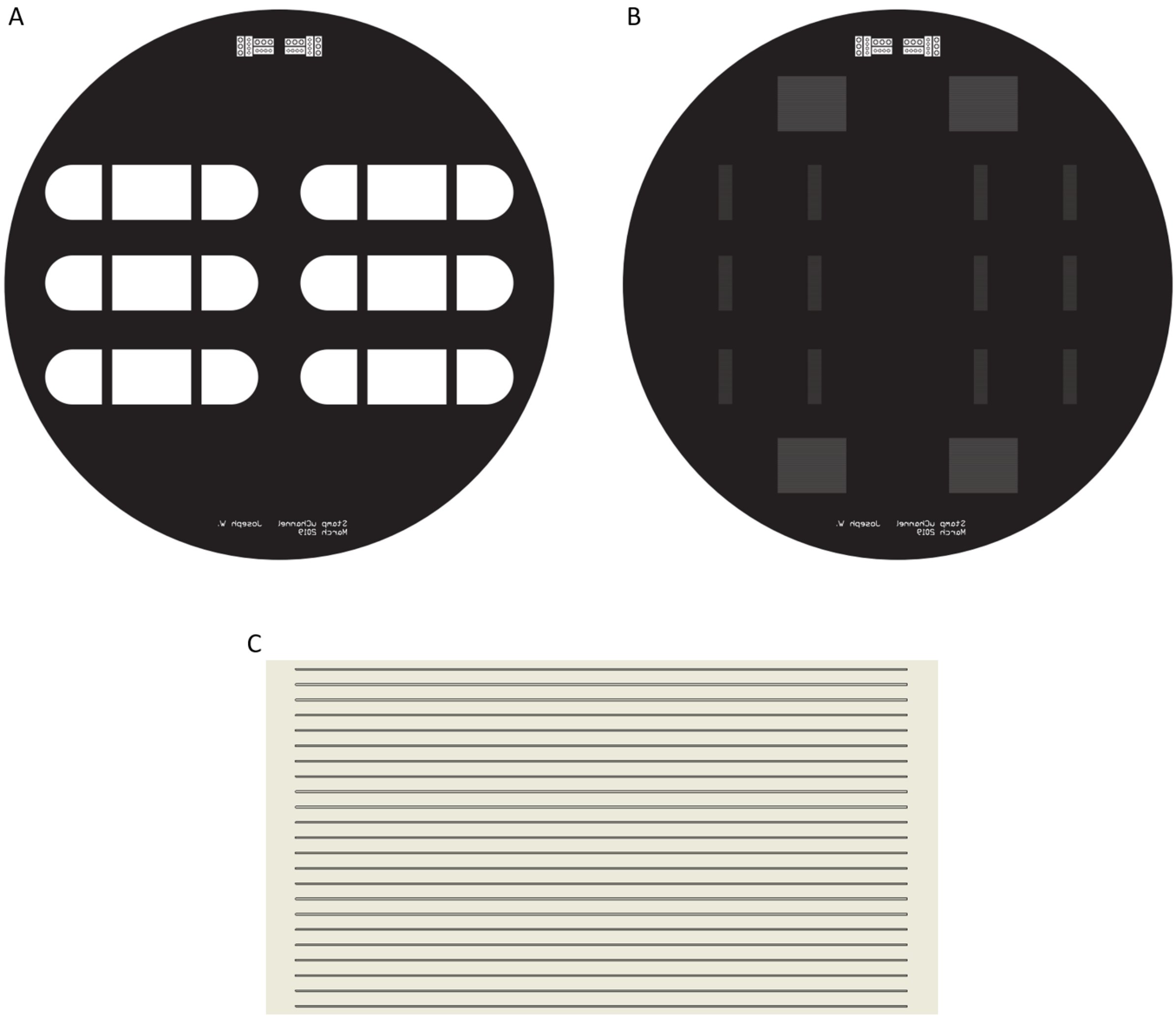

Figure 4.4 Photolithography mask used for creating the microchannel device. Microchannels (5μm width at 45μm gap) with 3μm in height were created with the *right* mask (B) followed by the culturing wells with the *left* mask (A) for 63μm in height. C: Zoomed in of the 5μm (width) x 2mm (length) microchannels.

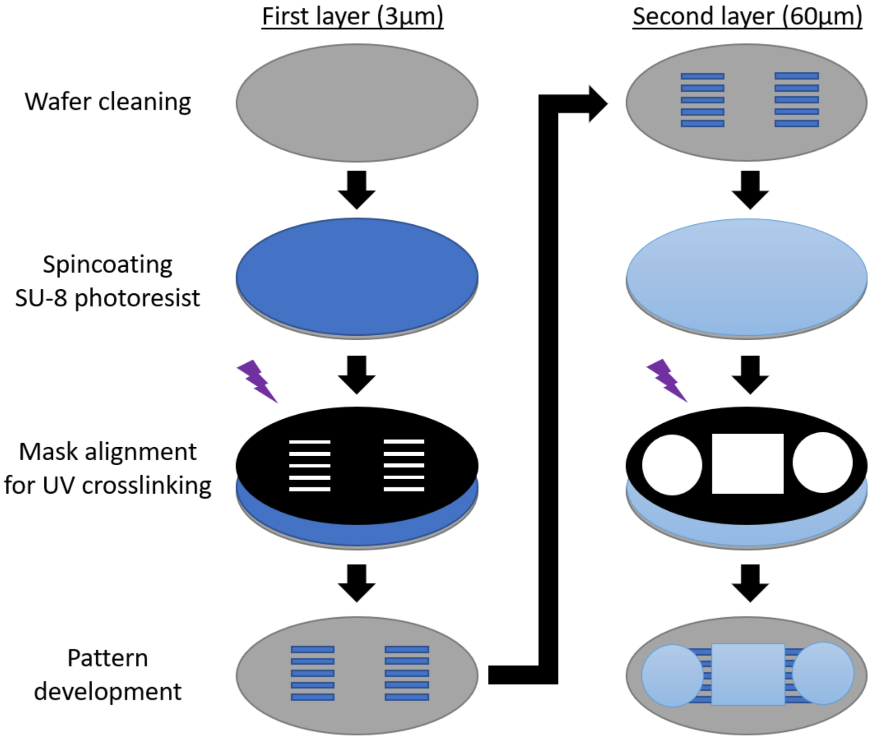

Figure 4.5 Schematic presentation of the microchannel device fabrication procedure by photolithography.

II. IV. PDMS microchannel device fabrication

The microchannel device was fabricated with PDMS due to its optical, oxygen diffusional and chemical favourable characteristics. The wafer with features was placed on a 140mm petri-dish. PDMS elastomer and curing agent were mixed in 10:1 ratio. The mixture was poured in the petri-dish with the wafer at the bottom. The 3D-printed block, with 6 legs of 8mm x 10mm, was placed in the PDMS mixture with each leg positioned directly on top of a central chamber to reduce the difficulty of cutting away cured PDMS. The combined device was then placed in the vacuum to remove the gas trapped in the PDMS mixture and the block. It was then placed on a heating plate and the block was carefully aligned with the central chamber markings on the wafer. The device was heated at 80°C for 1.5 hours until the PDMS had cured. Cured PDMS was first detached from the wafer with a scalpel as shown in figure 4.6A. The 3D-printed block was removed carefully. PDMS was then cut into separate pieces with a surgical scalpel (fig. 4.7A). 3-5mm distance from the features were kept for ensuring the PDMS walls having sufficient strength and rigidity after binding with glass. The trace amount of excess PDMS in the central well was removed by the scalpel. A biopsy punch (Ø: 8mm) was used to create the circular wells next to the central chamber. To shorten the distance for axonal growth into the central chamber, the punches were positioned to cut away a part of the channels (~700µm), with ~300µm remaining at the shortest part. A small distance between the open well and the microchannels existed as the legs of the 3D-printed block were slightly shorter than the photoresist master. The PDMS blocks had their features protected with Sellotape and placed in covered containers until they were ready for bonding onto glass. The final product of the device is presented in figure 4.7.

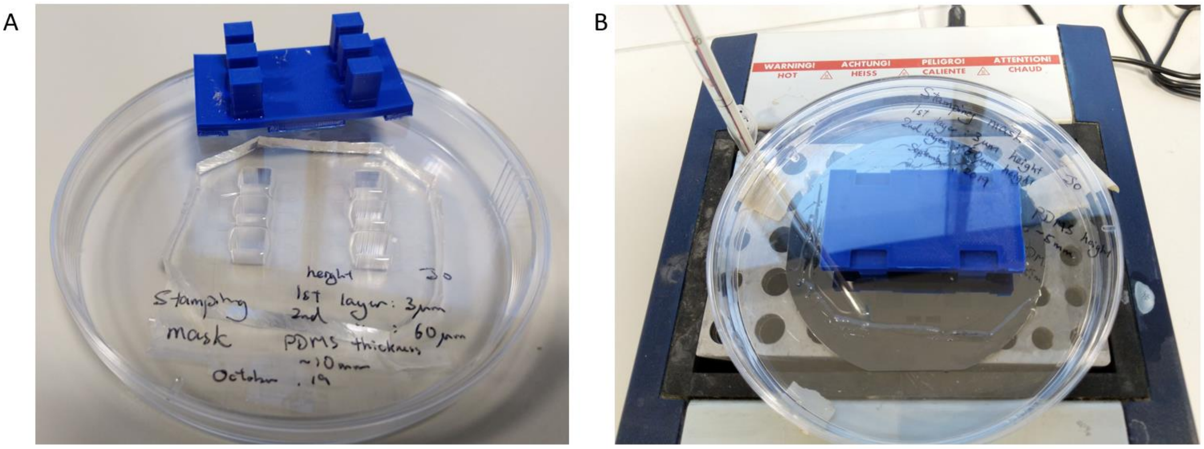

Figure 4.6 Images of the PDMS fabrication with the 3D printed block on the hot plate. A: the PDMS product cut out after curing process. B: PDMS with the 3D printed block curing on the hot plate at 80°C.

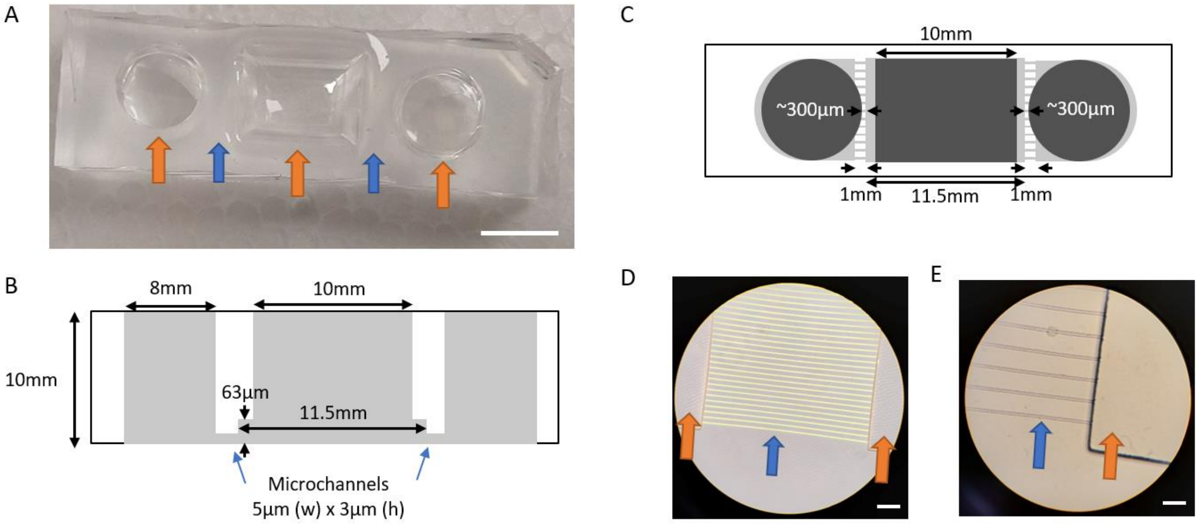

Figure 4.7 A: Final product of the microchannel device cast with PDMS. Blue arrow: microchannels; Orange arrow: open-well chambers. Scale bar: 8mm. B: Schematic diagram of the cross section of the microchannel device denoting the dimensions. C, Schematic diagram of the microchannel device from the top. Light grey region indicates the surfaces created from the photoresist whereas the dark grey region are the positions of the open wells. Circular wells were purposely punched on the channels to shorten the distance of axon outgrowth. D, E: Microscopic images of the microchannels (D) Scale bar: 200µm and (E) Scale bar: 50µm. Blue arrow: microchannels; Orange arrow: chambers for neuron culture, created by the second layer of spincoating at 63µm in height.

Glass coverslips (22 x 60 mm, Thermo Scientific Menzel #1.5) was used for the base of the microchannel device. The coverslips were first cleaned with ethanol, MilliQ water and then cleaned under air plasma at 70% power. They were placed in covered petri-dishes for 30 minutes to allow relaxation. PDMS block was cleaned by Sellotape to remove dust and PDMS debris. The PDMS block, bonding side facing up, and the glass coverslip were placed separately in the plasma generator and were oxygen plasma treated at 60% power (60W) for 45 seconds. The PDMS block was immediately pressed on the glass with moderate force without collapsing the microchannels. The bonded PDMS devices were then air plasma cleaned at 70% power for 10 minutes. 1mL of pH 8.5 borate buffer with 20µg/mL PDL was added to the PDMS device and incubated for 1 hour. The PDMS devices were then rinsed 3 times with PBS. Laminin in PBS were added to the wells and allowed to bond in the incubator overnight. The devices can be stored in the fridge after coating until use.

II. V. Neuron hypoxia in the microchannel device

II. V. I. Neuron culture and plating

Differentiation of NPC to cortical neurons were described in the previous chapter. Neurons expanded and differentiated in the N2B27 medium for 14 days were first detached from the culture well by incubating in Accutase for 15 minutes in the incubator. Neurons detached and suspending as a film in the Accutase were collected into a 15 mL Falcon tube without trituration. Wash buffer was used to top up the cell suspension to 5 mL, which was then centrifuged at 400x g for 3 minutes. After removing the supernatant, the cell pellet was triturated gently for 5 times in 1 mL N2B27. The cell density was then counted. If the cell density was below 10,000,000 cells/mL, the cells were centrifuged again and resuspended in volume accordingly.

To prepare the microchannel devices for cell loading, PBS with laminin in the culturing wells were aspirated but those within the microchannels was avoided. 100,000 cells (typically at 10 µL of medium) were aspirated with the pipette. The pipette tip was then angled towards the microchannels and cells were gently discharged. The microchannel devices were placed in the incubator for 15 minutes to allow cell attachment. The chambers were then filled with N2B27 medium, first at the central rectangular chamber and then at the side circular chambers. The central chamber was maintained at a higher volume height to create a constant solution outflow to the side chambers for deterring the neurons from migrating through the channels. Culture medium was half-exchanged with N2B27 every two to three days for a week. After day 7/8, culture medium refilled was changed to N2B27 with 20ng/mL BDNF, or neuron conditioned medium, which was a 1:1 mixture of fresh N2B27 and the one-week-old N2B27 used in dense human neuron culture.

To facilitate cell culturing practices, microchannel devices were grouped into sets of two and sheltered in 90mm petri-dishes. A small petri-dish of 35mm containing sterilized water was also placed inside each 90mm petri-dish to reduce the local water evaporation.

II. V. II. Focal hypoxia for neuronal culture

Human neurons after 21+ days of culture were subjected to focal hypoxia in the microchannel device. Prior to experiment, the cultures were rinsed and changed to the phenol red-absent N2B27(–). The system set-up is shown in figure 4.8. The Pt/C electrode was tailored to a size of 7mm (l) x 6mm (w). A solder iron was used to create three holes on a 90mm petri-dish, in which the electrode system was first set up by using a spare PDMS microchannel device. The electrodes were semi-fixed with Blu Tack to ensure that the scavenging electrode was at the same height (2mm) between experiments. The scavenging system was then inserted to the central chamber of neuron-containing devices for 25- and 35-minute oxygen scavenging, corresponding to 10- and 20-minute hypoxia (n = 4 for each focal hypoxia condition). After this, the culture medium was immediately changed to fresh N2B27 for 18 hours of incubation in 5% O_2. The positive control had cells incubated in 0% O_2 for 6 hours (3h equilibration + 3h bulk hypoxia) followed by a fresh N2B27 media change and culturing for 18 hours in 5% O_2 (n = 2), whereas the negative control was kept in 5% O_2 (n = 2). At the end of the treatments, 4% PFA was used to fix the cultures for 20 minutes at room temperature. The cultures were rinsed three times with PBS and stored in the fridge until performing immunofluorescent staining.

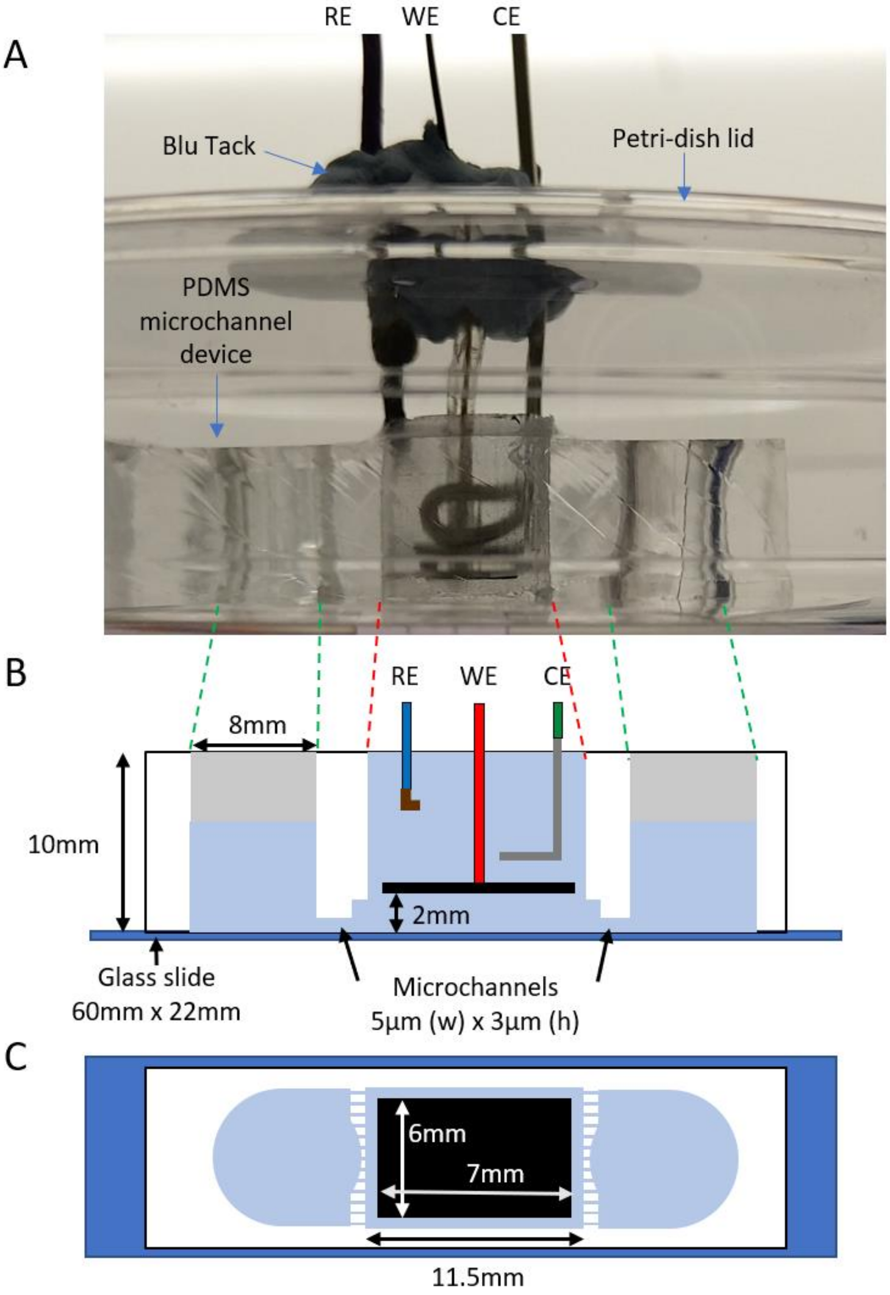

Figure 4.8 A: Focal hypoxia set up in the microchannel device. Red and green dotted lines were used to project the positions of the central and side wells in the schematic below, respectively. B,C: Schematic of the set-up with dimensions. WE: working electrode; RE: reference electrode; CE: counter electrode. The PDMS microchannel device is bonded on the glass slide (blue rectangle). The light blue colour in B indicates the level of medium loaded to each well. Black rectangle in C represents the scavenging electrode.

II. V. III. Immunofluorescent staining

Immunofluorescent staining of neurons was performed to investigate the morphological changes and cell responses to hypoxic stress. Annexin V and TUBB3 were stained in this experiment. Annexin V was stained immediately after fixation before permeabilizing the cells. Rabbit annexin V antibody at a dilution of 1:400 in PBS with 0.5% BSA was used to stain for 16h at 4°C. The cells were then rinsed 3 times with PBS with 0.5% BSA. They were blocked and permeabilized with AFB with triton x 0.1 for 2 hours. Chicken anti-TUBB3 in blocking buffer was diluted 1:1000 in AFB with triton x 0.1 for 16h at 4°C. Anti-rabbit 555 and anti-chicken 488 were used at the dilution of 1:500 in AFB with triton x 0.1 for 2 hours at room temperature. After rinsing 3 times with PBS + triton x 0.1, 300mL of BisBenzidine solution (diluted 1:10,000 in PBS) was added to each compartment for 2 minutes for nucleus staining. The cells were rinsed with PBS + triton x 0.1 for 3 times. The compartments were then topped with PBS to keep them hydrated. The microchannel devices were protected in 90mm petri-dishes sealed with parafilm and stored in the fridge.

II. V. IV. Confocal imaging analysis

Upon imaging with confocal microscopy, three regions were taken per sample per condition. Images were imported to ImageJ for processing and analysis. Since the cell bodies of neurons are small and the cytoplasm is relatively thin, annexin V staining co-localized with the cell nucleus were analysed. Regions of interest were exported for statistical analysis.

II. VI. Statistical analysis

The statistical analysis was performed using R. Comparisons among four groups in the quantitative analysis of annexin V intensity under hypoxia stress were performed using the one-way ANOVA and Tukey's post hoc test was used to analyse the results. Statistical significance was recognised for p values less than 0.05.

III. Results and discussions

III. I. Microchannel device for neuron culture

III. I. I. Characterization of the microchannel device

The surface characterization curves were measured by the stylus profiler to map the thickness of the crosslinked SU-8 photoresist (fig. 4.9). The height of the microchannels was measured as 3.3 ± 0.1μm, in line with the thickness indicated for segregating human neuron cell bodies as reported in the literature.[153] The second layer of SU-8 was measured to be 63 ± 1μm in height. Its purpose was for laying out well-defined surfaces for human cortical neuron culture and ensuring good transitions from the culturing wells to the microchannels. PDMS cast on the silicon wafer master was able to retain the features (fig. 4.7). The compartments were also successfully created by cutting with scalpel and biopsy punch. Notably, PDMS walls, allowing high oxygen exchange, could effectively house the electrode system for setting up the hypoxia gradient. This open-chamber microchannel device could be suitable for compartmentalizing neuron cell body and axons, analogous to the human cortex.

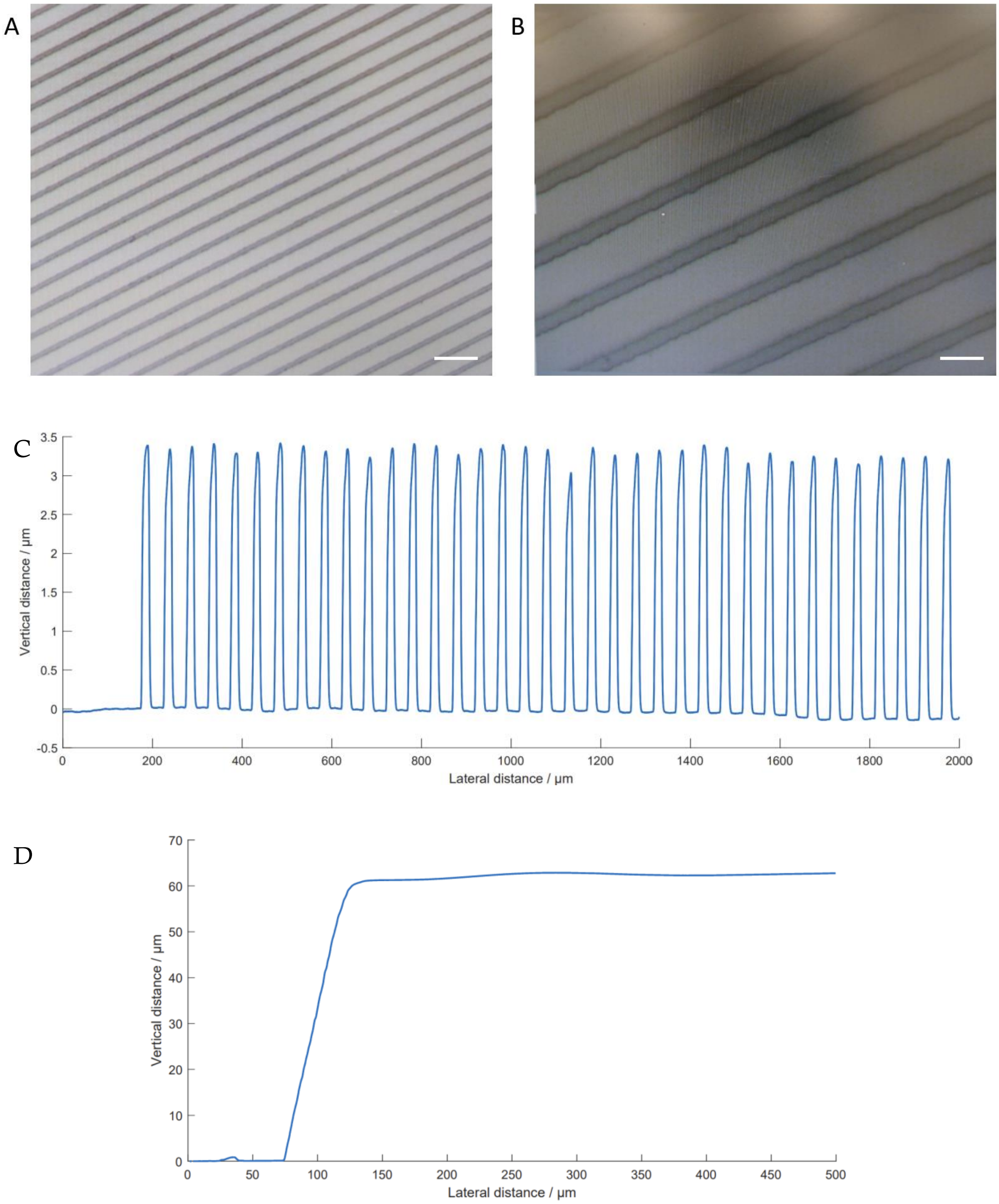

Figure 4.9 Characterization of silicon wafer master for fabricating microchannel device. A,B, Image of the features of the first layer on the silicon wafer. Scale bar: 100µm and 500µm, respectively. C: vertical profile of the microchannels (first layer). D: vertical profile of the culturing wells (second layer).

III. I. II. Human neurons growth in microchannel device

The microchannel device was evaluated by its effectiveness in separating human cortical neuron cell bodies from the axons. Widefield fluorescent images of human cortical neurons, differentiated for 14 days from GFP-expressing neural progenitor cells, showed continuous axon growth (fig. 4.10). The fine openings of the PDMS microchannels restricted the neuron cell bodies from translocation but allowed the axons to pass through into the adjacent chamber. Short axons were observed 2 days after replating. A few axons crossed the channels on day 6 whereas a few were still making their way through. On day 9, some long axons were observed in the adjacent chamber but remained sparse and separated. Axonal bundles were observed on day 14 and an extensive network of axons were observed on day 19. It was not obvious that any neurons passed through the microchannels. This suggested that the channels effectively acted as physical barriers in prohibiting the cell bodies trespassing. Notably, it was promising that the neurons had neurite outgrowth at day 19 and did not show morphological abnormalities despite the reduced exposure to nutrients in a short section of the axon within the microchannels. The growth was more sustainable when neuron conditioned medium was used as the culture medium over N2B27. Such benefits have been observed in multiple studies but the neurotrophic factors have not been fully understood to date.[154,155]

One of the biggest difficulties of this system was guiding the axonal growth at the open central chamber. Advantageous of providing ample nutrients from culture medium and the oxygen scavenging system, the central chamber was lacking proper guiding cues for the axons. Axons tended to turn and bundle up but not venture into the centre, let alone connecting with axons and neurons at the opposite end. Nevertheless, this microchannel device was effective for separating cell bodies and axons for focal hypoxic experiments and allowed the initial hypoxia studies to proceed.

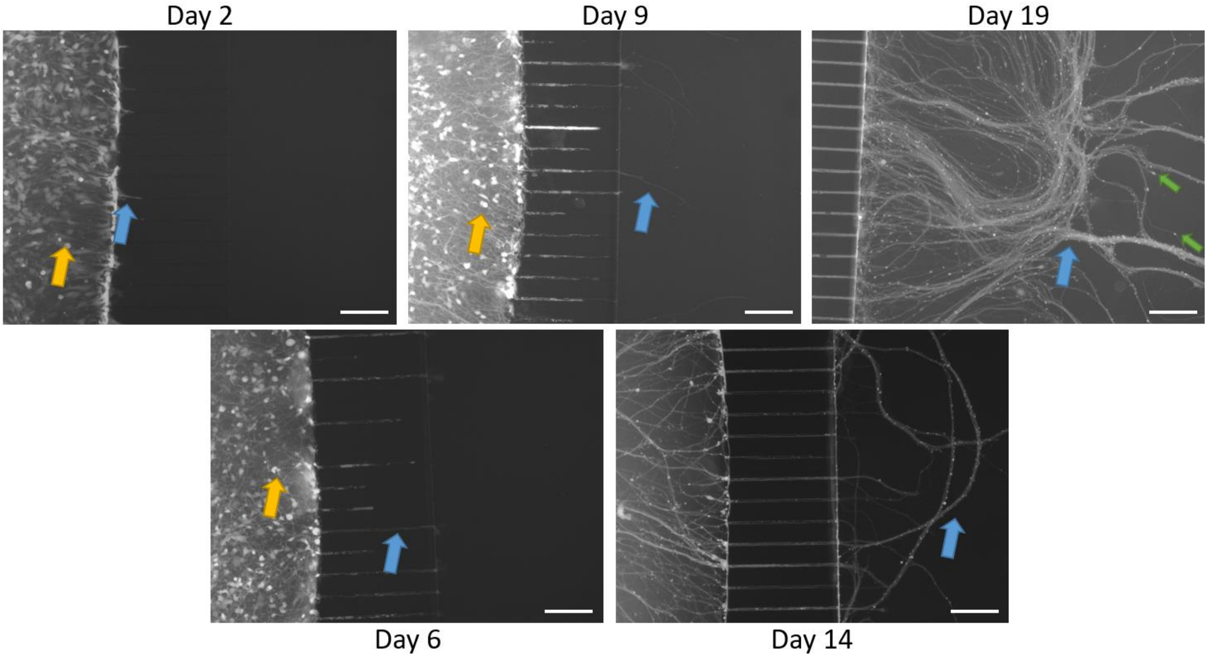

Figure 4.10 Widefield fluorescence microscopic images of human cortical neurons (with auto expressed GFP). Neuron cell bodies: yellow arrows; Axons: blue arrows; Neurites: green arrows. Scale bar: 100µm.

III. II. Focal hypoxia on neurons

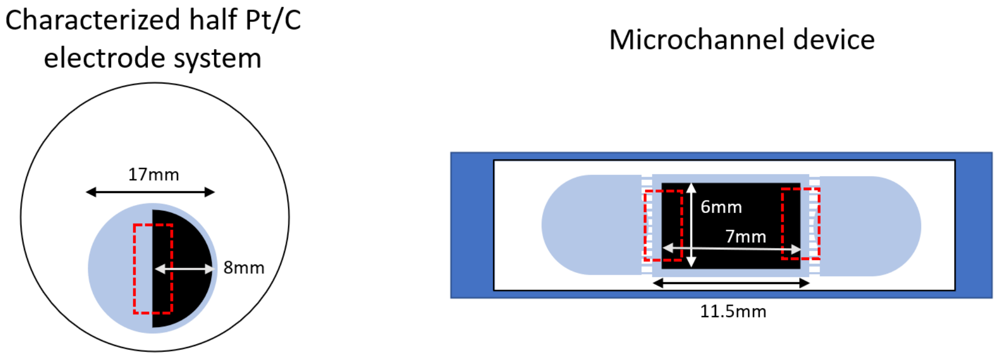

Figure 4.11 Schematic presentation of the assumption of similarity between the boundary (red dotted box) at the half Pt/C electrode system characterized in chapter 2, and that of the microchannel device reported in this chapter. Black area: coverage of the oxygen scavenging electrode; Light blue: electrolyte.

Electrochemical focal hypoxia was applied to the central chamber (see fig. 4.8 for set-up). The Pt/C electrode was cut into 7mm (l) x 6mm (w) to cover the 11.5mm (l) x 8mm (w) rectangular well. The decision of the size was based the characterization results reported in Chapter 2 on the half circle Pt/C electrode (see chapter 2, section III.II.III.IV, and figure 2.37). From figure 2.37, it was shown that the oxygen depleted zone extended to 2-3mm beyond the electrode edge. This local oxygen diffusion boundary was assumed at the boundary at the microchannel device, illustrated with schematics in figure 4.11. The electrode was therefore positioned to limit hypoxia to the central chamber, by maintaining approximately 2mm distance between the oxygen scavenging electrode and the microchannels (fig. 4.12). Based on the characterisation in Chapter 2, steady state O_2 concentration at 10mmHg in the central chamber could be assumed after 15 minutes O_2 scavenging whereas the surrounding remained at normoxia (38mmHg).

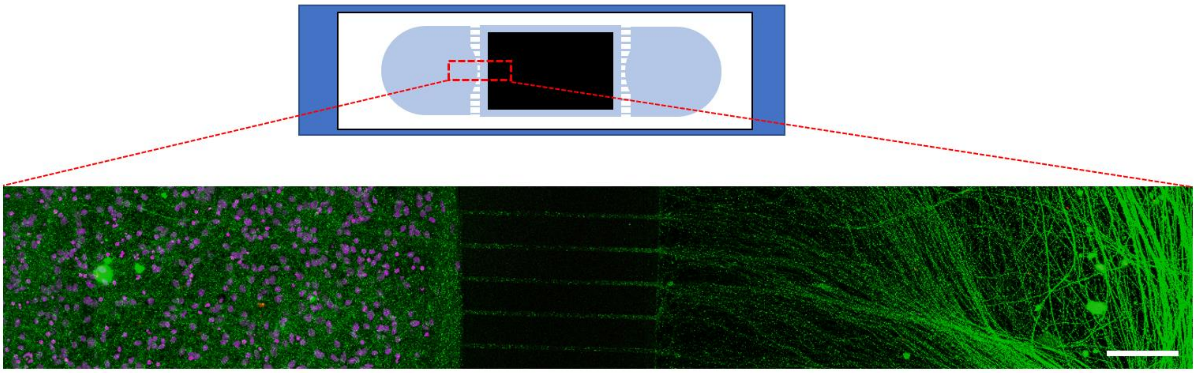

Figure 4.12 Representative tile image of the human neurons growing inside the microchannel device. The PDMS microchannels (5µm) are at the centre of the image, between the black rectangular boxes, allowing neurons on the left to grow axons to the adjacent central chamber. Schematic diagram at the top indicates the imaged region in the box with red dotted outline. Immunofluorescent image colours: Red: annexin V; Blue: nucleus; Green: TUBB3. Scale bar: 100µm.

A representative confocal tile scan of the neuron culture in the microchannel device is shown in figure 4.12. The microchannels show as the line between black rectangular blocks in the centre of the image. It was observed that neuron cell bodies were present in the left-hand chamber in the image, next to the microchannels, but were absent in the adjacent central chamber (right-hand in the image). This is similar to the observations reported in the section 3.1 of this chapter (figure 4.10). In contrast, however, while axon growth was abundant in the cell body chamber, many axons also grew through the microchannels to the neighbouring well. The axons spread on the glass surface and some formed axon bundles, which appeared as thick green lines in the image. It was also observed that the TUBB3 staining had a higher intensity on the right side of the image, despite using the same microscopic settings. This would be consistent with the slow diffusion of antibodies for staining, though this limitation had been foreseen and both antibody staining procedures were extensively prolonged by at least 2-fold of the normal duration needed for coverslips. It is intuitive that diffusion through the microchannels would be limited by the presence of the filling of axons, filling the void space; in the highly magnified image of the channels an intensity gradient, decreasing from both ends of the channels towards the middle can be see, which would be consistent with this hypothesis.

The neuron cell bodies (left hand chamber in image in figure 4.12) were investigated for their morphology and apoptotic response after focal hypoxia by immunofluorescent staining (fig. 4.13). Expectedly, a dense interlinked axon network was formed in the high-density neuron culture in all conditions. Annexin V staining showed significant increase in intensity in all samples with hypoxic stress, focal and bulk. This suggested that the phosphatidylserines at the plasma membrane were exposed at the extracellular side, indicating the induction of apoptosis (schematic of mechanism illustrated in figure 4.14).[156] The quantitative analysis on the annexin V intensity was presented in the boxplot shown in figure 4.15. The results agreed with the observation in the confocal images. All hypoxia treated groups showed statistically significant increase in annexin V against the negative control ($p < 0.01$ for 10min focal hypoxia; $p < 0.001$ for 20min focal hypoxia and 3h bulk hypoxia). 3h bulk hypoxia also expectedly showed significantly higher annexin V intensity than the focal hypoxia groups ($p < 0.001$ for 10min and 20min focal hypoxia). This is consistent with the longer hypoxic stress as compared to the acute focal hypoxic conditions. The difference between the focal hypoxia groups were not statistically significant ($p = 0.248$). These observations suggested that 10-minute focal hypoxia was enough to cause stress to the cells. The nucleus staining did not show nuclear condensation or fragmentation, suggesting any early-stage apoptosis.

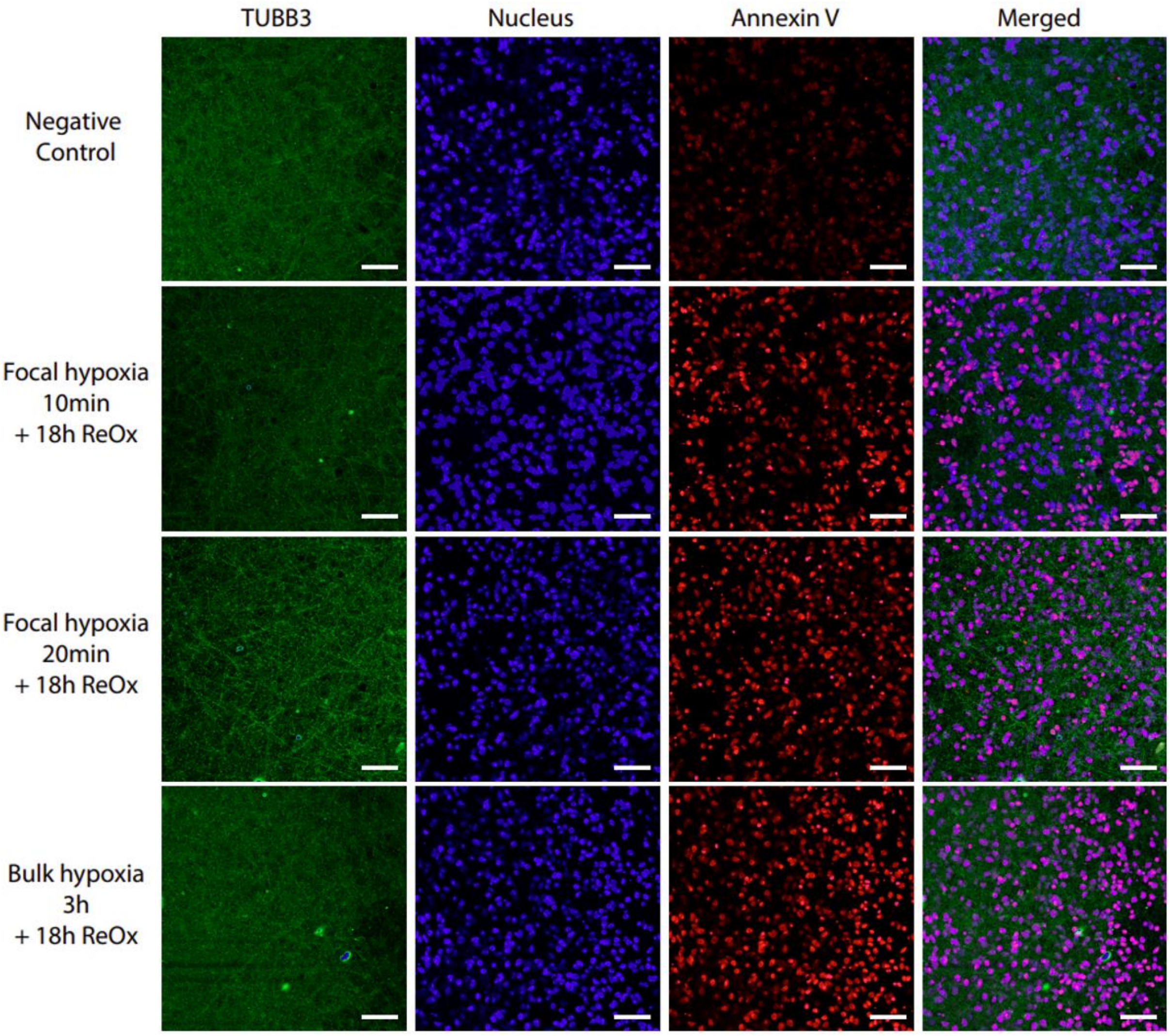

Figure 4.13 Representative confocal images of focal hypoxia and bulk hypoxia on human neurons. Scale bar: 25µm.

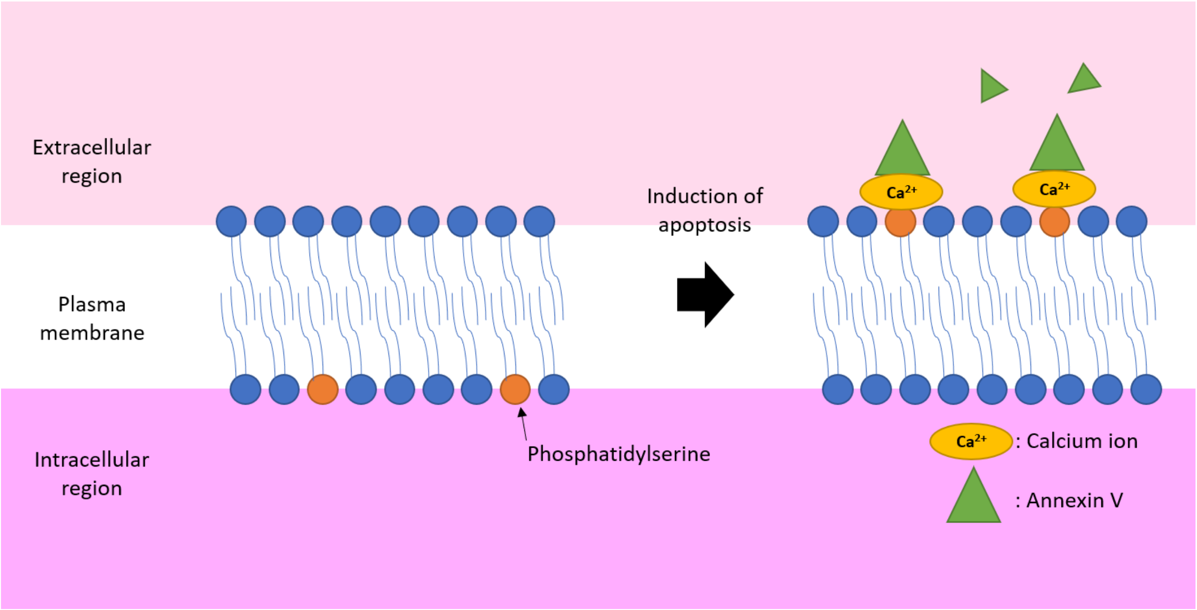

Figure 4.14 Schematic presentation of annexin V binding mechanism under the induction of apoptosis. Negatively charged phosphatidylserine translocated from the intracellular side (purple region) to the extracellular side (pink region) under the induction of apoptosis. With the assistance of calcium ion (Ca^{2+}), annexin V can bind to the cell membrane.[156]

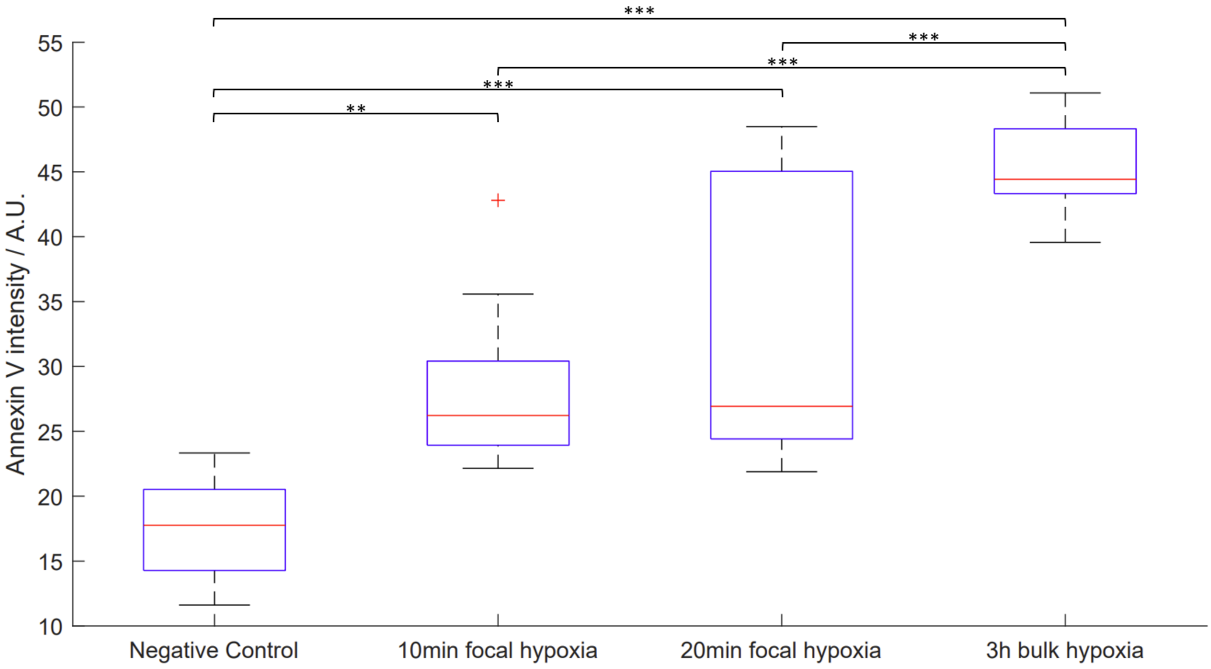

Figure 4.15 Box plot of the annexin V intensity under different conditions of focal hypoxia. Positive control is the bulk hypoxia. Two replications were collected in the negative control and the 3h bulk hypoxia condition, whereas four replications were collected in the 10min focal hypoxia and 20min focal hypoxia conditions. 3 images were analysed for each replication per condition. One-way ANOVA and Tukey's post hoc test was used for statistical analysis. **: $p < 0.01$; ***: $p < 0.001$.

Axons in the central chamber were also analysed with confocal microscopy (fig. 4.16). While significant differences in annexin V intensity was observed in hypoxic stressed neuronal cell body cultures, no obvious differences were observed on the axons. All conditions showed a mixture of intact axons and fragmented axons in the images taken that neither appeared to dominate. The fragmented axons were potentially related to some unhealthy neurons in the cell culture. It is suggested that in future experiments, introducing glial cells, such as astrocytes, along with the existing neuron-conditioned culture medium may improve the viability of the axons.

This experiment has successfully demonstrated for the first time, that focal hypoxia at the axons can affect the viability of human cortical neurons. Despite not incurring fragmentation locally, hypoxic stress experienced at the axons incurred apoptotic responses at the cell nucleus, suggesting that a signal transduction process to the cell nucleus was triggered. One possible mechanism speculated to occur was that HIF-1α stabilized locally at the distal axonal ends dimerizes with

HIF-1β. Even though the heterodimer translocated through oxygen-sufficient cytoplasm, the dimerization prevented hydroxylation and degradation of HIF-1α and permitted the translocation of the transcription factor. Despite not conclusive, this transcription response has become destructive, causing the nuclear condensation. Further investigations in the downstream responses of HIF-1α (e.g. VEGF, glut1, caspase) can provide a more definitive conclusion on the mechanisms involved.

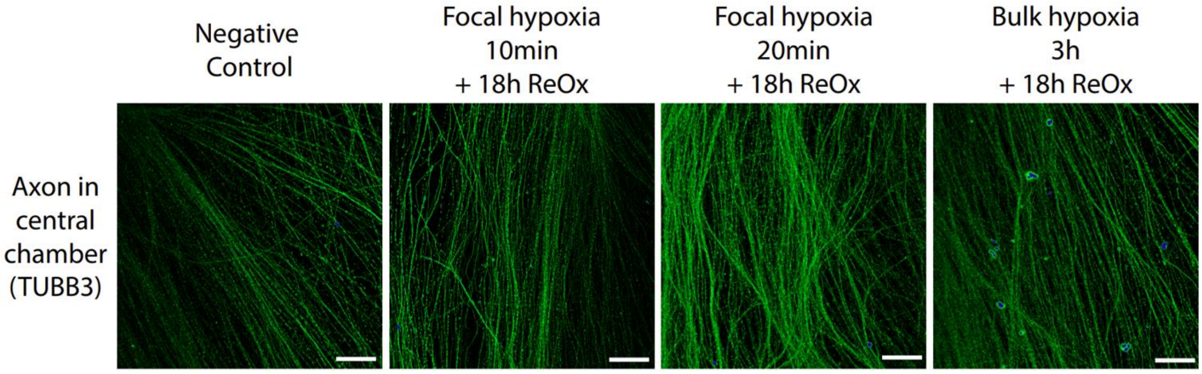

Figure 4.16 Representative confocal images of the axons in the central chamber under different conditions. Scale bar: Scale bar: 25μm.

IV. Conclusions

In this chapter, a human cerebral focal hypoxia model was developed and investigated. Initial results demonstrated that a microchannel system was capable of separating neuron cell bodies and axons, creating a human cortical neuron culture model. Compartmentalization of the neuron cell bodies and axons might be useful in simulating the grey matter and white matter of the brain in which they reside, respectively. The microchannel master created by photolithography was a highly efficient and reproducible platform for the PDMS device fabrication. PDMS has favourable optical properties and interfacial adhesion facilitating effective bonding.[157,158] Oxygen permeability of PDMS was also beneficial to the generation of an oxygen gradient.

Fine channel openings of 5µm x 3µm were created by permanent binding of the PDMS device to a glass coverslip. The PDMS walls acted as physical barriers and were proven to restrict the relatively larger cell bodies of human cortical neurons from translocating through the channels, whereas the axons were able to grow through to the central compartment. Axons were observed to pass through the microchannels shortly after two days of replating and reached a good density for experiments after culturing for approximately 3 weeks.

Another important feature of the design over conventional microfluidics is the open-well chambers. These chambers were particularly useful for fitting the oxygen scavenging system by simple insertion. This allowed conventional electrode cleaning and pre-treatments for the oxygen scavenging. This also minimized the use of tubing in microfluidic systems and thus the risk of media leaks and contamination. The generation of a pressure gradient was also made simple by varying the media height in different wells. With a higher media height at the central chamber, the constant outflow could assist deterring cells from translocating through the microchannels.

The human cerebral focal hypoxia model revealed that focal hypoxia on the axons can impact the viability of the cells. Upon applying focal hypoxia to the axons of human cortical neurons, the induction of apoptosis was observed in as short as 10 minutes. The observations of intact cell nucleus and minor axon fragmentation suggested that apoptosis was at the early stage. The fact that apoptotic response was detected at the opposite end of the cell-body chamber also suggested that a sensing and signal mechanism was involved in response to acute focal hypoxic stress. While the mechanism has not been investigated herein due to the rapid degradation of HIF after reoxygenation, it is speculated that HIF-1 might be the key regulator of the mechanism. Nevertheless, this experiment successfully demonstrated the impact of focal hypoxia to the human cortical neurons.

Chapter 5: Summary and future work

I. Summary

Research in focal hypoxia has revealed its involvement in physiological and pathophysiological phenomenon. Hypoxia plays a pivotal role in the developmental stage and can be triggered during daily activities whereas pathological focal hypoxia has been widely reported in diseases and is known to affect disease prognosis and pharmocokinetics. The hypoxic core of tumour cell masses has strong resistance to chemotherapy and radiotherapy, impacting disease prognosis and therapeutic strategy. On the other hand, focal hypoxia from microinfarcts in the human brain is speculated to cause neurological disorders such as dementia.

There is an immediate need for research in the impact of focal hypoxia but is challenged by the lack of appropriate and translatable focal hypoxia model. Common hypoxia models are the animal models and the *in vitro* cell models. While animal models are suitable for investigating how organs and the organism respond to hypoxic insults, the methods for inducing hypoxia are global (such as hypoxia chambers) and/or invasive (such as surgical occlusions). The underlying differences between species also reduce the translatability of the discoveries of mechanisms to human beings. As a result, *in vitro* cell models are attractive alternatives for researchers to investigate cellular and molecular interactions. The main approaches to create hypoxia were the chemical induction, enzymatic scavenging, the premixed gas equilibration, and the perfusion of equilibrated media. Yet, these approaches lack translatability to focal hypoxia due to the absence of oxygen gradient, chemical toxicity, and the slow diffusion of oxygen. Microfluidic devices have been developed to resolve some of the problems but are complicated to develop and are not biologist-friendly for studies. This thesis addressed the need in creating a biologically applicable focal hypoxia cell model for research in diseases and investigated the use of electrochemical oxygen scavenging for creating a focal hypoxia system, applying to a human cortical neuron model as the proof-of-concept.

Platinum / graphite (Pt/C) was selected to be an ideal material of for oxygen scavenging based on my previous work. High exchange current density and catalytic activity for the oxygen reduction reaction are beneficial to the oxygen scavenging in culture media. Pt/C was sintered on the Gore

membrane that provides structural support, flexibility, and oxygen permeability in all dimensions. This facilitates electrode reshaping and further electrode designs. Large electrochemical window of this material was advantageous to the oxygen reduction reaction occurring in both PBKCl and the culture medium, N2B27(–). This significant cathodic shift compared to Pt is attributed to the high amount of graphite in the mixture, causing an increase in surface energy required to adsorb oxygen.

The analysis of the oxygen reduction reaction on Pt/C showed chemical irreversibility and electrochemical quasi-irreversibility. They were evident by the absence of reverse anodic peak and the cathodic peak shift as scan rates increased. The kinetic analysis of oxygen reduction reaction by Tafel plot showed two Tafel slopes in both PBKCl and N2B27(–), suggesting a change in rate determining factor at lower potential, potentially due to the surface composition change from Pt/PtO to reduced Pt. The slopes in the former were 277mV/Dec and 601mV/Dec whereas the ones in the latter were 232mV/Dec and 492mV/Dec. The respective exchange current densities were –5.90 and –5.34, and –6.11 and –5.40. The significantly slow kinetics compared with Pt was due to the low platinum content in the material but should not affect its application by polarizing at the diffusion-controlled cathodic potential.

Pt/C had a large electrochemical active surface area. Calculated from the Randles-Sevcik equation, the electrochemical active surface areas were 5.97 cm^2 and 5.19 cm^2 in PBKCl and N2B27(-), respectively, three-fold of the geometric surface area. This observation was proven to relate to the rough surface of the material, observed in the SEM micrographs. BET surface area analysis further supported the observation. Pt/C had a BET surface area of 52.9m^2/g that is significantly larger than the literature values of mesoporous Pt and polycrystalline Pt.

Pt/C showed ideal oxygen scavenging characteristics. The oxygen scavenging system was fitted into the electrochemical cell and created a spatiotemporally advanced oxygen gradient environment. The electrochemical oxygen scavenging required only 7 minutes to drop the oxygen concentration at the base of the culture well from 159mmHg (20.9%) to 38mmHg (5%). The outstanding performance of the scavenging system was marked by needing only 6 minutes to reach

11mmHg (1.5%) O_2 from physiological oxygen level. In aerated medium, 13 minutes and 18 minutes were needed to reach 11mmHg (1.5%) and 4mmHg (0.5%) O_2, respectively, which are hypoxic to human cells. The oxygen gradient could also be adjusted based on the vertical height, position, and size of the oxygen scavenging electrode.

The key factor of a successful focal hypoxia model is defined by its ability in inducing the expected hypoxia response on the cells. The electrochemical oxygen scavenging system, proven to reduce local oxygen concentration in the electrochemical cell, was applied to human neural progenitor cells. HIF-1α transcription factor expectedly increased in intensity after 20 minutes and plateaued after 3 hours of hypoxic stress. This demonstrated that hypoxic stress was induced rapidly, and the steady-state hypoxia could be maintained over time. Spatially patterned hypoxia could also be tailored by modifying the geometry of the scavenging electrode to create pre-set oxygen gradient in the culture. Patterned HIF-1α responses of neural progenitor cells was induced, similar to the pattern characterized by the Clark electrode array. The electrochemical hypoxia was proven to be effective in triggering expected cellular hypoxia responses to the neural progenitor cells. It also successfully demonstrated the apoptotic impact of bulk hypoxia to human cortical neurons, inspiring more in-depth investigation by developing a focal hypoxia cerebral model.

Having proven the effectiveness of generating focal hypoxia on human neural progenitor cells, the oxygen scavenging system was used to investigate the impact of focal hypoxia to human cortical neurons. While human cortical neurons were reported and proved in the thesis to be more vulnerable to hypoxia, a human cerebral model was developed to simulate the separation of grey matter and white matter in the brain and the impact of hypoxia in the white matter was investigated. This was achieved by creating a microchannel device with fine channel openings of 5µm x 3µm. PDMS walls acted as physical barriers to the relatively larger cell bodies of the neurons and thus separating them from the axons. The adoption of open-well chambers and the usage of PDMS as the device material were beneficial to the generation of an oxygen gradient with the electrochemical scavenging system. It was discovered that focal hypoxia on the axons were able to affect the viability of the neurons. Focal hypoxia for 10 minutes caused the induction of apoptosis in the human cortical neurons, indicated by the increase in phosphatidylserine on the surface of the cells. Intact cell nucleus and minor axon fragmentation suggested an early-stage apoptosis. This successful combination of the electrochemical oxygen scavenging system to the human brain microchannel system was the first to demonstrate how hypoxic stress responses could be transmitted to the cell nucleus and triggered downstream apoptotic response.

II. Planned future work and supporting preliminary data

II. I. Improvements to the human cerebral model

II. I. I. Surface patterning for axonal guidance

One imperfection observed in the microchannel system is the limited axon extension in the central compartment. To direct the axons to grow further, the microchannel system could be further improved with surface patterning in parallel to the microchannels. Alternating zones of cytophilic and cytophobic surfaces can guide the axonal growth. Preliminary experiments investigated Pluronic F127 glass surface modification and showed reasonable success in tailoring axon growth (Details of the experimental set-ups are documented in the Appendix I).

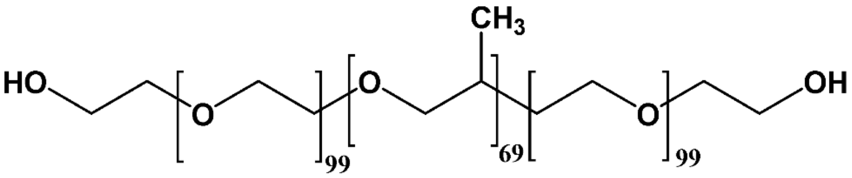

Figure 5.1 Molecular structure of Pluronic F127. A trimer of 12500 molecular weight with poly(ethylene oxide):poly(propylene oxide) at 2:1 ratio. Image courtesy of Donato *et al.*, 2020.[159]

The silanization of a hydrophobic silane, PFDTS, to the glass surface was optimized to modify the hydrophilic glass surfaces for Pluronic F127 adsorption (fig. 5.2). Results concluded that silanization above 30 minutes was needed for developing a hydrophobic surface. Pluronic F127 coating on the PFDTS was then optimized. It was observed that 1% Pluronic F127 in PBS was the most effective in preventing human cortical neuron adhesion (fig. 5.3 and fig. 5.4).

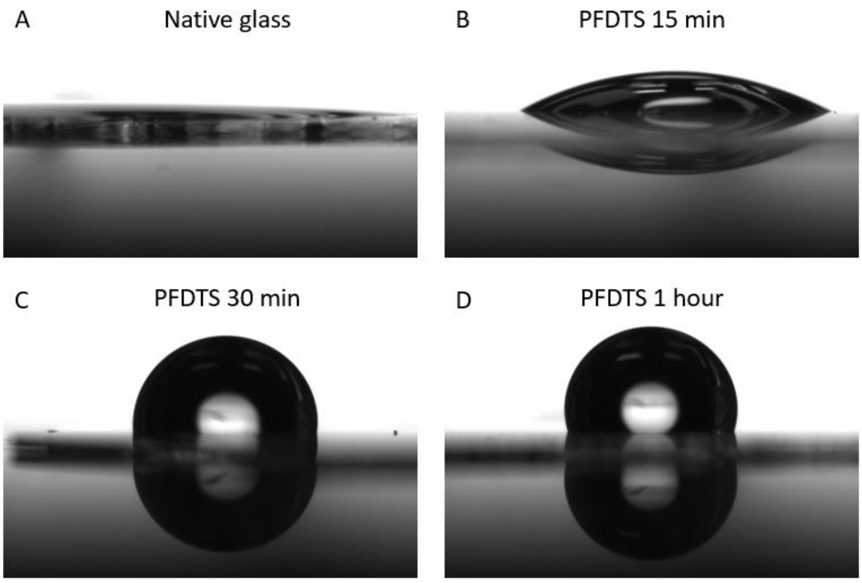

Figure 5.2 Static water contact angle measurements on glass treated with different treatment conditions of PFDTS.

Silanization duration (n = 3) (+ 1h curing @ 40°C)	Contact angle (°) (mean ± SEM)
Negative Control	6.0 ± 0.5
15 minutes	28.1 ± 2.9
30 minutes	102.7 ± 1.5
1 hour	103.3 ± 2.9

Table 5.1 Summary of contact angles measured on PFDTS modified glass (n = 3).

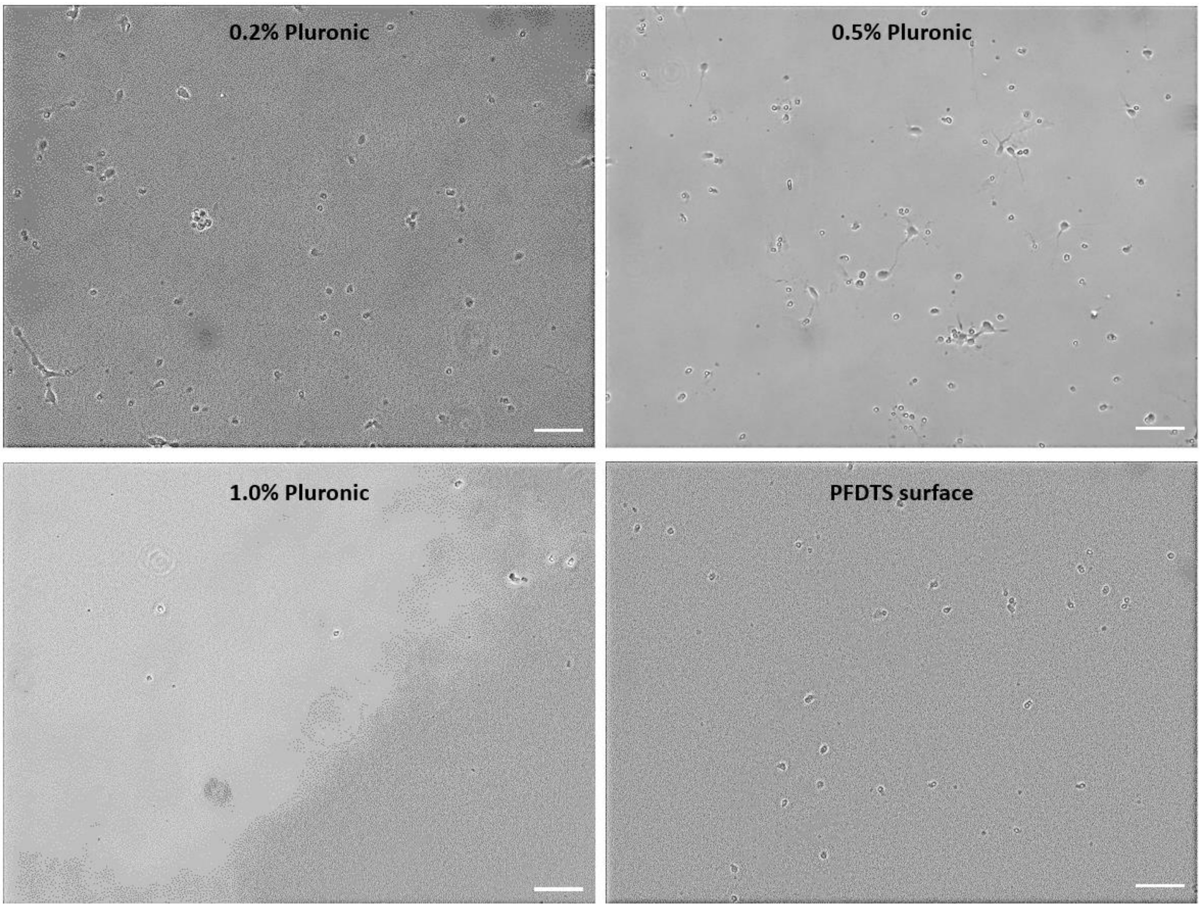

Figure 5.3 Widefield microscopic images of human cortical neurons cultured on PFDTS-glass with different Pluronic F127 treatment concentrations. Image taken 6 days after plating. Scale bar: 100µm.

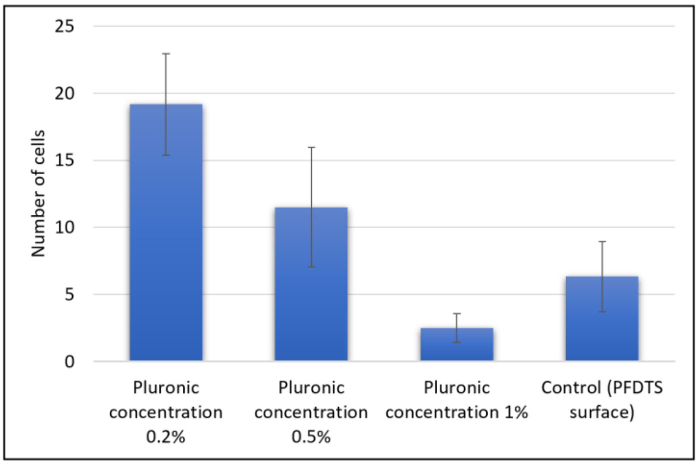

Figure 5.4 Quantitative analysis of flat cells on the F127-PFDTS-glass under different treatments. (n = 6)

Four surface patterning protocols were investigated, and the schematic presentations are shown in figure 5.5. Human cortical neurons were plated onto the treated surfaces for analysing the patterning efficiency (fig. 5.6). Method 1, which did not contain Pluronic F127, showed no obvious patterning of cell adhesion on the PFDTS-glass. Method 2 had Pluronic F127 coated before the oxygen plasma and bulk coating of PDL and laminin. Cell adhesion was indiscriminately observed at all surfaces without inhabitable zones. Method 3 and 4 had the PDMS stamp attached to the surface when coating PDL + laminin, and only PDL, respectively. It was evident that only Method 3 showed success in creating inhabitable zones as intended. Retaining the physical presence of the PDMS stamp during the PDL and laminin coating stages was effective in blocking amino acids and proteins, wherein other methods the substrates could electrostatically bind to the surfaces. More detailed widefield microscopy of glass prepared by method 3 showed neurons growing along the edges of a PDMS block and following microchannels on the PDMS stamp (fig. 5.7). It was however observed that after 3 weeks of culturing, axons did not extend much further along the pattern. It was speculated that the PDL and laminin did not coat the entire channel due to the restricted diffusion imposed by the PDMS stamp.

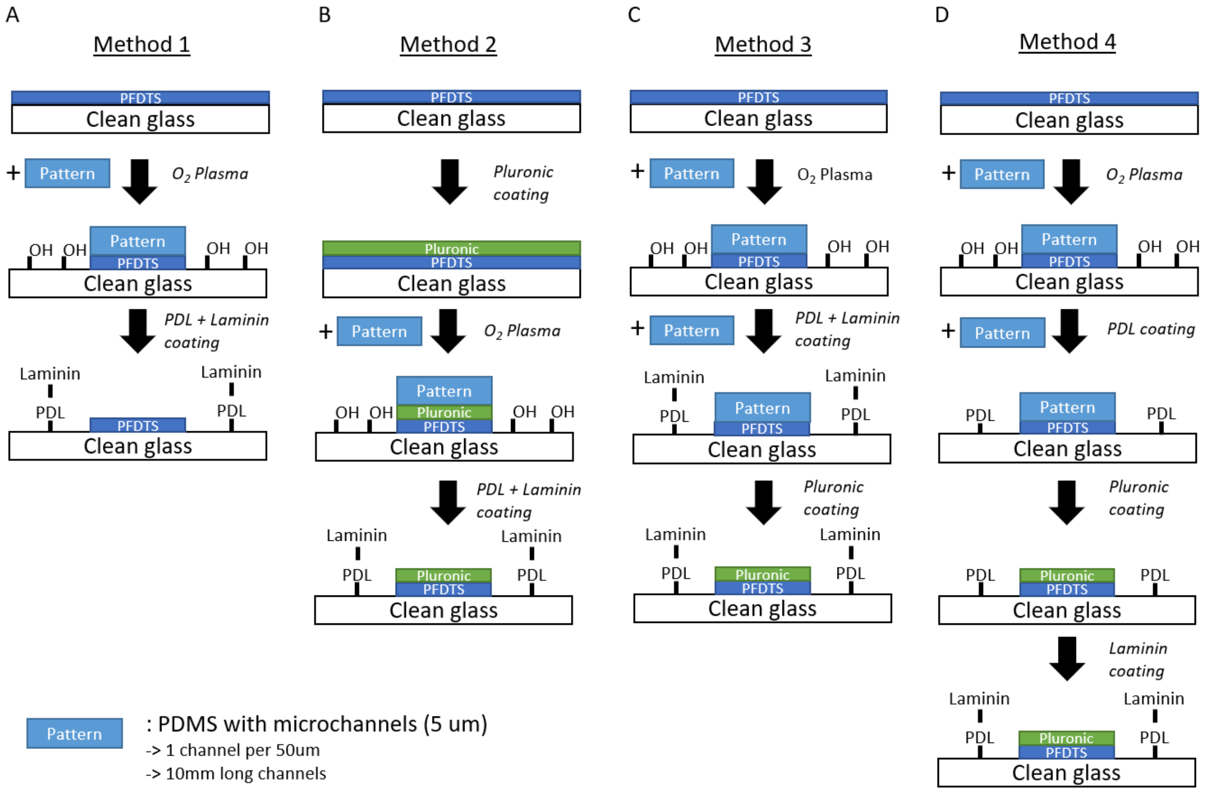

Figure 5.5 Schematic diagram of the protocols used for surface patterning.

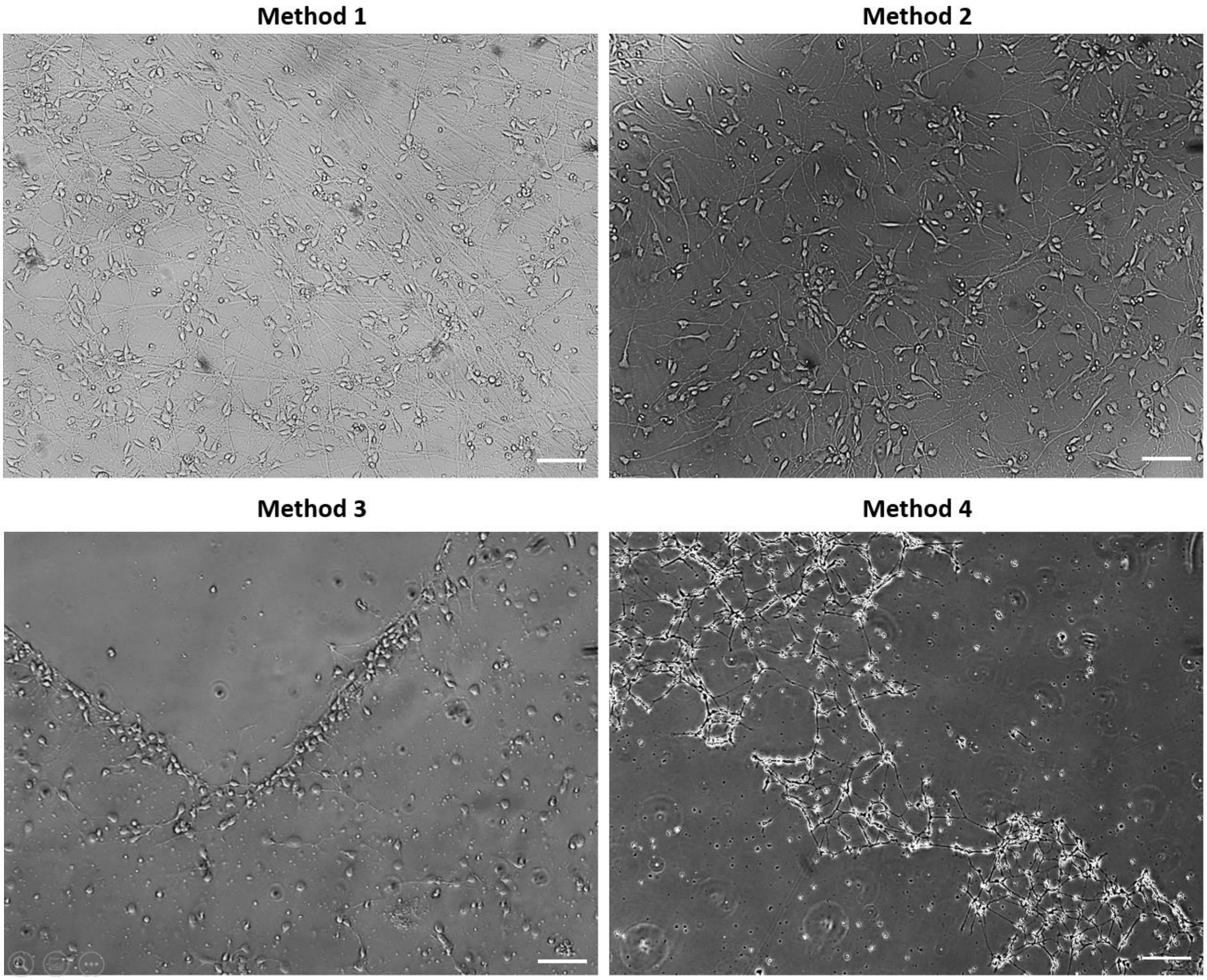

Figure 5.6 Widefield microscopic images of human cortical neurons cultured on the patterned glass surfaces for 24 hours with different protocols. Image taken at the zone of patterning. Scale bars: 100μm.

Fluorescence-tagged protein PLL-FITC was used to investigate the diffusion of substrates along the microchannels in Method 3. Widefield microscopic fluorescent images showed the adhesion of PLL-FITC on the glass surfaces along the microchannels (fig. 5.7). PLL-FITC travelled 102.38 ± 3.74μm, 174.21 ± 8.24μm and 565.65 ± 21.81μm after 1.5h, 3.5h and 72h of incubating at 37°C. While the length of grooves is 1cm, it was obvious that diffusion-driven coating with this PDMS stamp would require significantly long period of time for completion. It is thus deemed not feasible as days of incubation at 37°C increases the risk of protein denaturing, solution evaporation and contamination.

Further investigations should focus on improving the coating efficiency by (1) increasing the height of grooves in the PDMS stamp, which were 3µm in height, (2) forcing the coating substrate to flow along the channels by pressure or force, and (3) segment the stamp or shorten the size of the central chamber.

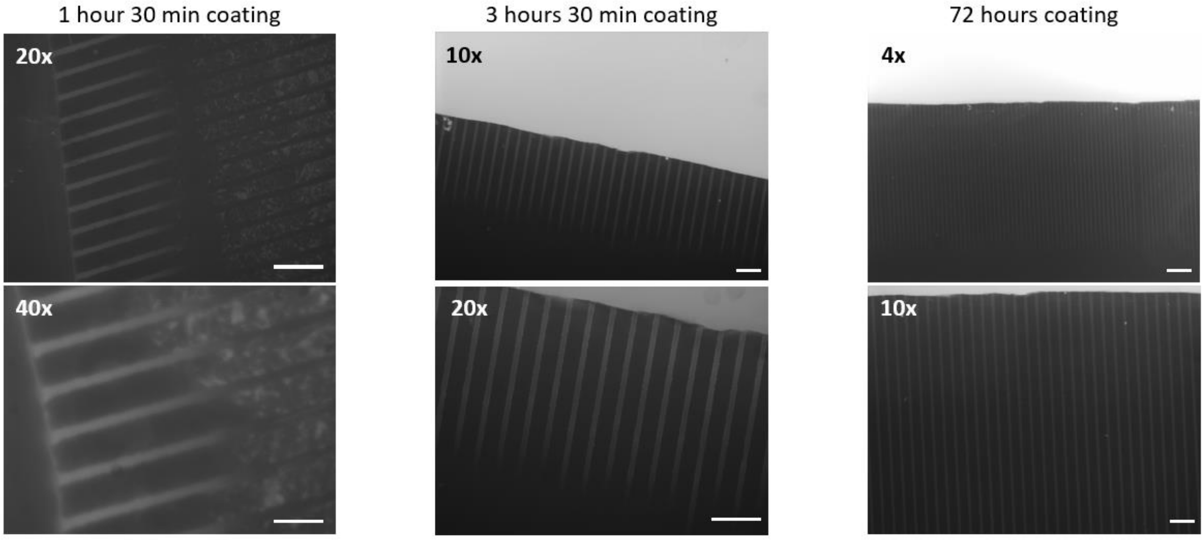

Figure 5.7 Widefield fluorescent images of FITC-PLL diffusing into the microchannels. Distances travelled were measured as 102.38 ± 3.74µm, 174.21 ± 8.24µm and 565.65 ± 21.81µm at 1.5h, 3.5h and 72h, respectively. Scale bars at magnifications 4x: 250µm; 10x: 100µm; 20x: 100µm; 40x: 50µm.

II. I. II. Oxygen-related neurological diseases

The microchannel focal hypoxia system can be further applied to investigate other types of oxygen-related neurological diseases. While acute focal hypoxia was modelled in this thesis, the system could be applied to other hypoxia research such as chronic focal hypoxia and intermittent focal hypoxia with reperfusions. Hyperoxia with focal normoxia / hypoxia regions could also be modelled by changing the ambient oxygen concentration. Upstream and downstream mechanisms could be easily monitored with live imaging by the appropriate reporters.

Co-culturing with other cell types would further our understanding of cellular interactions under focal hypoxia. Glial cells abundant in the human brain have been reported to assist action potential transmission along the axons (e.g. astrocytes and oligodendrocytes) and the synaptic activity (e.g. astrocytes). Further investigation should include astrocytes and/or oligodendrocytes to understand the responses and viability of neurons during and after hypoxic stress. The response of immune cells (e.g. macrophage and microglia) to focal hypoxia could also be investigated easily with the current system.

II. II. Modelling oxygen concentration in the media

While the hypoxia conditions were optimized for human cells in this study, the conditions of media and the time needed to reach hypoxia would differ slightly for different cell types. This is due to differences in oxygen consumption rates among cell types have been reported to vary significantly in the literature.[160,161] It is thus important to develop a computer model to predict oxygen concentration experienced by each culture under specific oxygen scavenging set-up. This would minimize cost (resources and time) needed for developing a translatable hypoxia model for studying cellular and molecular mechanisms.

II. III. Application to other hypoxia models

The electrochemical focal hypoxia system also has strong potential for advancing the studies of other hypoxic events. Chronic focal hypoxia plays a major role in tumour prognosis and pharmacokinetics. A tailored hypoxia model, similar to the proof-of-concept model presented in chapter 3, should be beneficial to the investigation of cell-cell interaction of cancerous cells, or with normal cells. The efficacy studies and screening of drugs could also benefit from the research model. Studies of other hypoxic events such as embryo development, chronic kidney diseases and cardiovascular diseases could adopt the electrochemical system developed.

Chapter 6: Bibliography

1. Sharp, F. R. & Bernaudin, M. HIF1 and oxygen sensing in the brain. *Nat. Rev. Neurosci.* **5**, 437–448 (2004).
2. Mik, E. G. *et al.* Mitochondrial PO 2 measured by delayed fluorescence of endogenous protoporphyrin IX. *Nat. Methods* **3**, 939–945 (2006).
3. Semenza, G. L. Hydroxylation of HIF-1: Oxygen Sensing at the Molecular Level. *Physiology* **19**, 176–182 (2004).
4. Pavlacky, J. & Polak, J. Technical Feasibility and Physiological Relevance of Hypoxic Cell Culture Models. *Front. Endocrinol.* **11**, (2020).
5. Favier, F. B., Britto, F. A., Freyssenet, D. G., Bigard, X. A. & Benoit, H. HIF-1-driven skeletal muscle adaptations to chronic hypoxia: molecular insights into muscle physiology. *Cell. Mol. Life Sci.* **72**, 4681–4696 (2015).
6. Wang, Z., Oppegard, S. C., Eddington, D. T. & Cheng, J. Effect of localized hypoxia on Drosophila embryo development. *PLoS ONE* **12**, (2017).
7. Wagegg, M. *et al.* Hypoxia Promotes Osteogenesis but Suppresses Adipogenesis of Human Mesenchymal Stromal Cells in a Hypoxia-Inducible Factor-1 Dependent Manner. *PLOS ONE* **7**, e46483 (2012).
8. Brezis, M. & Rosen, S. Hypoxia of the Renal Medulla — Its Implications for Disease. *N. Engl. J. Med.* **332**, 647–655 (1995).
9. Keith, B. & Simon, M. C. Hypoxia-Inducible Factors, Stem Cells, and Cancer. *Cell* **129**, 465–472 (2007).
10. Parmar, K., Mauch, P., Vergilio, J.-A., Sackstein, R. & Down, J. D. Distribution of hematopoietic stem cells in the bone marrow according to regional hypoxia. *Proc. Natl. Acad. Sci.* **104**, 5431–5436 (2007).
11. Yoshida, Y., Takahashi, K., Okita, K., Ichisaka, T. & Yamanaka, S. Hypoxia Enhances the Generation of Induced Pluripotent Stem Cells. *Cell Stem Cell* **5**, 237–241 (2009).

12. Deldicque, L. & Francaux, M. Acute vs chronic hypoxia: what are the consequences for skeletal muscle mass? *Cell. Mol. Exerc. Physiol.* **2**, e5 (2013).
13. Ferdinand, P. & Roffe, C. Hypoxia after stroke: a review of experimental and clinical evidence. *Exp. Transl. Stroke Med.* **8**, 9 (2016).
14. Giordano, F. J. Oxygen, oxidative stress, hypoxia, and heart failure. *J. Clin. Invest.* **115**, 500–508 (2005).
15. Harris, A. L. Hypoxia — a key regulatory factor in tumour growth. *Nat. Rev. Cancer* **2**, 38 (2002).
16. Zhang, X. & Le, W. Pathological role of hypoxia in Alzheimer's disease. *Exp. Neurol.* **223**, 299–303 (2010).
17. Sun, X. *et al.* Hypoxia facilitates Alzheimer's disease pathogenesis by up-regulating BACE1 gene expression. *Proc. Natl. Acad. Sci.* **103**, 18727–18732 (2006).
18. Grammas, P., Tripathy, D., Sanchez, A., Yin, X. & Luo, J. Brain microvasculature and hypoxia-related proteins in Alzheimer's disease. *Int. J. Clin. Exp. Pathol.* **4**, 616–627 (2011).
19. Nath, B. & Szabo, G. Hypoxia and hypoxia inducible factors: Diverse roles in liver diseases. *Hepatology* **55**, 622–633 (2012).
20. Taylor, C. T. Hypoxia in the Gut. *Cell. Mol. Gastroenterol. Hepatol.* **5**, 61–62 (2017).
21. Ke, Q. & Costa, M. Hypoxia-Inducible Factor-1 (HIF-1). *Mol. Pharmacol.* **70**, 1469–1480 (2006).
22. Brahimi-Horn, C. & Pouysségur, J. The role of the hypoxia-inducible factor in tumor metabolism growth and invasion. *Bull. Cancer (Paris)* **93**, 10073–10080 (2006).
23. Semenza, G. L. *et al.* Structural and functional analysis of hypoxia-inducible factor 1. *Kidney Int.* **51**, 553–555 (1997).
24. Chan, D. A., Sutphin, P. D., Yen, S.-E. & Giaccia, A. J. Coordinate Regulation of the Oxygen-Dependent Degradation Domains of Hypoxia-Inducible Factor 1α. *Mol. Cell. Biol.* **25**, 6415–6426 (2005).
25. Kibel, A., Iliopoulos, O., DeCaprio, J. A. & Kaelin, W. G. Binding of the von Hippel-Lindau tumor suppressor protein to Elongin B and C. *Science* **269**, 1444–1446 (1995).

26. Semenza, G. L. Hypoxia-inducible factor 1: oxygen homeostasis and disease pathophysiology. *Trends Mol. Med.* **7**, 345–350 (2001).
27. Carmeliet, P. *et al.* Role of HIF-1α in hypoxia-mediated apoptosis, cell proliferation and tumour angiogenesis. *Nature* **394**, 485–490 (1998).
28. Ryan, H. E., Lo, J. & Johnson, R. S. HIF-1 alpha is required for solid tumor formation and embryonic vascularization. *EMBO J.* **17**, 3005–3015 (1998).
29. Chen, C., Pore, N., Behrooz, A., Ismail-Beigi, F. & Maity, A. Regulation of glut1 mRNA by Hypoxia-inducible Factor-1 INTERACTION BETWEEN H-ras AND HYPOXIA. *J. Biol. Chem.* **276**, 9519–9525 (2001).
30. Vande Velde, C. *et al.* BNIP3 and Genetic Control of Necrosis-Like Cell Death through the Mitochondrial Permeability Transition Pore. *Mol. Cell. Biol.* **20**, 5454–5468 (2000).
31. Suzuki, H., Tomida, A. & Tsuruo, T. Dephosphorylated hypoxia-inducible factor 1α as a mediator of p53-dependent apoptosis during hypoxia. *Oncogene* **20**, 5779–5788 (2001).
32. Bourdillon, N. *et al.* Acute and chronic changes in baroreflex sensitivity in hypobaric vs. normobaric hypoxia. *Eur. J. Appl. Physiol.* **117**, 2401–2407 (2017).
33. Mohyeldin, A., Garzón-Muvdi, T. & Quiñones-Hinojosa, A. Oxygen in Stem Cell Biology: A Critical Component of the Stem Cell Niche. *Cell Stem Cell* **7**, 150–161 (2010).
34. Panchision, D. M. The role of oxygen in regulating neural stem cells in development and disease. *J. Cell. Physiol.* **220**, 562–568 (2009).
35. Crossley, D. A. & Altimiras, J. Cardiovascular development in embryos of the American alligator Alligator mississippiensis: effects of chronic and acute hypoxia. *J. Exp. Biol.* **208**, 31–39 (2005).
36. Tomita, S. *et al.* Defective Brain Development in Mice Lacking the Hif-1α Gene in Neural Cells. *Mol. Cell. Biol.* **23**, 6739–6749 (2003).
37. Bayer, C., Shi, K., Astner, S. T., Maftei, C.-A. & Vaupel, P. Acute Versus Chronic Hypoxia: Why a Simplified Classification is Simply Not Enough. *Int. J. Radiat. Oncol. Biol. Phys.* **80**, 965–968 (2011).

38. Li, D., Shao, Z., Hoek, T. L. V. & Brorson, J. R. Reperfusion accelerates acute neuronal death induced by simulated ischemia. *Exp. Neurol.* **206**, 280–287 (2007).

39. Ling, C. K. and E. A. Blood Brain Barrier in Hypoxic-Ischemic Conditions. *Current Neurovascular Research* vol. 5 71–81 https://www.eurekaselect.com/66418/article (2008).

40. Fletcher, E. C. An animal model of the relationship between systemic hypertension and repetitive episodic hypoxia as seen in sleep apnoea. *J. Sleep Res.* **4**, 71–77 (1995).

41. Spaite, D. W. *et al.* The Effect of Combined Out-of-Hospital Hypotension and Hypoxia on Mortality in Major Traumatic Brain Injury. *Ann. Emerg. Med.* **69**, 62–72 (2017).

42. Gibson, G. E., Pulsinelli, W., Blass, J. P. & Duffy, T. E. Brain dysfunction in mild to moderate hypoxia. *Am. J. Med.* **70**, 1247–1254 (1981).

43. Clarke, D. D. & Sokoloff, L. Circulation and Energy Metabolism of the Brain. *Basic Neurochem. Mol. Cell. Med. Asp. 6th Ed.* (1999).

44. Bolaños, J. P. & Almeida, A. Roles of nitric oxide in brain hypoxia-ischemia. *Biochim. Biophys. Acta BBA - Bioenerg.* **1411**, 415–436 (1999).

45. Schmidt-Kastner, R. & Freund, T. F. Selective vulnerability of the hippocampus in brain ischemia. *Neuroscience* **40**, 599–636 (1991).

46. Peña, F. & Ramirez, J.-M. Hypoxia-Induced Changes in Neuronal Network Properties. *Mol. Neurobiol.* **32**, 251–284 (2005).

47. Kirst, C. *et al.* Mapping the Fine-Scale Organization and Plasticity of the Brain Vasculature. *Cell* **180**, 780-795.e25 (2020).

48. Semenza, G. L. Defining the role of hypoxia-inducible factor 1 in cancer biology and therapeutics. *Oncogene N. Y.* **29**, 625–34 (2010).

49. Carmeliet, P. & Jain, R. K. Angiogenesis in cancer and other diseases. *Nature* **407**, 249–257 (2000).

50. Science, A. A. for the A. of. News of Science. *Science* **125**, 18–22 (1957).

51. Moeller, B. J., Richardson, R. A. & Dewhirst, M. W. Hypoxia and radiotherapy: opportunities for improved outcomes in cancer treatment. *Cancer Metastasis Rev.* **26**, 241–248 (2007).

52. Deschner, E. E. & Gray, L. H. Influence of Oxygen Tension on X-Ray-Induced Chromosomal Damage in Ehrlich Ascites Tumor Cells Irradiated in Vitro and in Vivo. *Radiat. Res.* **11**, 115–146 (1959).
53. Gray, L. H., Conger, A. D., Ebert, M., Hornsey, S. & Scott, O. C. A. The Concentration of Oxygen Dissolved in Tissues at the Time of Irradiation as a Factor in Radiotherapy. *Br. J. Radiol.* **26**, 638–648 (1953).
54. Rischin, D. *et al.* Tirapazamine, Cisplatin, and Radiation Versus Cisplatin and Radiation for Advanced Squamous Cell Carcinoma of the Head and Neck (TROG 02.02, HeadSTART): A Phase III Trial of the Trans-Tasman Radiation Oncology Group. *J. Clin. Oncol.* **28**, 2989–2995 (2010).
55. Moriwaki, T. *et al.* Cytotoxicity of Tirapazamine (3-Amino-1,2,4-benzotriazine-1,4-dioxide)-Induced DNA Damage in Chicken DT40 Cells. *Chem. Res. Toxicol.* **30**, 699–704 (2017).
56. Hicks, K. O. *et al.* Pharmacokinetic/Pharmacodynamic Modeling Identifies SN30000 and SN29751 as Tirapazamine Analogues with Improved Tissue Penetration and Hypoxic Cell Killing in Tumors. *Clin. Cancer Res.* **16**, 4946–4957 (2010).
57. Attard, J.-A. P. *et al.* The Effects of Systemic Hypoxia on Colon Anastomotic Healing: An Animal Model. *Dis. Colon Rectum* **48**, 1460–1470 (2005).
58. Zhan, G., Fenik, P., Pratico, D. & Veasey, S. C. Inducible Nitric Oxide Synthase in Long-term Intermittent Hypoxia. *Am. J. Respir. Crit. Care Med.* **171**, 1414–1420 (2005).
59. Huang, M. *et al.* Capsaicin protects cortical neurons against ischemia/reperfusion injury via down-regulating NMDA receptors. *Exp. Neurol.* **295**, 66–76 (2017).
60. Tamisier, R. *et al.* A new model of chronic intermittent hypoxia in humans: effect on ventilation, sleep, and blood pressure. *J. Appl. Physiol.* **107**, 17–24 (2009).
61. Louis, M. & Punjabi, N. M. Effects of acute intermittent hypoxia on glucose metabolism in awake healthy volunteers. *J. Appl. Physiol.* **106**, 1538–1544 (2009).

62. Macrae, I. M. Focal Ischemia Models: Middle Cerebral Artery Occlusion Induced by Electrocoagulation, Occluding Devices, and Endothelin-1. in *Rodent Models of Stroke* (ed. Dirnagl, U.) 45–58 (Springer, 2016). doi:10.1007/978-1-4939-5620-3_5.

63. Kurth, C. D., McCann, J. C., Wu, J., Miles, L. & Loepke, A. W. Cerebral Oxygen Saturation-Time Threshold for Hypoxic-Ischemic Injury in Piglets. *Anesth. Analg.* **108**, 1268–1277 (2009).

64. Horsley, H., Dharmasena, D., Malone-Lee, J. & Rohn, J. L. A urine-dependent human urothelial organoid offers a potential alternative to rodent models of infection. *Sci. Rep.* **8**, 1238 (2018).

65. Hartung, T. Thoughts on limitations of animal models. *Parkinsonism Relat. Disord.* **14**, S81–S83 (2008).

66. Suntharalingam, G. *et al.* Cytokine Storm in a Phase 1 Trial of the Anti-CD28 Monoclonal Antibody TGN1412. *N. Engl. J. Med.* **355**, 1018–1028 (2006).

67. Muñoz-Sánchez, J. & Chánez-Cárdenas, M. E. The use of cobalt chloride as a chemical hypoxia model. *J. Appl. Toxicol.* **39**, 556–570 (2019).

68. Hirsilä, M. *et al.* Effect of desferrioxamine and metals on the hydroxylases in the oxygen sensing pathway. *FASEB J.* **19**, 1308–1310 (2005).

69. Zhang, Z., Yan, J., Chang, Y., Yan, S. S. & Shi, H. Hypoxia Inducible Factor-1 as a Target for Neurodegenerative Diseases. *Curr. Med. Chem.* **18**, 4335–4343 (2011).

70. Jones, N. M., Kardashyan, L., Callaway, J. K., Lee, E. M. & Beart, P. M. Long-Term Functional and Protective Actions of Preconditioning With Hypoxia, Cobalt Chloride, and Desferrioxamine Against Hypoxic-Ischemic Injury in Neonatal Rats. *Pediatr. Res.* **63**, 620–624 (2008).

71. Swoboda, M. *et al.* Enzymatic Oxygen Scavenging for Photostability without pH Drop in Single-Molecule Experiments. *ACS Nano* **6**, 6364–6369 (2012).

72. Wong, C. M., Wong, K. H. & Chen, X. D. Glucose oxidase: natural occurrence, function, properties and industrial applications. *Appl. Microbiol. Biotechnol.* **78**, 927–938 (2008).

73. Li, C. *et al.* A New Approach for On-Demand Generation of Various Oxygen Tensions for In Vitro Hypoxia Models. *PLOS ONE* **11**, e0155921 (2016).

74. Uppoor, R. & Niebergall, P. J. β-D(+) Glucose-Glucose Oxidase-Catalase for Use as an Antioxidant System. *Pharm. Dev. Technol.* **1**, 127–134 (1996).

75. Allen, C. B., Schneider, B. K. & White, C. W. Limitations to oxygen diffusion and equilibration in in vitro cell exposure systems in hyperoxia and hypoxia. *Am. J. Physiol.-Lung Cell. Mol. Physiol.* **281**, L1021–L1027 (2001).

76. Oppegard, S. C., Blake, A. J., Williams, J. C. & Eddington, D. T. Precise control over the oxygen conditions within the Boyden chamber using a microfabricated insert. *Lab. Chip* **10**, 2366–2373 (2010).

77. Brown, D. A. *et al.* Analysis of oxygen transport in a diffusion-limited model of engineered heart tissue. *Biotechnol. Bioeng.* **97**, 962–975 (2007).

78. Huang, Y., Zitta, K., Bein, B., Steinfath, M. & Albrecht, M. An insert-based enzymatic cell culture system to rapidly and reversibly induce hypoxia: investigations of hypoxia-induced cell damage, protein expression and phosphorylation in neuronal IMR-32 cells. *Dis. Model. Mech.* **6**, 1507–1514 (2013).

79. Acosta, M. A. *et al.* A microfluidic device to study cancer metastasis under chronic and intermittent hypoxia. *Biomicrofluidics* **8**, 054117 (2014).

80. Grist, S., Yu, L., Chrostowski, L. & Cheung, K. C. Microfluidic cell culture systems with integrated sensors for drug screening. in *Microfluidics, BioMEMS, and Medical Microsystems X* vol. 8251 825103 (International Society for Optics and Photonics, 2012).

81. Wang, L. *et al.* Construction of oxygen and chemical concentration gradients in a single microfluidic device for studying tumor cell–drug interactions in a dynamic hypoxia microenvironment. *Lab. Chip* **13**, 695–705 (2013).

82. Leclerc, E., Sakai, Y. & Fujii, T. Microfluidic PDMS (Polydimethylsiloxane) Bioreactor for Large-Scale Culture of Hepatocytes. *Biotechnol. Prog.* **20**, 750–755 (2004).

83. Skolimowski, M. *et al.* Microfluidic dissolved oxygen gradient generator biochip as a useful tool in bacterial biofilm studies. *Lab. Chip* **10**, 2162–2169 (2010).

84. Lam, S. F., Shirure, V. S., Chu, Y. E., Soetikno, A. G. & George, S. C. Microfluidic device to attain high spatial and temporal control of oxygen. *PLOS ONE* **13**, e0209574 (2018).
85. Chen, Y.-A. *et al.* Generation of oxygen gradients in microfluidic devices for cell culture using spatially confined chemical reactions. *Lab. Chip* **11**, 3626–3633 (2011).
86. Wood, D. K., Soriano, A., Mahadevan, L., Higgins, J. M. & Bhatia, S. N. A biophysical marker of severity in sickle cell disease. *Sci. Transl. Med.* **4**, 123ra26 (2012).
87. Wang, X., Jiang, M., Zhou, Z., Gou, J. & Hui, D. 3D printing of polymer matrix composites: A review and prospective. *Compos. Part B Eng.* **110**, 442–458 (2017).
88. Sun, J. & Litchinitser, N. M. Toward Practical, Subwavelength, Visible-Light Photolithography with Hyperlens. *ACS Nano* **12**, 542–548 (2018).
89. Brennan, M. D., Rexius-Hall, M. L., Elgass, L. J. & Eddington, D. T. Oxygen control with microfluidics. *Lab. Chip* **14**, 4305–4318 (2014).
90. Hahn, C. E. W., Hall, E. a. H., Maynard, P. & Albery, W. J. A Sandwich Electrode for Multi-Gas Analysis: A Prototype. *Br. J. Anaesth.* **54**, 681–687 (1982).
91. Bacon, N. C. & Hall, E. A. H. A Sandwich Enzyme Electrode Giving Electrochemical Scavenging of Interferents. *Electroanalysis* **11**, 749–755 (1999).
92. Marei, M. M., Roussel, T. J., Keynton, R. S. & Baldwin, R. P. Electrochemical Dissolved Oxygen Removal from Microfluidic Streams for LOC Sample Pretreatment. *Anal. Chem.* **86**, 8541–8546 (2014).
93. Wong, J. J. Y. A Novel Oxygen Scavenging Device for Cell Models. (University of Cambridge, 2016).
94. Litster, S. & McLean, G. PEM fuel cell electrodes. *J. Power Sources* **130**, 61–76 (2004).
95. Bahadır, E. B. & Sezgintürk, M. K. Applications of commercial biosensors in clinical, food, environmental, and biothreat/biowarfare analyses. *Anal. Biochem.* **478**, 107–120 (2015).
96. Buggy, D. J. & Kerin, M. J. Paravertebral Analgesia with Levobupivacaine Increases Postoperative Flap Tissue Oxygen Tension after Immediate Latissimus Dorsi Breast Reconstruction Compared with Intravenous Opioid Analgesia. *Anesthesiology* **100**, 375–380 (2004).

97. Nørskov, J. K. *et al.* Origin of the Overpotential for Oxygen Reduction at a Fuel-Cell Cathode. *J. Phys. Chem. B* **108**, 17886–17892 (2004).

98. Song, C. & Zhang, J. Electrocatalytic Oxygen Reduction Reaction. in *PEM Fuel Cell Electrocatalysts and Catalyst Layers* (ed. Zhang, J.) 89–134 (Springer London, 2008). doi:10.1007/978-1-84800-936-3_2.

99. Wu, J. & Yang, H. Platinum-Based Oxygen Reduction Electrocatalysts. *Acc. Chem. Res.* **46**, 1848–1857 (2013).

100. Li, Y. *et al.* Stabilization of High-Performance Oxygen Reduction Reaction Pt Electrocatalyst Supported on Reduced Graphene Oxide/Carbon Black Composite. *J. Am. Chem. Soc.* **134**, 12326–12329 (2012).

101. Paulus, U. A., Schmidt, T. J., Gasteiger, H. A. & Behm, R. J. Oxygen reduction on a high-surface area Pt/Vulcan carbon catalyst: a thin-film rotating ring-disk electrode study. *J. Electroanal. Chem.* **495**, 134–145 (2001).

102. Gómez-Marín, A. M., Feliu, J. M. & Ticianelli, E. Oxygen Reduction on Platinum Surfaces in Acid Media: Experimental Evidence of a CECE/DISP Initial Reaction Path. *ACS Catal.* **9**, 2238–2251 (2019).

103. Tripković, V., Skúlason, E., Siahrostami, S., Nørskov, J. K. & Rossmeisl, J. The oxygen reduction reaction mechanism on Pt(1 1 1) from density functional theory calculations. *Electrochimica Acta* **55**, 7975–7981 (2010).

104. Marković, N. M. & Ross, P. N. Surface science studies of model fuel cell electrocatalysts. *Surf. Sci. Rep.* **45**, 117–229 (2002).

105. Hauman, C. H. J. & Love, R. M. Biocompatibility of dental materials used in contemporary endodontic therapy: a review. Part 1. Intracanal drugs and substances. *Int. Endod. J.* **36**, 75–85 (2003).

106. Moggia, G., Kenis, T., Daems, N. & Breugelmans, T. Electrochemical Oxidation of d-Glucose in Alkaline Medium: Impact of Oxidation Potential and Chemical Side Reactions on the Selectivity to d-Gluconic and d-Glucaric Acid. *ChemElectroChem* **7**, 86–95 (2020).
107. Kinsey, D. W. & Bottomley, R. A. Improved Electrode System for Determination of Oxygen Tension in Industrial Applications. *J. Inst. Brew.* **69**, 164–176 (1963).
108. Kolthoff, I. M. & Jordan, J. Oxygen Induced Electroreduction of Hydrogen Peroxide and Reduction of Oxygen at the Rotated Gold Wire Electrode. *J. Am. Chem. Soc.* **74**, 4801–4805 (1952).
109. Rodriguez, P. & Koper, M. T. M. Electrocatalysis on gold. *Phys. Chem. Chem. Phys.* **16**, 13583–13594 (2014).
110. Zhao, Z. Nanostructured Electrodes for Mediated Electrochemical Biosensor Application. (University of Cambridge, 2015).
111. Kunz, H. R. & Gruver, G. A. The Catalytic Activity of Platinum Supported on Carbon for Electrochemical Oxygen Reduction in Phosphoric Acid. *J. Electrochem. Soc.* **122**, 1279 (1975).
112. Honbo, H., Takei, K., Ishii, Y. & Nishida, T. Electrochemical properties and Li deposition morphologies of surface modified graphite after grinding. *J. Power Sources* **189**, 337–343 (2009).
113. Ong, T. S. & Yang, H. Effect of atmosphere on the mechanical milling of natural graphite. *Carbon* **38**, 2077–2085 (2000).
114. Cvelbar, U., Pejovnik, S., Mozetiè, M. & Zalar, A. Increased surface roughness by oxygen plasma treatment of graphite/polymer composite. *Appl. Surf. Sci.* **210**, 255–261 (2003).
115. Dubouis, N. & Grimaud, A. The hydrogen evolution reaction: from material to interfacial descriptors. *Chem. Sci.* **10**, 9165–9181 (2019).
116. Daubinger, P., Kieninger, J., Unmüssig, T. & A. Urban, G. Electrochemical characteristics of nanostructured platinum electrodes – a cyclic voltammetry study. *Phys. Chem. Chem. Phys.* **16**, 8392–8399 (2014).
117. King, F. *et al.* A High-Temperature, High-Pressure, Silver-Silver Chloride Reference Electrode: A User's Guide. 39 (1989).

118. Young, D. A. *Phase diagrams of the elements*. https://www.osti.gov/biblio/4010212 (1975) doi:https://doi.org/10.2172/4010212.

119. Cui, H.-F., Ye, J.-S., Zhang, W.-D., Wang, J. & Sheu, F.-S. Electrocatalytic reduction of oxygen by a platinum nanoparticle/carbon nanotube composite electrode. *J. Electroanal. Chem.* **577**, 295–302 (2005).

120. Lin, L. *et al.* Significant enhancement of the performance of hydrogen evolution reaction through shape-controlled synthesis of hierarchical dendrite-like platinum. *J. Mater. Chem. A* **6**, 8068–8077 (2018).

121. Ramaswamy, N. & Mukerjee, S. Fundamental Mechanistic Understanding of Electrocatalysis of Oxygen Reduction on Pt and Non-Pt Surfaces: Acid versus Alkaline Media. *Adv. Phys. Chem.* **2012**, 1–17 (2012).

122. Clouser, S. J., Huang, J. C. & Yeager, E. Temperature dependence of the Tafel slope for oxygen reduction on platinum in concentrated phosphoric acid. *J. Appl. Electrochem.* **23**, 597–605 (1993).

123. Meng, H. & Shen, P. K. Tungsten Carbide Nanocrystal Promoted Pt/C Electrocatalysts for Oxygen Reduction. *J. Phys. Chem. B* **109**, 22705–22709 (2005).

124. Ge, X. *et al.* Oxygen Reduction in Alkaline Media: From Mechanisms to Recent Advances of Catalysts. *ACS Catal.* **5**, 4643–4667 (2015).

125. Nart, F. C. & Iwasita, T. On the adsorption of H2PO−4 and H3PO4 on platinum: an in situ FT-ir study. *Electrochimica Acta* **37**, 385–391 (1992).

126. Kamat, A. *et al.* Experimental Investigations into Phosphoric Acid Adsorption on Platinum Catalysts in a High Temperature PEM Fuel Cell. *Fuel Cells* **11**, 511–517 (2011).

127. Banerjee, I., Pangule, R. C. & Kane, R. S. Antifouling Coatings: Recent Developments in the Design of Surfaces That Prevent Fouling by Proteins, Bacteria, and Marine Organisms. *Adv. Mater.* **23**, 690–718 (2011).

128. Gao, F. *et al.* Role of ionic strength on protein fouling during ultrafiltration by synchronized UV–vis spectroscopy and electrochemical impedance spectroscopy. *J. Membr. Sci.* **563**, 592–601 (2018).

129. Vannice, M. A., Benson, J. E. & Boudart, M. Determination of surface area by chemisorption: Unsupported platinum. *J. Catal.* **16**, 348–356 (1970).

130. Park, S., Chung, T. D. & Kim, H. C. Nonenzymatic Glucose Detection Using Mesoporous Platinum. *Anal. Chem.* **75**, 3046–3049 (2003).

131. Giannozzi, P., Car, R. & Scoles, G. Oxygen adsorption on graphite and nanotubes. *J. Chem. Phys.* **118**, 1003–1006 (2003).

132. Perry, R. H. & Green, D. W. *Perry's Chemical engineers' handbook*. (New York : McGraw-Hill, 1984).

133. Yao, M. *et al.* Mixing and delivery of multiple controlled oxygen environments to a single multiwell culture plate. *Am. J. Physiol.-Cell Physiol.* **315**, C766–C775 (2018).

134. Mikati, M. A. *et al.* Long-term effects of acute and of chronic hypoxia on behavior and on hippocampal histology in the developing brain. *Dev. Brain Res.* **157**, 98–102 (2005).

135. Anderson, D., Yu, T.-W., Phillips, B. J. & Schmezer, P. The effect of various antioxidants and other modifying agents on oxygen-radical-generated DNA damage in human lymphocytes in the COMET assay. *Mutat. Res. Mol. Mech. Mutagen.* **307**, 261–271 (1994).

136. Cummins, E. P. *et al.* The Hydroxylase Inhibitor Dimethyloxalylglycine Is Protective in a Murine Model of Colitis. *Gastroenterology* **134**, 156-165.e1 (2008).

137. Piret, J.-P., Mottet, D., Raes, M. & Michiels, C. CoCl2, a Chemical Inducer of Hypoxia-Inducible Factor-1, and Hypoxia Reduce Apoptotic Cell Death in Hepatoma Cell Line HepG2. *Ann. N. Y. Acad. Sci.* **973**, 443–447 (2002).

138. Wang, J. *et al.* Identification of one-electron reductases that activate both the hypoxia prodrug SN30000 and diagnostic probe EF5. *Biochem. Pharmacol.* **91**, 436–446 (2014).

139. Thomas, P. C., Raghavan, S. R. & Forry, S. P. Regulating Oxygen Levels in a Microfluidic Device. *Anal. Chem.* **83**, 8821–8824 (2011).

140. Rexius-Hall, M. L., Rehman, J. & Eddington, D. T. A microfluidic oxygen gradient demonstrates differential activation of the hypoxia-regulated transcription factors HIF-1α and HIF-2α. *Integr. Biol.* **9**, 742–750 (2017).

141. Ando, Y. *et al.* A Microdevice Platform Recapitulating Hypoxic Tumor Microenvironments. *Sci. Rep.* **7**, 15233 (2017).

142. Bayer, C. & Vaupel, P. Acute versus chronic hypoxia in tumors: Controversial data concerning time frames and biological consequences. *Strahlenther. Onkol.* **188**, 616–627 (2012).

143. Yuan, J., Narayanan, L., Rockwell, S. & Glazer, P. M. Diminished DNA Repair and Elevated Mutagenesis in Mammalian Cells Exposed to Hypoxia and Low pH. *Cancer Res.* **60**, 4372–4376 (2000).

144. Yang, A.-S. & Honig, B. On the pH Dependence of Protein Stability. *J. Mol. Biol.* **231**, 459–474 (1993).

145. Talley, K. & Alexov, E. On the pH-optimum of activity and stability of proteins. *Proteins Struct. Funct. Bioinforma.* **78**, 2699–2706 (2010).

146. Huang, M. *et al.* Carbon Dots for Intracellular pH Sensing with Fluorescence Lifetime Imaging Microscopy. *Nanomaterials* **10**, 604 (2020).

147. Choi, D. W. Ischemia-induced neuronal apoptosis. *Curr. Opin. Neurobiol.* **6**, 667–672 (1996).

148. Saab, A. S., Tzvetanova, I. D. & Nave, K.-A. The role of myelin and oligodendrocytes in axonal energy metabolism. *Curr. Opin. Neurobiol.* **23**, 1065–1072 (2013).

149. Mahmoud, S., Gharagozloo, M., Simard, C. & Gris, D. Astrocytes Maintain Glutamate Homeostasis in the CNS by Controlling the Balance between Glutamate Uptake and Release. *Cells* **8**, (2019).

150. Gustafsson, M. V. *et al.* Hypoxia Requires Notch Signaling to Maintain the Undifferentiated Cell State. *Dev. Cell* **9**, 617–628 (2005).

151. Wang, G. L., Jiang, B. H., Rue, E. A. & Semenza, G. L. Hypoxia-inducible factor 1 is a basic-helix-loop-helix-PAS heterodimer regulated by cellular O2 tension. *Proc. Natl. Acad. Sci.* **92**, 5510–5514 (1995).
152. Campenot, R. B. Local control of neurite development by nerve growth factor. *Proc. Natl. Acad. Sci.* **74**, 4516–4519 (1977).
153. Taylor, A. M. *et al.* A microfluidic culture platform for CNS axonal injury, regeneration and transport. *Nat. Methods* **2**, 599–605 (2005).
154. Idrizaj, E. *et al.* Cortical and spinal conditioned media modify the inward ion currents and excitability and promote differentiation of human striatal primordium. *J. Chem. Neuroanat.* **90**, 87–97 (2018).
155. Vereyken, E. J. *et al.* Classically and alternatively activated bone marrow derived macrophages differ in cytoskeletal functions and migration towards specific CNS cell types. *J. Neuroinflammation* **8**, 58 (2011).
156. Demchenko, A. P. Beyond annexin V: fluorescence response of cellular membranes to apoptosis. *Cytotechnology* **65**, 157–172 (2013).
157. McDonald, J. C. *et al.* Fabrication of microfluidic systems in poly(dimethylsiloxane). *ELECTROPHORESIS* **21**, 27–40 (2000).
158. Hofmann, O., Niedermann, P. & Manz, A. Modular approach to fabrication of three-dimensional microchannel systems in PDMS—application to sheath flow microchips. *Lab. Chip* **1**, 108–114 (2001).
159. Di Donato, C. *et al.* Polypseudorotaxanes of Pluronic® F127 with Combinations of α- and β-Cyclodextrins for Topical Formulation of Acyclovir. *Nanomaterials* **10**, 613 (2020).
160. Magliaro, C. *et al.* Oxygen Consumption Characteristics in 3D Constructs Depend on Cell Density. *Front. Bioeng. Biotechnol.* **7**, (2019).

161. Herst, P. M. & Berridge, M. V. Cell surface oxygen consumption: A major contributor to cellular oxygen consumption in glycolytic cancer cell lines. *Biochim. Biophys. Acta BBA - Bioenerg.* **1767**, 170–177 (2007).

Appendix

Appendix I. Methodology of surface modification

I. Materials

1H,1H,2H,2H-perfluorooctyltriethoxysilane (PFTES) was purchased from Alfa Aesar. Fluorescently tagged poly-L-lysine (PLL-FITC), Pluronic F127 and ethanol were purchased from Sigma Aldrich.

II. Static water contact angle measurement

The contact angle equipment was used to measure the hydrophilicity of native materials and post-modified materials. Water droplets of 7 µL were dropped vertically and carefully onto the surfaces of materials. Images of the water droplets were taken laterally immediately and the contact angles between the liquid and the material were measured and compared. All experiments had the contact angle reported as mean ± S.D. calculated from 3 experimental repeats.

III. Silanisation optimization

The glass slides were first cleaned in a beaker by sonicating, in sequence, in isopropanol, acetone and Milli-Q water for 3-5 minutes each. The coverslips were thus dried and placed in a dry plate covered from dust and dirt. They were thus surface activated by oxygen plasma at 70% power (70W) for 45 seconds. PFDTS solution, prepared by dissolving 1% (v/v) in ethanol, was immediately added onto the glass surfaces enough to cover without overflowing. The coverslips were protected from ambient and placed at room temperature for 15 minutes, 30 minutes and 1 hour for silane self-assembled monolayer formation. The silane was thus aspirated from the coverslips without physical contact. The coverslips were rinsed 3 times with ethanol and then 3 times with water. Silane covered coverslips were thus allowed curing at 40°C for one hour on a hot plate. The contact angles of the coverslips were tested and evaluated against the theoretical value in literature.

IV. Pluronic F127 surface coating optimization

Silanized glass slides were used after the curing process. Pluronic F127 was dissolved in PBS at 0.2%, 0.5% and 1% (w/v). Negative control used for comparison was pure PBS. Pluronic F127 conditions were added to cover coverslips and the entire well was incubated in room temperature for 30 minutes. The coverslips were rinsed 3 times in PBS after the incubation. The coating efficiency was measured by the contact angle and neuron attachment (50,000 cells/cm^2). Flat cells, considered as viable cells after 6 days from replating, were counted and reported as mean ± S.D.

V. Protocols for surface patterning and optimization

Four protocols were designed for patterning the surface of the glass for neuron cultures. The steps for each protocol are shown in the schematic in fig. 4.3 and are explained here briefly. The PFDTS-glass was used as it was after the silanization protocol whereas a stripped patterned PDMS stamp and a non-patterned PDMS block were used as the patterning blocks. The blocks were cleaned by sonicating in ethanol and water for 5 minutes each, and thus dried with nitrogen gas. The contacting surfaces were protected by tape until use.

Method 1 investigated the effectiveness of PFDTS patterns in blocking neuron adhesion and growth. The patterned PDMS stamp and the PFDTS-glass were placed in the vacuum for 10-15 minutes to ensure they were dried completely. The PDMS pattern, tape removed, was thus pressed on top the PFDTS-glass. Oxygen plasma (60% power / 60W, for 60 seconds) was used to remove the PFDTS not protected by the PDMS pattern. The stamp was removed after and PDL at 5μg/cm^2 in pH 8.5 borate buffer were added to the wells for 1-hour incubation at 37°C. The surfaces were rinsed 3 times with PBS and coated with laminin at 1.5μg/cm^2 in PBS overnight at 37°C. The surface was then ready for cell culturing.

Method 2 to method 4 investigated whether Pluronic F127 can effectively retain its level of cell repulsion. In method 2, PFDTS-glass was first coated with 0.5% Pluronic F127 for 30 minutes. The glass was thus assembled with the PDMS stamp and subjected to oxygen plasma (60% power / 60W, for 60 seconds). It was then coated with PDL (5μg/cm^2) and laminin (1.5μg/cm^2) in the absence of the PDMS stamp.

Methods 3 and 4 were first patterned with PDMS in oxygen plasma (60% power / 60W, for 60 seconds). Method 3 attempted to coat both PDL (5μg/cm^2) and laminin (1.5μg/cm^2) with the PDMS stamp attached until the coating of Pluronic F127 (0.5% for 30 minutes). In method 4, PDMS stamp was attached when coating PDL (5μg/cm^2) but was removed for Pluronic F127 coating (0.5% for 30 minutes), followed by laminin coating (1.5μg/ cm^2). Products from all methods were plated with human neurons for investigating the cell repulsion effectiveness.

VI. Optimization of coating microchannels

Poly-L-lysine (PLL)–FITC, labelled PLL, was used to visualize the coating efficiency in the microchannels. PLL-FITC was diluted in at 5μg/mL in PBS and coated on the glass for 1.5h, 3.5h and 72h. Widefield microscopy was used to image the PLL-FITC and its diffusion distances were measured and compared.